1 A Primer on Compact Objects

Within the cores of stars, there exists a delicate balance between the gravitational forces pulling the matter inward, and the outward pressure generated by the thermonuclear fusion of light elements. This process begins as hydrogen is fused to form helium. Eventually, the hydrogen is depleted, allowing gravity to temporarily overcome the outward pressure, leading to the core to begin contracting. As this occurs, the gravitational potential energy is converted to thermal energy and the core eventually becomes hot enough to facilitate helium burning.

This cycle can continue as heavier and heavier elements are formed within the ever-increasingly hot stellar core. Lighter stars cannot reach the temperatures required to fuse light elements such as helium and carbon. If the star is heavy enough, iron will eventually be formed from the burning of silicon. As the fusion of iron nuclei is an endothermic process, it will not occur spontaneously, ending the cycle in heavy stars. Without a fuel source, the core will collapse under its gravity, leading to the death of the star.

What comes after this collapse depends on the mass of the progenitor star. Very light stars, $\lesssim 0.5M_\odot$, have lifetimes much longer than the age of the universe, and so are uninteresting to our current discussion. Moderately heavy stars, $1M_\odot \lesssim M_\star \lesssim 8M_\odot$, will continue burning fuel until the outer layers of the star are dispersed as it expands, leaving a core comprised of helium, carbon, and oxygen with and small abundance of heavier elements. In this case, the core will begin to collapse until the Fermi degeneracy of the ultrarelativistic electrons is great enough to reestablish equilibrium, resulting in a White Dwarf (WD) [1].

Heavy stars, $\gtrsim 8M_\odot$, spectacularly end their lives in a type-II supernova event. This occurs when the core of the star exceeds the Chandrashekhar mass of $1.4M_\odot$, which cannot be supported by electron degeneracy pressure. The core itself will then collapse, leading to a shockwave that ejects the majority of the mass of the star.

All that will remain is an extremely dense core supported by neutron degeneracy pressure: a Neutron Star (NS) [2]. If the star was so massive that the gravitational forces overcome even the neutron degeneracy pressure, then the core collapses into a black hole.

These stellar corpses, white dwarfs, neutron stars, and black holes, are collectively known as compact objects. They have masses similar to or larger than the Sun, which is compressed into much smaller bodies with significantly larger surface gravities. These objects do not have a source of fuel, and spend the rest of their lives cooling through the emission of photons and neutrinos. For the remainder of this thesis, we will only be interested in white dwarfs and neutron stars and will collectively refer to these as compact objects, excluding black holes from this term.

This chapter is dedicated to discussing the aspects of the structure, composition, and observational status of compact objects relevant to this work

1.1 Structure Equations from General Relativity

Being comprised of matter in a highly dense state, the gravitational fields produced by neutron stars and white dwarfs are extremely strong. As such, modeling the structure of these objects falls into the domain of General Relativity (GR). Here we review the structure of static, spherically symmetric, compact objects, adapting the discussions in Refs. [3–5].

First, the static nature of the star means that the components of the metric are functions only of the spatial coordinates and not of time. Together with the assumption that the mass distribution of the star is spherically symmetric, this leads to a Schwarzschild-like metric of the form

$$ds^2 = -d\tau^2 = -B(r)dt^2 + A(r)dr^2 + r^2 d\Omega^2, \tag{1.1}$$

with $d\tau$ the proper time interval. The functions $A(r)$, $B(r)$ depend only on the radial coordinate, and are often written as

$$A(r) = e^{2\Lambda(r)}, \quad B(r) = e^{2\Phi(r)}. \tag{1.2}$$

These functions are subject to the condition that at distances far from the star, $r \to \infty$, space-time must become flat, which translates to the boundary conditions

$$\lim_{r\to\infty} A(r) = \lim_{r\to\infty} B(r) = 1. \tag{1.3}$$

The matter within the star can be modeled as a perfect fluid, meaning we are neglecting any shear stresses and energy transport within the star. Such a fluid is described by its pressure $P(r)$, density $\rho(r)$, and baryonic number density, $n_b(r)$, as well as the 4-velocity of the fluid $u^\mu(r)$. Being static, the only non-zero component of this velocity is the $\mu = 0$ component, which is fixed by the normalisation condition $g_{\mu\nu}u^\mu u^\nu = -1$ to be $u^0 = 1/\sqrt{B(r)}$. These quantities are used to construct the stress-energy tensor of the star, which takes the form

$$T^{\mu\nu} = (\rho + P)u^\mu u^\nu + Pg^{\mu\nu}. \tag{1.4}$$

The physics describing the underlying microscopic interactions within matter are encoded in an equation of state (EoS) that describes the relationship between the various thermodynamic quantities. This is typically expressed by providing the pressure as a function of the density, $P(\rho)$. It is often more convenient to parameterise the EoS by the number density of baryons n_b, and the entropy per baryon s, such that

$$P = P(n_b, s), \quad \rho = \rho(n_b, s). \tag{1.5}$$

The dependence on s turns out to be trivial in most scenarios involving compact objects, such as those considered througout this work. The pressure in these stars arises from the degeneracy of the nucleons in NSs or the electrons in WDs, rather than from the thermal motion of the constituents as in main sequence stars. These thermal degrees of freedom will be frozen out at temperatures lower than the Fermi energy of the system, which is typically around $E_F \sim 10\,\mathrm{MeV}$ in NSs or $\sim 1\,\mathrm{MeV}$ in WDs, and correspond to temperatures of $T_\star \sim 10^{11}\,\mathrm{K}$ and $\sim 10^{10}\,\mathrm{K}$ respectively. As these objects are expected to cool well below these temperatures quickly after formation [6–8], the entropy can be taken to be zero throughout the star. This allows us to reduce the two-parameter EoS to a simpler one-parameter one,

$$P = P(n_b, s = 0) = P(n_b), \quad \rho = \rho(n_b, s = 0) = \rho(n_b). \tag{1.6}$$

The structure of the star is therefore dictated by the quantities $A(r)$, $B(r)$, $P(r)$, $\rho(r)$, and $n_b(r)$. This system is determined by applying the Einstein field equations, $G^{\mu\nu} = 8\pi T^{\mu\nu}$, together with the energy-momentum conservation, $T^{\mu\nu}{}_{;\nu} = 0$, the EoS relations Eqs. 1.6, and the appropriate boundary conditions. The structure equations that come out of this analysis were first discovered concurrently by Tolman [9] and by Oppenheimer and Volkoff [10], and so are known as the TOV equations. They take the form

$$\frac{dP}{dr} = -\rho(r)c^2\left[1 + \frac{P(r)}{\rho(r)c^2}\right]\frac{d\Phi}{dr}, \tag{1.7}$$

$$\frac{d\Phi}{dr} = \frac{GM(r)}{c^2r^2}\left[1 + \frac{4\pi r^3 P(r)}{M(r)c^2}\right]\left[1 - \frac{2GM(r)}{c^2 r}\right]^{-1}, \tag{1.8}$$

$$\frac{dB}{dr} = 2B(r)\frac{d\Phi}{dr}, \tag{1.9}$$

where $M(r)$ is related to the metric factor $A(r)$ through

$$A(r) = \left[1 - \frac{GM(r)}{c^2 r}\right]^{-1}, \tag{1.10}$$

and is interpreted as the mass contained within a radius r. It obeys the mass equation

$$\frac{dM}{dr} = 4\pi r^2 \rho(r), \quad M(0) = 0, \tag{1.11}$$

which arises from the $\mu = \nu = 0$ component of the Einstein field equiations. These equations are the general relativistic versions of the hydrostatic equilibrium equations of regular stellar structure, with Eq. 1.7 reducing to the familiar

$$\frac{dP}{dr} = -\frac{GM(r)}{r^2}\rho(r), \tag{1.12}$$

in the Newtonian limit, $GM(r)/c^2 r \ll 1$.

The radius of the star, $R_\star$, is identified as the point at which the pressure and density vanish, $P(R_\star) = \rho(R_\star) = 0$. In the region outside the star, $r > R_\star$, the total mass remains constant at the total mass of the star, $M(r \geq R_\star) = M_\star$, and so the only non-trivial structure functions in this region are the metric factors. Solving Eq. 1.9 for $B(r)$ with $P(r) = 0$ and constant $M(r) = M_\star$ leaves us with

$$A(r) = \left[1 - \frac{GM_\star}{c^2 r}\right]^{-1}, \quad B(r) = 1 - \frac{GM_\star}{c^2 r}, \quad \text{for } r > R_\star, \tag{1.13}$$

and the metric reduces to the familiar Schwarzschild metric outside the star. Continuity of the metric at $r = R_\star$ enforces a second boundary condition for $B(r)$,

$$B(R_\star) = 1 - \frac{GM_\star}{c^2 R_\star}. \tag{1.14}$$

The final boundary condition required is the central pressure $P(0) = P_c$ or, equivalently the central density/baryon number density. This is the only free parameter in the system and hence, for a given EoS, uniquely determines the stellar structure. Therefore, all the stars that are predicted by solving the coupled TOV + EoS system can be represented by a one-parameter sequence, represented by the mass-radius relation for the EoS model.

Given all the above, we can write a simple recipe for constructing a model of a compact object:

1. Model the constituent matter with an appropriate EoS.

2. Specify the central pressure of the star, P_c.

3. Integrate the coupled system of differential equations 1.7, 1.8, 1.11 from the centre of the star outward until the pressure vanishes.

4. Use the boundary condition Eq. 1.14 to normalise the metric function $B(r)$.

In general, additional quantities will be present in the EoS, such as chemical potentials and the speed of sound, which may be subject to additional constraints. These quantities will need to be calculated at each step of the integration alongside the other structure functions.

1.2 White Dwarfs

The fate of main sequence stars of mass below $M_\star \lesssim 8M_\odot$ is to end their lives as a white dwarf. Consequently, these compact stellar remnants, which are supported against gravitational collapse by electron degeneracy pressure, are the most abundant stars in the Galaxy ($\gtrsim 90\%$). They are born at very high temperatures and cool down over billions of years. Observations of the coldest WDs therefore contain information about the star formation history of the Galaxy.

The vast majority of observed WDs are composed primarily of carbon and oxygen, plus small traces of elements heavier than helium. At the extremely high densities found in WDs, $\rho_\star \sim 10^6 - 10^{10}\,\mathrm{g\,cm^{-3}}$, electrons are strongly degenerate and determine the WD equation of state (EoS) and internal structure. The stellar core resembles a Coulomb lattice of ions surrounded by the degenerate electron gas, implying that the WD core is isothermal and a very good thermal conductor. The degenerate core is enclosed by a thin envelope that accounts for $\lesssim 1\%$ of the total mass [11].

The outer layers form an atmosphere that is rich in lighter elements such as hydrogen or helium, where the exact composition depends on the evolution of the WD progenitor and changes as the WD cools. This atmosphere is non-degenerate and extremely opaque to radiation, with an EoS that is subject to finite temperature effects. We limit our discussion to the core region of the WD, which accounts for the vast majority of its mass.

1.2.1 The FMT Equation of State

In the limit of zero temperature, the simplest way to obtain the WD EoS is to assume an ideal Fermi gas of degenerate electrons, for a WD that is primarily composed of a single element. Corrections to the non-interacting electron picture were introduced early by Salpeter [12]. By introducing the Wigner-Seitz (WS) cell approximation and assuming point-like nuclei, Salpeter obtained an analytical EoS that accounts for interactions between electrons and ions as well as other Coulomb corrections. These corrections, in general, depend on the chemical composition of the star.

More recently, it has been shown that the treatment of matter at high pressures presented by Feynman, Metropolis and Teller [13] can be extended to consistently take into account weak interactions and relativistic effects [14, 15], and incorporates Coulomb corrections in a more natural manner than the Salpeter EoS. The resulting Feynman-Metropolis-Teller (FMT) EoS is obtained by considering a relativistic Thomas-Fermi model within Wigner-Seitz cells of radius $R_{\rm WS}$. For degenerate, relativistic, electrons, the equilibrium condition is that the Fermi energy, E_e^F, is constant within the cell,

$$E_e^F = \sqrt{(p_e^F)^2 + m_e^2} - m_e - eV(r) = \text{constant}, \tag{1.15}$$

where $V(r)$ is the Coulomb potential inside the cell, p_e^F is the electron Fermi momentum, m_e is the electron mass and e is the electric charge. To obtain an integrable solution for the energy density near the origin, it is necessary to introduce a finite size for the nucleus, with radius $R_c = \Delta\lambda_\pi Z^{1/3}$, where λ_π is the pion Compton wavelength, $\Delta \approx (r_0/\lambda_\pi)(A/Z)^{1/3}$, Z is the proton number, A is the atomic mass, and r_0 is an empirical constant ~ 1.2 fm. The proton and electron number densities inside the cell are then given by

$$n_p = \frac{(p_p^F)^3}{3\pi^2} = \frac{3Z}{4\pi R_c^3}\theta(R_c - r) = \frac{3}{4\pi}\left(\frac{1}{\Delta\lambda_\pi}\right)^3 \theta(R_c - r), \tag{1.16}$$

$$n_e = \frac{(p_e^F)^3}{3\pi^2} = \frac{1}{3\pi^2}\left[\hat{V}^2(r) + 2m_e\hat{V}(r)\right]^{3/2}, \tag{1.17}$$

$$\hat{V}(r) = eV(r) + E_e^F. \tag{1.18}$$

The Coulomb potential satisfies the Poisson equation

$$\nabla^2 V(r) = -4\pi e[n_p(r) - n_e(r)], \tag{1.19}$$

with the requirement of global charge neutrality of the cell enforcing the boundary conditions

$$\left.\frac{dV}{dr}\right|_{r=R_{\rm WS}} = V(R_{\rm WS}) = 0. \tag{1.20}$$

In practice, it is beneficial to work with dimensionless quantities, and so we define $x = r/\lambda_\pi$ and $\chi(r) = r\hat{V}(r)$, such that $x_c = R_c/\lambda_\pi$ and $x_{\rm WS} = R_{\rm WS}/\lambda_\pi$. Using these expressions results in the relativistic Thomas-Fermi equation

$$\frac{1}{3x}\frac{d^2\chi}{dx^2} = -\frac{\alpha_{\rm EM}}{\Delta^3}\theta(x_c - x) + \frac{4\alpha_{\rm EM}}{9\pi}\left[\frac{\chi^2(x)}{x^2} + 2\frac{m_e}{m_\pi}\frac{\chi(x)}{x}\right]^{3/2}, \tag{1.21}$$

with the boundary conditions

$$\chi(0) = 0, \qquad \left.\frac{d\chi}{dx}\right|_{x_{\rm WS}} = \frac{\chi(x_{\rm WS})}{x_{\rm WS}}. \tag{1.22}$$

By solving these equations, we can obtain the relevant thermodynamic quantities, namely the electron and proton number densities, electron chemical potential, and the energy and pressure of the cell. The electron chemical potential is obtained by evaluating Eq. 1.15 at the cell radius, noting that the Coulomb potential must vanish there, which results in the usual expression[1]

$$\varepsilon_{F,e} = \sqrt{(p_e^F)^2 + m_e^2} - m_e. \tag{1.23}$$

The energy and pressure of the cell can then be obtained following the analysis presented in ref. [15]. The cell energy gains contributions from the nuclear mass, electron kinetic energy, and Coulomb interactions, such that

$$E_{\rm tot} = M_N + E_k + E_C, \tag{1.24}$$

$$E_k = \int_0^{R_{WS}} 4\pi r^2 [\mathcal{E}_e(r) - m_e n_e(r)]\, dr, \tag{1.25}$$

$$E_C = \frac{1}{2}\int_{R_c}^{R_{WS}} 4\pi r^2 e[n_p(r) - n_e(r)] V(r)\, dr, \tag{1.26}$$

where

$$\mathcal{E}_e(r) = \frac{1}{\pi^2}\int_0^{p_e^F} p^2\sqrt{p^2 + m_e^2}\, dp, \tag{1.27}$$

is the electron energy density, and M_N is the mass of the nucleus. The energy density of the cell is then simply

$$\rho_{\rm WS} = \frac{E_{\rm tot}}{V_{\rm WS}}, \tag{1.28}$$

where $V_{\rm WS} = 4\pi R_{\rm WS}/3$ is the volume of the WS cell. The only contribution to the internal cell pressure comes from the electrons,

$$P_e(r) = \frac{1}{3\pi^2}\int_0^{p_e^F} \frac{p^4}{\sqrt{p^2 + m_e^2}}\, dp, \tag{1.29}$$

with the total pressure of the cell being $P_{\rm tot} = P_e(R_{WS})$. Finally, the EoS is then obtained by solving Eq. 1.21 for various cell radii, yielding a relation between $E_{\rm tot}(R_{\rm WS})$ and $P_{\rm tot}(R_{\rm WS})$ parameterised by the radius of the Wigner-Seitz cell.

[1] We use the symbol $\varepsilon_{F,i}$ to represent the chemical potential minus the mass of a particle species i, reserving $\mu_{F,i}$ for the full chemical potential.

EoS	**WD$_1$**	**WD$_2$**	**WD$_3$**	**WD$_4$**
$\rho_c\,[\mathrm{g\,cm^{-3}}]$	1.47×10^{6}	3.84×10^{7}	3.13×10^{8}	2.31×10^{10}
$M_\star\,[M_\odot]$	0.440	1.000	1.252	1.384
$R_\star\,[\mathrm{km}]$	9.39×10^{3}	5.38×10^{3}	3.29×10^{3}	1.25×10^{3}
$v_{\rm esc}(R_\star)\,[\mathrm{km/s}]$	3.72×10^{3}	7.03×10^{3}	1.01×10^{4}	1.71×10^{4}

Table 1.1: Four configurations for white dwarfs composed of carbon, with an FMT EoS. Shown are the central densities, ρ_c, stellar mass $M_\star$ and radius $R_\star$, and escape velocity at the edge of the WD, $v_{\rm esc}$.

Different WD configurations can be obtained, assuming a non-rotating spherically symmetric star, by solving the Tolman-Oppenheimer-Volkoff (TOV) equations [9, 10] coupled to the FMT EoS with different initial conditions for the pressure at the centre of the star. In Fig. 1.1 we show radial profiles for n_e (top left), $\varepsilon_{F,e}$ (top right), and escape velocity $v_{\rm esc}$ (bottom) for the carbon WDs in Table 1.1. Note that the difference in radius between the lightest and heaviest WD in Table 1.1 spans almost one order of magnitude, while the electron number densities in the core can vary up to 4 orders of magnitude (see top left panel). As expected, electrons are more degenerate in more compact WDs and become relativistic (see top right panel). The escape velocity can reach $\mathcal{O}(0.1\,c)$ at the interior of the most compact WDs, while for very low mass WDs it can be as low as $\sim 0.003\,c$.

The mass-radius relations obtained from a zero-temperature EoS begin to deviate from observations for low-mass WDs. To address this discrepancy, finite temperature effects can be introduced to the EoS [16]. The extension to finite temperatures is made by reintroducing the temperature dependence in the Fermi-Dirac distributions. Now, the electron chemical potential is no longer simply the Fermi energy of the system due to thermal corrections. Define the finite temperature Fermi-Dirac integrals of degree s as

$$F_s(\eta,\beta) = \int_0^\infty \frac{t^s\sqrt{1+(\beta/2)t}}{1+e^{t-\eta}}dt, \tag{1.30}$$

where we define the dimensionless quantities

$$t = \frac{E_e - m_e}{T_\star}, \tag{1.31}$$

$$\eta = \frac{\varepsilon_{F,e}}{T_\star}, \tag{1.32}$$

$$\beta = \frac{T_\star}{m_e}, \tag{1.33}$$

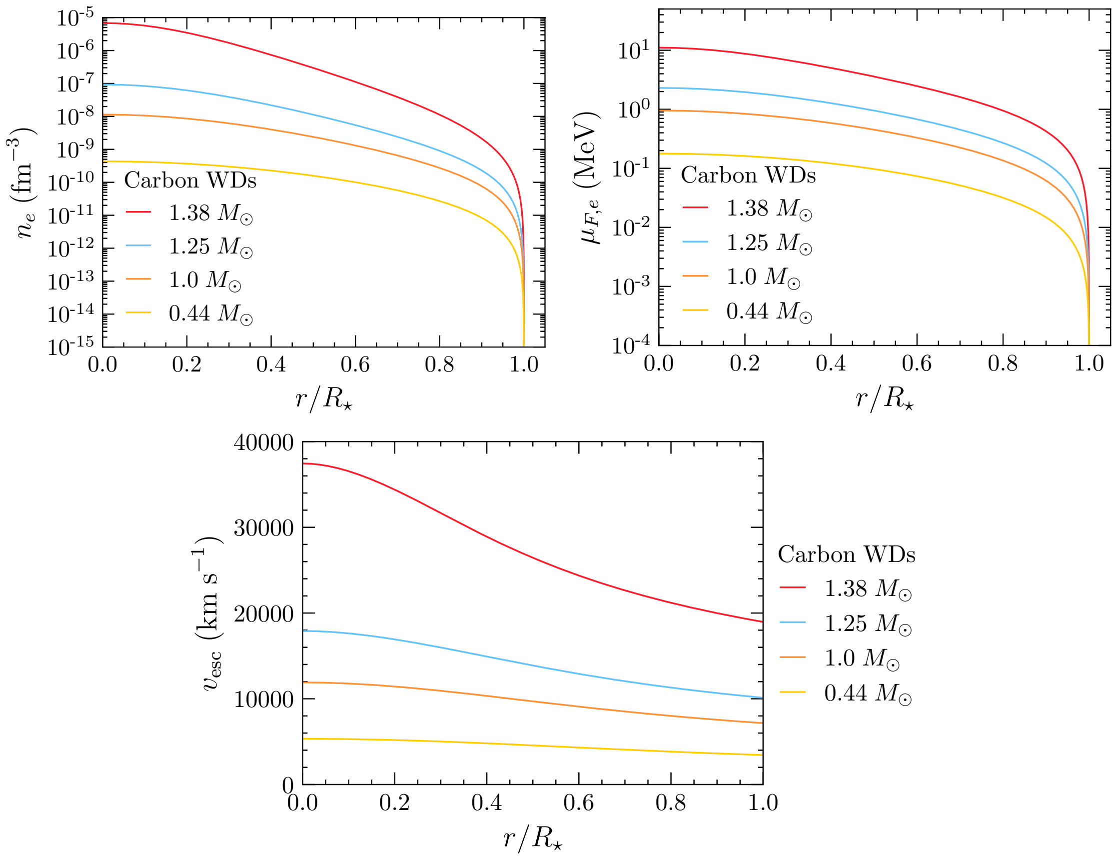

Figure 1.1: Electron number density (top left), chemical potential (top right), and escape velocity (bottom) radial profiles for the carbon WDs with FMT EoS in Table 1.1. The radial distance of each profile has been normalised to the radius of the star.

for a star at temperature $T_\star$. The Thomas-Fermi equilibrium condition within the WS cell is now given by

$$\varepsilon_{F,e}(r) - eV(r) = T_\star\eta(r) - eV(r) = \text{constant}, \tag{1.34}$$

with the Coulpmb potential vanishing at the boundary of the cell as before. We now make the change of variables into the dimensionless quantities $\chi/r = \varepsilon_{F,e}/(\hbar c)$ and $x = x/x_{\text{WS}}$ so that the Poisson equation 1.19 becomes

$$\begin{aligned}\frac{d^2\chi}{dx^2} = -4\pi\alpha_{\text{EM}}x\Bigg(&\frac{3}{4\pi\Delta^3}\theta(x_c - x)\\ &-\frac{\sqrt{2}}{\pi^2}\left(\frac{m_e}{m_\pi}\right)^2\left[F_{1/2}(\eta,\beta) + \beta F_{3/2}(\eta,\beta)\right]\Bigg),\end{aligned} \tag{1.35}$$

$$\eta(x) = \left(\frac{1}{\lambda_\pi T_\star}\right)\frac{\chi(x)}{x}, \tag{1.36}$$

with the same boundary conditions as in Eq. 1.22.

The total energy of the cell remains very similar to the zero-temperature case, with the main differences being that it gains a contribution from the thermal motion of the nucleus,

$$E_{\text{th}} = \frac{3}{2}T_\star, \tag{1.37}$$

and that the electron energy density is now given by

$$\mathcal{E}_e = m_e n_e + \frac{\sqrt{2}}{\pi^2}m_e^4\beta^{5/2}\left[F_{3/2}(\eta,\beta) + \beta F_{5/2}(\eta,\beta)\right]. \tag{1.38}$$

The pressure of the cell will now gain contributions from the motion of the nucleus as well as the electron, such that the total pressure is

$$P_{\text{tot}} = P_N + P_e, \tag{1.39}$$

$$P_N = \frac{2}{3}\frac{E_{\text{th}}}{V_{\text{WS}}} = \frac{T_\star}{V_{\text{WS}}}, \tag{1.40}$$

$$P_e = \frac{2^{3/2}}{3\pi}me^4\beta^{5/2}\left[F_{3/2}(\eta(x_{\text{WS}}),\beta) + \beta F_{5/2}(\eta(x_{\text{WS}}),\beta)\right]. \tag{1.41}$$

In Fig. 1.2 we show the Mass-Radius relations obtained from the zero temperature FMT EoS together with several finite temperature configurations. As can be seen, the deviations from the zero temperature approximation begin at rather high temperatures, $T_\star \gtrsim 10^7\,$K, for masses $\lesssim 0.6M_\odot$. Additionally, we show a random selection of 20,000 WDs presented in the Gaia early data release 2 (EDR2) report [17] as the yellow-red dots. The colour of the dot represents the internal temperature of the corresponding WD. The core temperature must be determined from the observed effective surface temperature of the star[2], with the relation between the two depending on the composition of the WD atmosphere. To obtain the central temperature from the reported effective temperatures, we use the WD cooling sequences generated in Ref. [8][3] assuming a thin hydrogen atmosphere. In general, there is good agreement between the mass-radius relations derived from the finite temperature FMT EoS and the observed internal temperatures of the WDs.

Given the non-linear nature of the differential equations that describe the FMT EoS (both at zero and finite temperatures), solving the system is a numerically challenging task. As there are no publically available resources to help solve these systems, a significant amount of time was put into solving this problem. As such, we have outlined in Appendix **??** the method employed in numerically solving the differential equations.

1.2.2 Observational Status

The rate at which the energy of the WD core is radiated away is determined by the outer non-degenerate layers of the atmosphere. Spectroscopic observations shed light on the composition of these layers and can be used to classify WDs in terms of $\sim$ six spectral types. Most of the observed WDs lie in the DA (hydrogen-rich) and DB (helium-rich) categories. Note that as WDs slowly cool, they undergo spectral evolution. There is a well-defined relation between their luminosity and age (cooling time) that, together with recent breakthroughs in theory and observations, allow us to estimate the age of the stars within the solar neighbourhood and to date the nearest star clusters [18–22].

Over the past few decades, WDs have been extensively observed using photometry and spectroscopy. Most of the WDs have been discovered by large area surveys, such as the Sloan Digital Sky Survey (SDSS) [23]. However, these local samples are dominated by young WDs with relatively high effective temperatures ($T_{\rm eff} \gtrsim 10^4\,$K) [24–28]. Recently, the local volume sample of nearby stars within $\sim 100\,$pc has been catalogued by the Gaia spacecraft [29, 30], an astrometric mission. New WD candidates have been identified [17], followed by dedicated spectroscopic observations [31, 32], increasing the local sample of cool WDs ($T_{\rm eff} \lesssim 5000\,$K).

[2]The effective temperature is the temperature that characterises the surface of the star. Assuming that WDs are perfect blackbody emitters, the luminosity will be $L_\gamma = 4\pi\sigma_{SB}\,R_\star^2\,T_{\rm eff}^4$, where σ_{SB} is the Stefan–Boltzmann constant.

[3]The cooling sequence data can be obtained from `http://www.astro.umontreal.ca/ bergeron/CoolingModels`.

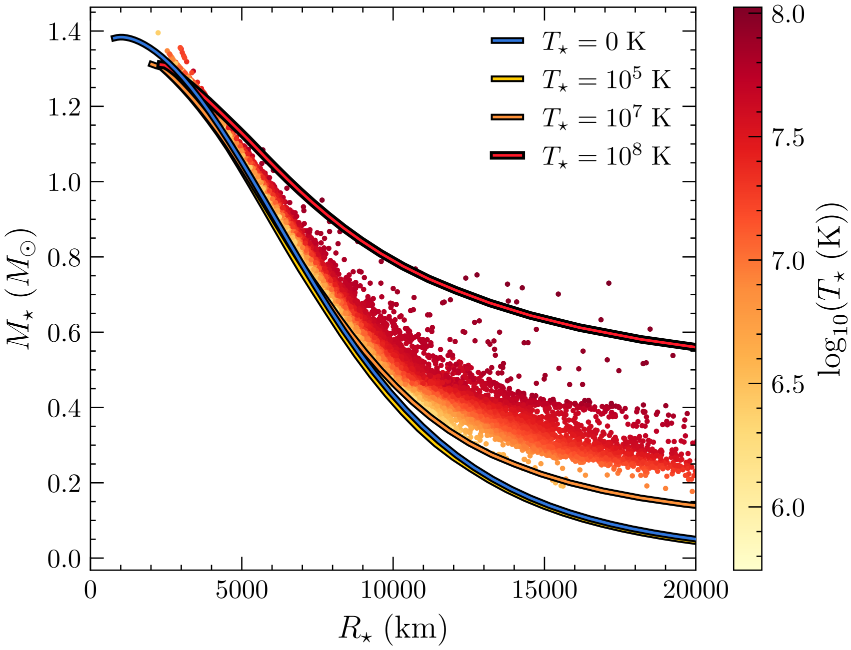

Figure 1.2: Mass-Radius relation of WDs calculated from the FMT EoS in the zero-temperature approximation (dark blue), at 10^5 K (yellow), 10^7 K (orange), and 10^8 K (red), together with observed WDs from Gaia EDR2 observations [17] (yellow-red dots). The colour of the dots represents the surface temperature of the WD inferred from cooling models [8].

On the other hand, globular clusters (GCs) are the oldest known stellar systems in the Galaxy. Among them is Messier 4 (M4), also classified as NGC 6121, which is the closest globular cluster to Earth being $\sim 1.9\,\mathrm{kpc}$ away [33–35]. The age of M4, 11.6 Gyr, has been estimated using observations of faint cold WDs with the Hubble Space Telescope (HST) [18, 20]. This HST data, corrected for reddening and extinction, was converted into luminosities and effective temperatures in ref. [36]. From these calculations, it is possible to infer WD radii and their corresponding masses by assuming a mass-radius relation.

1.3 Neutron Stars

Being the end product of massive, $\gtrsim 8M_\odot$, stars, there are significantly fewer NSs than the WDs discussed above. As their name suggests, they are composed primarily of neutrons, which provide the degeneracy pressure required to prevent the gravitational collapse of the star. The internal structure of an NS is significantly more complicated than that of a WD. Broadly speaking, an NS can be divided into five main regions. We give an overview of the important features of each of these regions, and point the reader to Refs. [37–44] for more indepth discussions. Working from the outside in, these regions are:

Atmosphere

The atmosphere is an extremely thin layer of plasma that makes up less than 1% of the NS mass. However, it plays an extremely important role as the observed spectrum radiation emitted by the star must pass through this region [38, 39].

Outer Crust

The outer crust is the thin layer of ionized Iron-56 nuclei that extends down until the density reaches the neutron drip point, $\rho_\star = \rho_{\rm ND} \sim 4.3\times10^{11}\,\mathrm{g\,cm^{-3}}$. This is the density at which neutrons begin to drip from the nuclei as their chemical potentials approach zero. The ionized electrons form a non-relativistic but degenerate gas, with their chemical potentials increasing as the density increases. This leads to the “neutronisation” of the nuclei as the beta-capture of electrons by protons increases.

Inner Crust

The density within the inner crust spans the range between $\rho_{\rm ND} \lesssim \rho_\star \lesssim 0.5\rho_0$, with $\rho_0 \sim 2.8 \times 10^{14}\,\mathrm{g\,cm^{-3}}$ the nuclear saturation density (i.e. the density of nuclear matter) [38, 39, 45]. Here, the neutrons that have dripped from the nuclei will potentially form a superfluid. Towards the crust-core boundary, the nuclear lattice begins taking on interesting topological structures that are distinguished by the configuration of the voids in the lattice. These are known as the so-called *pasta phases* [46–48] of nuclear matter, which include 2D sheets (lasagna), cylindrical rods (spaghetti), or 3D clumps (gnochi). Eventually, towards the crust-core interface the nuclear matter transitions into a uniform medium[4].

Outer Core

Once densities go above $0.5\rho_0$, the nuclear clusters will dissolve into a homogenous fluid that is composed of neutrons, protons, electrons, and muons known as *npeμ* matter. The relative abundances of the species, $Y_i = n_i/n_b$, are dictated by the conditions of electrical neutrality and beta-equilibrium. Charge neutrality dictates that the abundances of the charged particles obeys

$$Y_p = Y_e + Y_\mu, \tag{1.42}$$

while beta-equilibrium refers to the balance between the weak decays of neutrons and the electron/muon capture by the protons,

$$n \to p + \ell^- + \bar{\nu}_\ell, \tag{1.43}$$
$$p + \ell^- \to n + \nu_\ell, \tag{1.44}$$

with $\ell = e, \mu$. Muons will begin to replace electrons in these reactions once the electron chemical potential exceeds the mass of the muon, $\mu_{F,e} \gtrsim m_\mu = 105.7\,\mathrm{MeV}$. As neutrinos are assumed to escape the NS once produced, the relation between the chemical potential of the leptons is simply

$$\mu_{F,e} = \mu_{F,\mu}. \tag{1.45}$$

The outer core region ends once the density reaches $\rho_\star \sim 2\rho_0$, and we transition into the inner core.

Inner Core

The densities within the inner cores of NSs extend between $2\rho_0 \lesssim \rho_\star \lesssim (10-15)\rho_0$ and are hence a mystery to this day. As the density greatly exceeds any

[4]The nuclear minestrone, if you will.

material that can be produced in a laboratory, the exact composition of this region is unknown and depends on the equation of state one adopts to describe it. Some of the more well-known candidates are

- A hyperonic matter component, i.e. nucleons containing a valence strange quark. These appear once the neutron chemical potential equals that of the Λ^0 hyperon, with the Ξ^- appearing once its chemical potential equals the sum of the chemical potentials of the neutrons and electrons [40, 49].

- Pion/Kaon condensates. These are Bose-Einstein condensates of pion/kaon-like excitations [50–55].

- A quark-gluon plasma comprised of deconfined u, d and s quarks and gluons [56–58].

1.3.1 Observational Status

Unlike the WDs discussed above, there are significantly fewer NS observations to constrain the EoS. However, recent years have seen significant strides in furthering our understanding of matter at super-nuclear densities, both from a theory and observational standpoint. On the theoretical side, these advances come from developments in chiral EFT allowing more detailed modelling of nuclear interactions [59–61]. The observational data has been bolstered thanks to the onset of gravitational wave astronomy due to the LIGO-VIRGO experiment [62–64] and the launch of the Neutron star Interior Composition Explorer (NICER) X-ray timing instrument.

Ultimately, what is needed to further constrain the NS EoS are more precise observations of NS masses and radii, which can be obtained from various observational techniques. NS masses have historically been much easier to measure than their radii. In particular, masses of NSs in binary systems can be precisely determined as the underlying gravitational theories are well-understood today [42, 43, 65–67]. The radii must be determined by assuming the NSs emit a blackbody spectrum, however, this method is only reliable for cool NSs where the atmospheric models are well understood [67].

The NICER experiment can provide much more precise measurements of NS radii than previous methods. This is achieved ny measuring the X-ray pulse profiles of pulsars, that are sensitive to how light bends around the star. This provides information on the compactness of the star, $GM_\star/R_\star c^2$, that can be used to determine $M_\star$ and $R_\star$ given that the mass can usually be determined through other means. The heaviest NS observed to date, the millisecond pulsar PSR J0740+6620 [68, 69], had its mass determined by measuring the relativistic Shapiro time delay [70][5] of the radio signal, allowing the radius to be obtained once the compactness was measured [71]. Refined analyses result in a mass of $2.08{\pm}0.07 M_\odot$ [72] and a radius of $12.39^{+1.30}_{-0.98}$ km [69] or $13.71^{+2.61}_{-1.50}$ km [68] at 68% confidence levels.

Gravitational wave astronomy offers an alternative and independent determination of NS masses and radii to the electromagnetic observations above. The best candidate events for this analysis are NS binary mergers, though these are expected to be an uncommon occurrence. As the NSs inspiral toward each other, they will begin to deform due to the tidal forces they induce on one another [73]. This deformation will alter the waveform observed at the detectors, with the shift in the phase of the waveform depending on the mass ratio, $q = M_2/M_1 < 1$, the chirp mass of the system, $\mathcal{M}_{\rm chirp} = (M_1 M_2)^{3/5}/(M_1 + M_2)^{1/5}$, and a combination of the tidal deformabilities, $\tilde{\Lambda}$. The latter refers to how susceptible the star is to deformation due to tidal forces acting upon it, with larger values corresponding to less compact objects. Comparing the observed waveform to that determined from precise numerical simulations allows constraints to be placed on these parameters, and ultimately on the masses and radii of the merging NSs.

Furthermore, the electromagnetic emission from the remnant object provides information about the maximum mass an NS can achieve. If the mass of the remnant object is too large, it will collapse into a black hole, and it is highly unlikely that a gamma-ray burst will occur. If the remnant does not immediately collapse, then its mass and how it is rotating determines whether it will be hydrodynamically stable, unstable, or metastable against gravitational collapse. A remnant that undergoes differential rotation[6] can support heavier masses than one that is uniformly rotating. Hence, the afterglow spectrum can inform us as to how the star is rotating. Comparing the maximum mass supported by this rotation to the initial mass after inspiral yields an upper bound on the maximum NS mass achievable.

To date, the only confirmed NS-NS merger is the merger event GW170817 observed at LIGO-VIRGO in 2017 [63, 64], with the gamma-ray burst counterpart signal observed at the Fermi Gamma-ray Burst Monitor and INTEGRAL satellite [62]. These observations led to the constraint that the radius of a $1.4 M_\odot$ NS has an upper bound of $R_{1.4} < 13.3$ km [74, 75], and that the maximum NS mass must be $M_{\rm NS}^{\rm MAX} < 2.18 M_\odot$ [62]. These constraints on the neutron star mass-radius relation are shown as the shaded turquoise and red regions of Fig 1.3.

[5]This refers to the time it takes for light to move out of a gravitational well taking longer than the naive Newtonian prediction due to the curvature of space-time.

[6]This is when components of the star at different latitudes have different angular velocities.

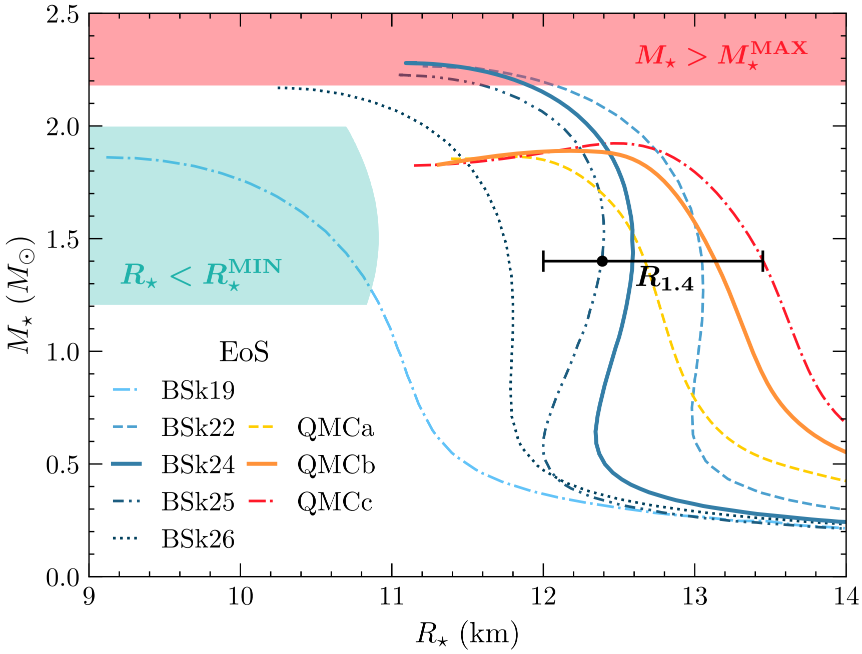

Figure 1.3: Neutron Star Mass-Radius relation predicted by the BSk (blue lines) and QMC (red lines) EoSs. Constraints obtained from the gravitational wave event GW170817 are shown as the shaded regions, with the lower bound on the radius in turquoise, and the maximum NS mass possible in red. The line band labeled $R_{1.4}$ indicates the constraints on the radius of a 1.4 $M_\odot$ NS.

1.3.2 Neutron Star Equations of State

Given the scarce constraints that have been placed on the NS mass-radius relation, there are numerous equations of state in the literature that can be used to incorporate the internal structure into our calculations. In this work, we adopt two different EoSs, which we detail here.

The Brussels-Montreal EoS

The first family of EoSs adopted in this work are based on the Brussels-Montreal (BSk) energy density functionals [76–81], for cold, non-accreting NSs. In these models, the density-dependent nucleon interactions are accounted for via a mean-field approximation in either the Hartree-Fock (HF) or Hartree-Fock-Bogoliubov (HFB) formalism[7], through effective Skyrme type forces [82, 83]. The BSk EoS family are unified EoSs, meaning they describe all the regions of the NS interior using the single effective Hamiltonian. Furthermore, the authors provide public `FORTRAN` subroutines that implement fits to the EoS quantities such as the pressure and density as functions of the baryon number density, allowing straightforward implementation of the EoS.

The authors provide these fits to eight configurations of the BSk EoS, labeled BSK19-26. Of these, the older BSK19-21 functionals were fitted to older atomic mass data that has since been updated in the newer models, BSk22-26. The mass-radius relation predicted by a selection of these models is shown in Fig. 1.3 by the blue lines. Missing are the BSk20 and 21 models, as they give very similar results to the 26 and 24 models respectively. The BSk19 EoS is partially ruled out from the lower bound on NS radii obtained from the electromagnetic counterpart of the GW170817 event [84], while BSk22 is ruled out from constraints on the tidal deformability from the same event [85]. Additionally, BSk22 does not support the presence of direct Urca[8] processes in NSs described by this EoS. These processes are required to explain observations of a small population of NSs that have cooled to temperatures below those predicted by the "minimal cooling paradigm" [86, 87]. On the other hand, the BSk26 functional predicts that all stable NSs will support direct Urac processes. This goes against the current observational evidence that a majority of NSs are well modeled by the minimal cooling paradigm, ruling the EoS out. Of the remaining two models, BSk24 and 25, we choose to adopt BSk24 as it gives slightly better fits to NS mass data than that of BSk25.

We use the BSk24 EoS to generate four benchmark NSs with masses of 1, 1.5, 1.9 an 2.16 $M_\odot$, with the central density ρ_c, stellar mass, radius, metric factor

[7]The HF method accounts for the energy associated with nucleon pairings, while the HFB method neglects this contribution.

[8]This is another name given to the reactions in Eqs. 1.43, 1.44.

EoS	BSk24-1	BSk24-2	BSk24-3	BSk24-4
ρ_c [g cm^{-3}]	5.94×10^{14}	7.76×10^{14}	1.04×10^{15}	1.42×10^{15}
$M_\star$ [$M_\odot$]	1.000	1.500	1.900	2.160
$R_\star$ [km]	12.215	12.593	12.419	11.965
$B(R_\star)$	0.763	0.648	0.548	0.467
$c_s(0)$ [c]	0.511	0.628	0.734	0.835

Table 1.2: Benchmark NSs, for four different configurations of the equations of state (EoS) for cold non-accreting neutron stars with Brussels–Montreal functionals BSk24 [81]. EoS configurations are determined by the central mass-energy density ρ_c.

$B(R_\star)$ and central speed of sound $c_s(0)$ in Table 1.2. Radial profiles of the baryon number density $n_b(r)$, metric factor $B(r)$, neutron chemical potential $\varepsilon_{F,n}(r)$, and neutron abundance $Y_n(r)$, are shown in Fig. 1.4.

While BSk24 and 25 lie well within current observational constraints, they are minimal models in that they only account for $npe\mu$ matter, and do not incorporate any exotic species within the NS core. This is problematic as it is highly likely that hyperonic matter will appear in the cores of NS heavier than $\sim 1.7\ M_\odot$. Additionally, the Skyrme forces that describe the nuclear interaction are treated non-relativistically, while the nucleons in heavier stars can become semi-relativistic. To address these concerns, later works [88, 89] adopted the Quark-Meson Coupling (QMC) EoS.

The Quark-Meson Coupling EoS

The second EoS adopted is based on the QMC model of Refs. [90–93], in which baryons are described as bags of three valence quarks, with the bags themselves modeled by the MIT bag model [94]. The interactions among the baryons are described by the exchange of mesons between the valence non-strange quarks and are formulated within a relativistic mean-field Lagrangian. The exchange of the vector mesons acts as an overall shift to the energy of the baryons[9]. The scalar mean fields play a significantly more important role, modifying the effective mass of the baryons. The scalar (and also vector) couplings are density-dependent, leading to an effective mass of the baryons that varies throughout the NS. The density dependence of these couplings is equivalent to including repulsive three-body forces

[9] A simple analogy for this is how the force of an electron in an electromagnetic field is due to the exchange of photons, which are vector fields. The total energy of the electron is a shift relative to the free electron energy.

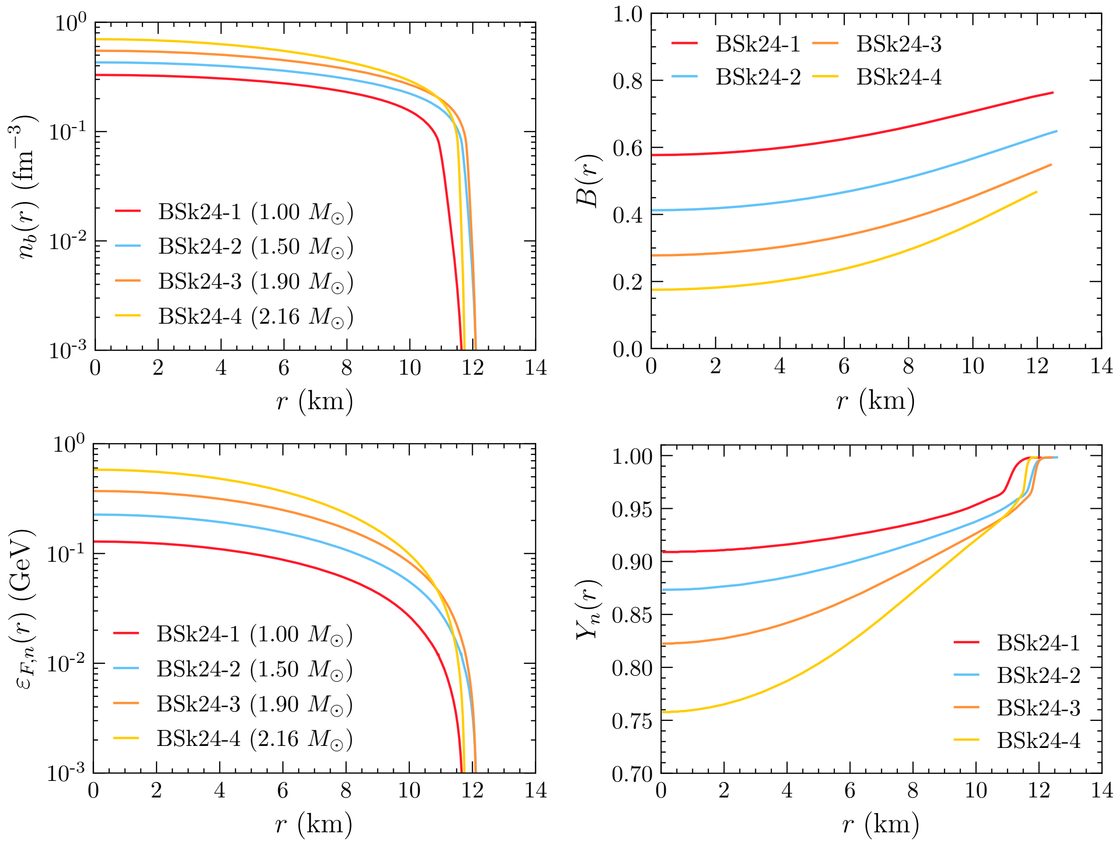

Figure 1.4: Radial profiles of the baryon number density (top left), metric factor $B(r)$ (top right), neutron chemical potential (bottom left), and neutron abundance (bottom right) for the four benchmark NS of the BSk24 EoS in Table 1.2.

EoS	QMC-1	QMC-2	QMC-3	QMC-4
$n_{\mathcal{B}}^{c}$ [fm^{-3}]	0.325	0.447	0.540	0.872
$M_\star$ [$M_\odot$]	1.000	1.500	1.750	1.900
$R_\star$ [km]	13.044	12.847	12.611	12.109
$B(R_\star)$	0.772	0.653	0.588	0.535

Table 1.3: Benchmark NSs for four different configurations of the QMC equation of state. EoS configurations are determined by the central number density $n_{\mathcal{B}}^{c}$.

between the baryons and arises naturally in the QMC model through the in-medium modification of the baryonic structure [95, 96]. Additional details on the energy density and couplings of the QMC model adopted in this work are given in Appendix **??**.

The mass-radius relation of three different configurations of the QMC EoS, namely three different choices of the isovector coupling constant, are shown as the red lines in Fig. 1.3, obtained from Ref. [97]. Of these, QMCb (orange solid line in Fig. 1.3) lies within the constraints on the radius of a 1.4 $M_\odot$ NS from GW170817, and can produce an NS of mass $1.908 \pm 0.016\ M_\odot$, the currently preferred mass of PSR J1614-2230 obtained by the NANOGrav collaboration [98][10].

The QMCb EoS data was provided by the authors of Ref. [97] for use in this work and will be referred to as simply the QMC EoS from here on. From this, we calculate the internal structure of four benchmark QMC NSs, similar to the BSk models of Table 1.2, with the central baryon density replacing the central density and the speed of sound omitted. The relevant parameters are shown in Table 1.3. The top four plots in Fig. 1.5 show the radial profiles for the number densities of the neutrons and protons for each configuration on the left, with their effective masses shown on the right. The bottom two plots of the same figure show the number densities for each species within the heaviest star on the left, including leptons in dashed lines, with the effective masses for each of the baryons on the right. The replacement of high-momentum neutrons with low-momentum hyperons is clearly seen in the bottom left plot, as the neutron number density dips towards the centre of the massive star. As the densities are high enough for the charged hyperon Ξ^- to appear, the abundance of leptons decreases due to the requirement of charge neutrality, also seen in this plot.

[10]As mentioned above, the current heaviest NS has a mass of $2.08 \pm 0.07 M_\odot$ though the implications of this on the QMC EoS are beyond the scope of this work.

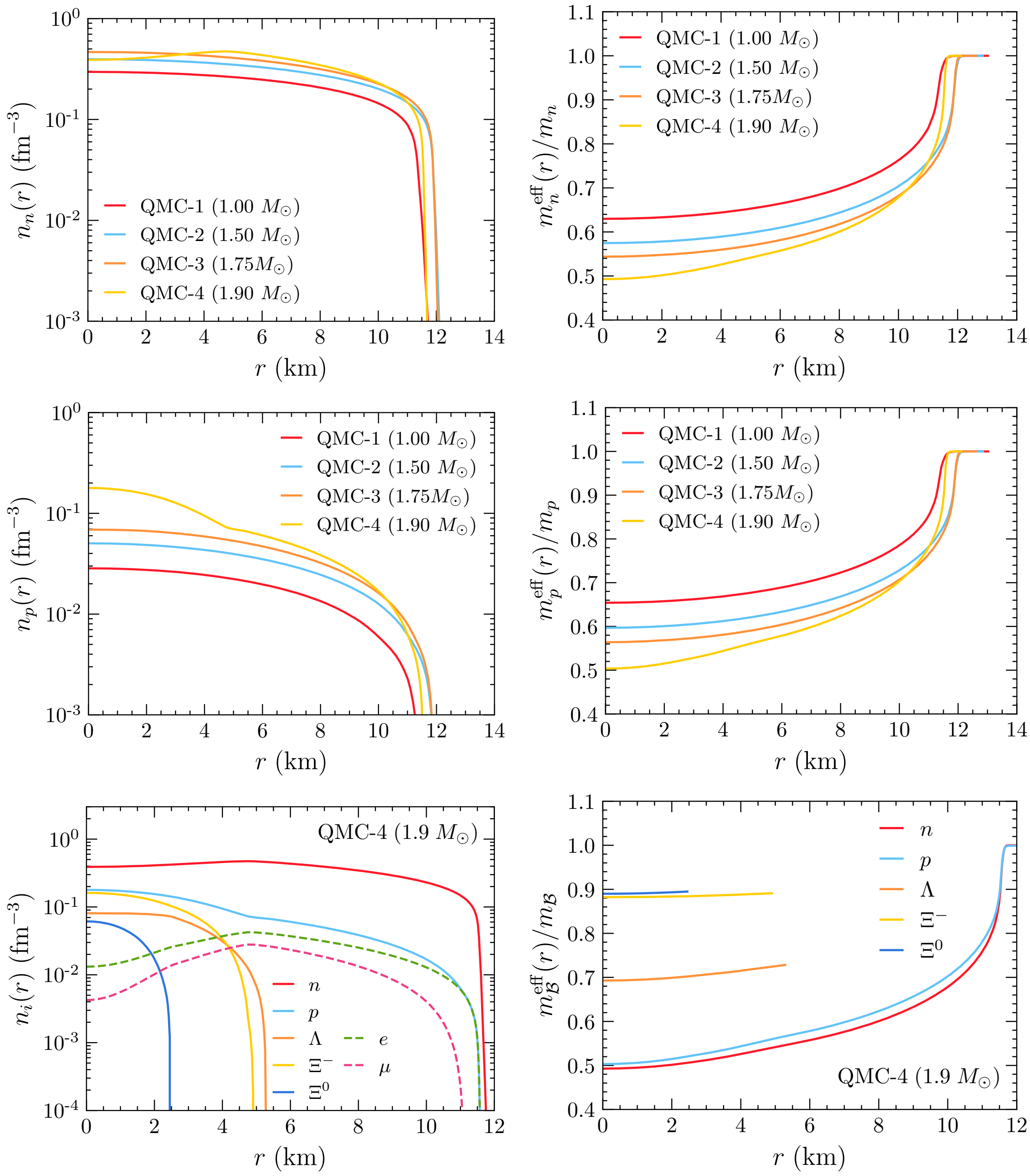

Figure 1.5: Number density profiles (left) and the ratio of the effective mass to the bare mass (right) for neutrons (top) and protons (middle) for benchmark configurations of the QMC EoS in Table 1.3. In the bottom panels, we show the same profiles for all species in the heaviest NS considered, QMC-4, which contains hyperonic matter.

2

Improved Treatment of Dark Matter Capture in Compact Objects

This chapter combines aspects of Refs. [88, 99, 100] to give a complete introduction to the formalism we have built for dark matter capture in compact objects. We begin by reviewing aspects of Gould's formalism for capture in the Sun [101, 102]. We then build upon these results to incorporate relativistic corrections and the effects of Pauli Blocking due to scattering from a degenerate media in a self-consistent manner. Important aspects of both the interaction and capture rates are discussed, including Pauli blocking for low mass DM and the effects of multiple scatting in the high-mass regime. We then apply our results to the example DM scattering from neutron targets using the BSk24 EoS to model the neutron star.

2.1 Dark Matter Capture in the Sun

Before jumping into the capture formalism relevant to compact objects, it will serve us well to review the formalism laid out by Gould for capture in the Sun [101, 102].

To begin, we consider the flux of dark matter particles that pass through a spherical shell a large distance R from the star, where the gravitational field is negligible. For this, we need to know the distribution function of the relative velocity between the DM and the stellar constituents. The velocity distribution function will be spatially isotropic, and so for simplicity we will assume that the

DM follows a Maxwell-Boltzmann distribution function,

$$f_\infty(\tilde{u}_\chi)d\tilde{u}_\chi = 4\pi \left(\frac{3}{2\pi}\right)^{3/2} \frac{\tilde{u}_\chi^2}{v_d^2} \exp\left(-\frac{3\tilde{u}_\chi^2}{2v_d^3}\right) d\tilde{u}_\chi, \tag{2.1}$$

where $\tilde{u}_\chi$ is the DM velocity in the halo, and v_d is the DM halo velocity dispersion.

Taking into account the motion of the star through the halo and the thermal motion of the constituents, which are assumed to follow a Maxwell-Boltzmann distribution, gives the relative velocity between the DM and targets, u_χ. The distribution function for the relative velocity can be expressed as [103]

$$f_{\rm MB}(u_\chi, T_\star)du_\chi = \frac{u_\chi}{v_\star}\sqrt{\frac{3}{2\pi(v_d^2+3T_\star/m_i)}}\left(e^{-\frac{3(u_\chi-v_\star)^2}{2(v_d^2+3T_\star/m_i)}} - e^{-\frac{3(u_\chi+v_\star)^2}{2(v_d^2+3T_\star/m_i)}}\right)du_\chi, \tag{2.2}$$

where $v_\star$ is the star's velocity in the halo rest frame[1], $T_\star$ is the temperature of the star, and m_i is the mass of the target.

Returning to the large spherical shell of radius R, given the velocity distribution function, we can obtain the flux of DM through this surface. The rate of DM particles passing through a surface element $d\tilde{A}$ with velocity between u_χ and $u_\chi + du_\chi$, with an angle to the normal of $d\tilde{A}$ between $\tilde{\theta}$ and $\tilde{\theta}+d\tilde{\theta}$ and an azimuthal angle between $\tilde{\phi}$ and $\tilde{\phi}+d\tilde{\phi}$ is given by [104]

$$\begin{aligned}
\frac{dN_\chi}{dt} &= \frac{\rho_\chi}{m_\chi} f_{\rm MB}(u_\chi, T_\star)\vec{u}\cdot d\vec{\tilde{A}}\, du_\chi \frac{d\tilde{\Omega}}{4\pi} && (2.3)\\
&= \frac{\rho_\chi}{m_\chi} f_{\rm MB}(u_\chi, T_\star)u_\chi \cos\tilde{\theta}\, d\tilde{A}\, du_\chi \frac{d\cos\tilde{\theta}\, d\tilde{\phi}}{4\pi} && (2.4)\\
&= \frac{1}{4}\frac{\rho_\chi}{m_\chi} f_{\rm MB}(u_\chi, T_\star)u_\chi d\tilde{A}\, du_\chi\, d\cos^2\tilde{\theta}, && (2.5)
\end{aligned}$$

where we have integrated over the azimuthal angle $\tilde{\phi}$ due to the isotropy of the system. The number density of the DM is included through the ρ_χ/m_χ factor. Integrating over the area of the sphere is trivial due to isotropy, leaving us with

$$\frac{dN_\chi}{dt} = \pi\frac{\rho_\chi}{m_\chi} f(u_\chi, T_\star)u_\chi\, du_\chi\, d\cos^2\tilde{\theta}, \tag{2.6}$$

with the integration interval for $\cos^2\tilde{\theta}$ being $(0, 1)$.

[1]This is the frame where the DM has an average velocity of zero.

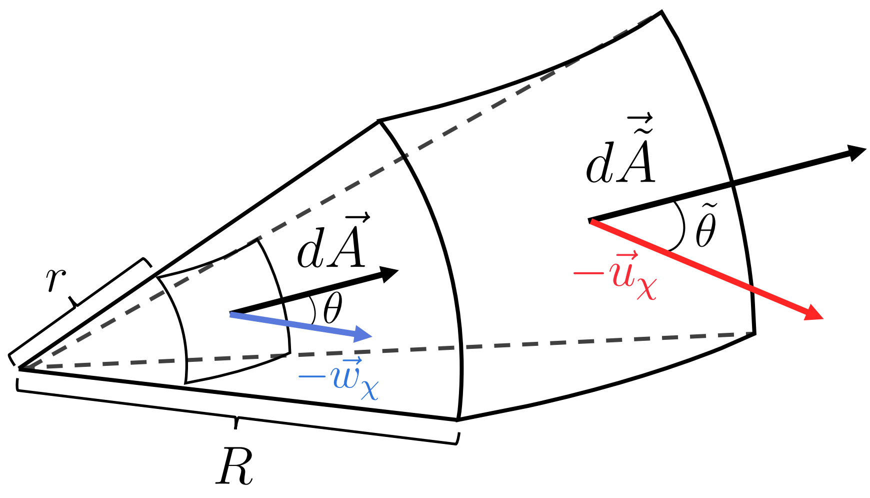

Figure 2.1: Geometry of the capture process, showing two elements of spheres with radii r close to the star

As the DM begins to infall from this large distance R to a closer distance r, the star's gravitational field will boost the velocity by the local escape velocity $v_e(r)$ such that

$$w_\chi^2(r) = u_\chi^2 + v_e^2(r), \tag{2.7}$$

$$v_e^2(r) = \frac{2GM_\star}{R_\star} + \int_r^{R_\star} \frac{GM_\star(r')}{r'^2}\, dr'. \tag{2.8}$$

Due to the conservation of angular momentum, we can relate the angular momentum of the DM at the two distances R and r such that

$$J_\chi = m_\chi R u_\chi \sin\tilde{\theta} = m_\chi r w_\chi(r) \sin\theta \leq m_\chi r w_\chi(r) \equiv J_{\max}, \tag{2.9}$$

where θ is the incident angle of the DM at the closer distance r, and we have defined the maximum angular momentum $J_{\max}$ corresponding to a linear DM trajectory.

Changing integration variables from $\cos^2\tilde{\theta}$ to J_χ allows us to write the number of DM particles passing through the shell per unit volume as

$$\frac{dN_\chi}{dt} = 2\pi \frac{\rho_\chi}{m_\chi} \frac{f_{\rm MB}(u_\chi, T_\star)}{u_\chi} r^2 w_\chi^2(r) \frac{J_\chi dJ_\chi}{J_{\max}^2}\, du_\chi. \tag{2.10}$$

The geometry of the system is shown in Fig. 2.1 for clarity.

The probability that the DM interacts with the constituents of the shell depends on the interaction rate, $\Omega(w_\chi)$, multiplied by the time spent in the shell, $dt = dr/\dot{r}$. Hence, the probability of scattering within the shell is

$$\Omega(w_\chi)\frac{dr}{\dot{r}} = 2\Omega(w_\chi)\frac{1}{w_\chi}\left(1-\left(\frac{J_\chi}{rw_\chi}\right)^2\right)^{-1/2}\Theta(J_{\max}-J_\chi)\,dr, \tag{2.11}$$

where the factor of 2 is due to the DM having two opportunities to pass through the shell, once when incoming and another after turning around[2]. The step-function is put in to ensure the angular momentum does not exceed its maximum allowed value.

For a scattered DM to be considered captured, it must lose enough energy in the collision to become gravitationally bound. The rate at which a DM particle scatters from an initial velocity w_χ to a final velocity $v < v_e(r)$ is given by [101–103]

$$\Omega^-(w_\chi) = \int_0^{v_e} R^-(w_\chi \to v)dv, \tag{2.12}$$

$$R^-(w_\chi \to v) = \int n_T(r)\frac{d\sigma_{\chi T}}{dv}|\vec{w}_\chi - \vec{u}_T| f_T(u_T)\, d^3\vec{u}_T, \tag{2.13}$$

with $R^-(w_\chi \to v)$ being the differential interaction rate, n_T is the target number density, u_T is the target velocity and $f_T(u_T)$ is the corresponding distribution function, and $d\sigma_{\chi T}/dv$ is the differential cross-section. The minus superscript is used to signify that this is the down scattering rate, i.e. the rate of interactions leading to the DM losing energy.

Finally, we obtain the capture rate by multiplying Eqs. 2.10 and 2.11 and integrate over the angular momentum to give the result

$$C = \int_0^{R_\star} dr\, 4\pi r^2 \int_0^\infty du_\chi \frac{\rho_\chi}{m_\chi}\frac{f_{\rm MB}(u_\chi, T_\star)}{u_\chi} w_\chi(r)\Omega^-(w_\chi). \tag{2.14}$$

This result is rather generic, as the choice of DM model will only dictate the form of the differential cross-section in Eq. 2.13. As written above, the distribution function for the relative velocity far from the star can be any isotropic distribution function. The MB form was chosen as it allows for a simple analytic form of the total capture rate.

[2]The radial velocity $\dot{r}$ is a standard result in orbital mechanics and can be obtained from the central force Lagrangian.

2.2 Capture in Compact Objects

Having reviewed the capture process in non-relativistic stars, we can begin discussing the necessary modifications required when considering relativistic stars. In this section, we consider the two major modifications that need to be made:

- The corrections from General Relativity due to the extreme gravitational fields. This ultimately alters the flux of DM passing through the star, boosting it through gravitational focusing.
- Accounting for the relativistic and degenerate nature of the star's constituents in the interaction rate.

The former is generic to neutron stars and white dwarfs, while the latter is required for all NS constituents, but only the electrons in a WD are degenerate and relativistic. The ions of the WD are non-relativistic and non-degenerate and, hence, can the solar capture formalism can be applied in this case.

2.2.1 General Relativistic Corrections to the Capture Rate

Far from the star, the physics is the same as in the previous section. The deviations arise as the DM falls into he gravitational potential of the star. We begin by following the DM along its trajectory, moving from a distance $R \gg R_\star$ to a closer distance r. Hence, we are working in the DM rest frame and calculating the rate at which the DM passes through the shell *per unit of proper time*, τ. The proper time interval is related to the metric through

$$d\tau^2 = B(r)dt^2 - A(r)dr^2 - r^2 d\Omega^2, \tag{2.15}$$

with $B(r)$ and $A(r)$ defined in Chapter 1.

Following the same arguments as in the non-relativistic case, the flux of DM passing through the shell is

$$\frac{dN_\chi}{d\tau} = 2\pi \frac{\rho_\chi}{m_\chi} \frac{f_{\rm MB}(u_\chi)}{u_\chi}\, du_\chi\, \frac{J_\chi\, dJ_\chi}{m_\chi^2}, \tag{2.16}$$

which takes the same form as Eq. 2.10, with the physical difference being that this is the rate with respect to the proper time. Additionally, as we will be considering cold stars, we take the $T_\star \to 0$ limit of the DM-target relative velocity distribution, such that

$$f_{\rm MB}(u_\chi) = \lim_{T_\star \to 0} f_{\rm MB}(u_\chi, T_\star) \tag{2.17}$$

$$= \frac{u_\chi}{v_\star}\sqrt{\frac{3}{2\pi(v_d^2 + 3T_\star/m_i)}}\left(e^{-\frac{3(u_\chi - v_\star)^2}{2(v_d^2+3T_\star/m_i)}} - e^{-\frac{3(u_\chi + v_\star)^2}{2(v_d^2+3T_\star/m_i)}}\right), \tag{2.18}$$

The probability that DM scatters within the shell and is captured is $2\hat{\Omega}^-(r)d\tau$, where $\hat{\Omega}^-(r)$ is the interaction rate with respect to the proper time, and $d\tau$ is the proper time taken to move from coordinate r to $r+dr$. The factor of 2 once again accounts for the DM crossing the shell twice per orbit. For calculation purposes, we need to relate this to the interaction rate seen by a distant observer, $\Omega^-(r)$, that is done through

$$\hat{\Omega}^-(r)d\tau = \frac{1}{\sqrt{g_{tt}}}\Omega^-(r)d\tau = \frac{1}{\sqrt{B(r)}}\Omega^-(r)d\tau. \tag{2.19}$$

Now, the proper time that the DM spends inside a shell of thickness dr will be[3]

$$d\tau = \left(\frac{d\tau}{dt}\right)dt = B(r)\frac{dr}{\dot{r}} = \frac{\sqrt{B(r)}dr}{\sqrt{\frac{1}{A(r)}\left[1 - B(r)\left(1 + \frac{J_\chi^2}{m_\chi^2 r^2}\right)\right]}}. \tag{2.20}$$

The differential capture rate can then be written as

$$dC = 2\pi\frac{\rho_\chi}{m_\chi}\frac{f_{\rm MB}(u_\chi)}{u_\chi}\,du_\chi\,\frac{dJ_\chi^2}{m_\chi^2}\frac{\Omega^-(r)\sqrt{A(r)}\,dr}{\sqrt{1 - B(r)\left(1 + \frac{J_\chi^2}{m_\chi^2 r^2}\right)}}. \tag{2.21}$$

As the total number of targets in the star, N_T, needs to satisfy

$$N_T = \int_0^{R_\star} 4\pi r^2 n_T(r)\sqrt{A(r)}\,dr, \tag{2.22}$$

where $n_T(r)$ is the number density that appears in the interaction rate, we absorb the factor $\sqrt{A(r)}$ into the definition of $n_T(r)$, such that $\Omega^-(r)\sqrt{A(r)} \to \Omega^-(r)$. This is due to the number densities obtained by solving the TOV equations already account for the $\sqrt{A(r)}$ factor.

As before, we have $w_\chi^2(r) = u_\chi^2 + v_e^2(r)$, however as the escape velocity will be significantly larger than the ambient DM velocity far from the star, we can safely approximate $w_\chi^2(r) \approx v_e^2(r)$. In the relativistic case, the escape velocity can be defined as

$$v_e^2(r) = \left(\frac{dl}{d\tau}\right)^2 = A(r)\left(\frac{dr}{d\tau}\right)^2 + r^2\left(\frac{d\phi}{d\tau}\right)^2 = 1 - B(r), \tag{2.23}$$

where dl is a length element. The large boost from the escape velocity also removes the u_χ dependence in the kinematics of the interactions and allows us to perform the integration over the initial DM velocity, yielding an overall factor of

$$\int_0^\infty \frac{f_{\rm MB}(u_\chi)}{u_\chi}du_\chi = \frac{1}{v_\star}\,\mathrm{Erf}\left(\sqrt{\frac{3}{2}}\frac{v_\star}{v_d}\right). \tag{2.24}$$

[3]See Appendix **??** for the derivation of $\dot{r} = \frac{dr}{dt}$.

To integrate over J_χ^2, we need the maximum angular momentum the DM can achieve as it passes through the shell. This can be obtained by requiring the argument of the radical above to remain positive, giving

$$J_{\max} = \sqrt{\frac{1-B(r)}{B(r)}} m_\chi r. \tag{2.25}$$

The factor of $1/\sqrt{B}$ arises due to the gravitational focusing of the incoming flux of DM [105].

Putting everything together, and integrating over the radius of the star, we are left with the final result for the capture rate of

$$C = \frac{4\pi}{v_\star} \frac{\rho_\chi}{m_\chi} \operatorname{Erf}\left(\sqrt{\frac{3}{2}} \frac{v_\star}{v_d}\right) \int_0^{R_\star} r^2 \frac{\sqrt{1-B(r)}}{B(r)} \Omega^-(r)\, dr. \tag{2.26}$$

All that remains is determining the form of the interaction rates for relativistic energies.

2.2.2 Geometric Limit and Threshold Cross-Section

In the previous section, we derived an expression for the capture rate assuming that the DM is captured after a single scatter, and that it only scatters once along its orbit through the NS. This first assumption is true for DM light enough to lose enough energy in this single interaction, which for nucleon targets turns out to be $m_\chi \lesssim 10^6\,\mathrm{GeV}$. The latter assumption is a statement that we are working in the optically thin regime, such that the cross-section is much less than the "threshold cross-section", $\sigma_{\rm th}$. The value of the threshold cross-section is defined as the cross-section for which the capture rate evaluated in the optically thin regime is equal to the geometric limit [106],

$$C_{\rm geom} = \frac{\pi R_\star^2 (1-B(R_\star))}{v_\star B(R_\star)} \frac{\rho_\chi}{m_\chi} \operatorname{Erf}\left(\sqrt{\frac{3}{2}} \frac{v_\star}{v_d}\right). \tag{2.27}$$

This is the capture rate for which the entire flux of DM passing through the surface of the star is captured at the surface. Hence, it serves as an upper bound to the capture rate, with cross-sections greater than $\sigma_{\rm th}$ saturating the capture rate to this value. Note the $1/B(R_\star)$ factor in the equation above. In stars and planets where classical Newtonian mechanics can be applied, gravitational focusing would result in a factor $v_{esc}^2/v_\star = (1-B(R_\star))/v_\star$ in Eq. 2.27, where we have used Eqs. 2.23 and 1.14. In neutron stars, on the other hand, general relativity introduces an additional factor of $1/B(R_\star)$, which can be obtained from the derivation of the flux of DM particles accreted to a NS with a Schwarzschild metric (Eq. 2.26) [105, 107].

For scattering on neutrons, the threshold cross-section is approximately

$$\sigma_{th} = \begin{cases} \sigma_{\rm ref}\frac{\rm GeV}{m_\chi}, & m_\chi \lesssim 1\,{\rm GeV} \quad \text{(Pauli blocking regime)}, \\ \sigma_{\rm ref}, & 1\,{\rm GeV} \lesssim m_\chi \lesssim 10^6\,{\rm GeV}, \\ \sigma_{\rm ref}\frac{m_\chi}{10^6\,{\rm GeV}}, & m_\chi \gtrsim 10^6\,{\rm GeV} \quad \text{(Multiscattering regime)}, \end{cases} \tag{2.28}$$

where we take the canonical value of

$$\sigma_{\rm ref} \sim 1.7 \times 10^{-45}\,{\rm cm}^2, \tag{2.29}$$

which assumes the NS is a solid sphere such that $\sigma_{\rm ref} \sim m_n \pi R_\star^2/M_\star$ with m_n the neutron mass.

For scattering off other targets, Pauli blocking is relevant for $q_0^{\rm MAX} \lesssim \mu_{\rm target}$ while multi-scattering is relevant for $m_\chi \gtrsim q_0^{\rm MAX}/v_\star^2$, where $q_0^{\rm MAX}$ is the maximum energy transfered in a collision, as will be discussed later. In addition, because the other target species have a lower abundance than neutrons, the reference cross-section, $\sigma_{\rm ref}$, will be higher. The values of σ_{th} in Eq. 2.28, and their regions of applicability, can thus be altered appropriately for other target species of interest.

2.2.3 Interaction Rate for Relativistic Energies and Degenerate Targets

Our next goal is to write down an interaction rate suitable for describing the interactions between relativistic particles and account for the degeneracy of the target species. This will be achieved by modifying the non-relativistic interaction rate of Eq. 2.12 through the use of relativistic kinematics and the use of Lorentz invariant quantities, and the correct distribution functions for degenerate fermion targets.

As shown in Eqs. 2.12 and 2.13, the interaction rate between non-relativistic, non-degenerate species i can be expressed as

$$\Omega^-(r) = \int dv \frac{d\sigma}{dv}|\vec{w}_\chi - \vec{u}_i| n_i(r) f_{\rm MB}(u_i) d^3u_i. \tag{2.30}$$

First, we address the degeneracy of the targets by exchanging the Maxwell-Boltzmann distribution function for a Fermi-Dirac (FD) distribution, $f_{\rm FD}(E_i, r)$, via the replacement

$$n_i(r) f_{\rm MB}(u_i) d^3u_i \to \frac{g_s}{(2\pi)^3} f_{\rm FD}(E_i, r), \tag{2.31}$$

where $g_s = 2$ is the number of spin states of the target species, p is the 3-momentum of the incoming target, and E_i is its corresponding energy. The radial dependence of the FD distribution stems from its implicit dependence on the chemical potential of the target. Rewriting this expression in a more computationally friendly manner in terms of the relevant kinematic quantities results in

$$\frac{g_s}{(2\pi)^3} f_{\rm FD}(E_i, r) = \frac{pE_i}{2\pi^2} f_{\rm FD}(E_i, r) dE_i d\cos\theta_{uw}, \tag{2.32}$$

where we have expressed the angular component of the d^3p differential in terms of the angle between the incoming DM and target. This angle can be traded for the more useful quantity s, the centre of mass energy through

$$\frac{d\cos\theta_{uw}}{ds} = \frac{1}{2pp_\chi} = \frac{1}{2p\sqrt{E_\chi^2 - m_\chi^2}} = \frac{1}{2pm_\chi}\sqrt{\frac{B(r)}{1-B(r)}}, \tag{2.33}$$

as the initial DM energy is $E_\chi = m_\chi/\sqrt{B(r)}$.

Next, we calculate the initial relative velocity, $|\vec{w}_\chi - \vec{u}_i|$, using relativistic kinematics, expressing it in terms of the Mandalstam s,

$$|\vec{w}_\chi - \vec{u}_i| = \frac{\sqrt{s^2 - 2s(1+\mu^2)m_i^2 + (1-\mu^2)^2 m_i^4}}{s - (1+\mu^2)m_i^2}, \tag{2.34}$$

where $\mu = m_\chi/m_i$.

Given that it is most common to present the relativistic differential scattering cross-section $d\sigma/d\cos\theta_{\rm cm}$ as a function of the Mandalstam variables s and t, with $\theta_{\rm cm}$ the centre of mass frame scattering angle, we make the replacement

$$dv\frac{d\sigma}{dv} = dt\frac{d\sigma}{dt} = dt\frac{d\sigma}{d\cos\theta_{\rm cm}}\frac{d\cos\theta_{\rm cm}}{t}. \tag{2.35}$$

The final Jacobian factor can be expressed as

$$\frac{d\cos\theta_{\rm cm}}{dt} = \frac{2s}{s^2 - 2s(1+\mu^2)m_i^2 + (1-\mu^2)^2 m_i^4}, \tag{2.36}$$

for the elastic scattering we consider here.

Finally, we note that the first application of this capture formalism was for neutron targets, with the analysis completed before we had considered the additional effects from the form factors and strong interactions discussed in subsection **??**. These effects will be incorporated into this formalism in a self-consistent way next chapter. The initial approach that was taken to account for the fact that we are using realistic neutron number density profiles, despite the expression in Eq. 2.31 being for a free Fermi gas, is to introduce a correction factor as in Ref. [108],

$$\zeta(r) = \frac{n_i(r)}{n_{\rm free}(r)}, \tag{2.37}$$

where $n_{\rm free}(r)$ is obtained by integrating Eq. 2.32 over all phase space. In the zero-temperature approximation, the result is

$$n_{\rm free}(r) = \frac{1}{3\pi^2}\left[\varepsilon_{F,i}(r)(2m_i + \varepsilon_{F,i}(r))\right]^{3/2}. \tag{2.38}$$

Compiling everything together leads to the final expression for the interaction rate being

$$\begin{aligned}\Omega^-(r) = \int dt\, dE_i\, ds\, \zeta(r) \frac{d\sigma}{d\cos\theta_{\rm cm}} \frac{E_i}{2\pi^2 m_i} \sqrt{\frac{B(r)}{1-B(r)}} \frac{s}{\beta(s)\gamma(s)} \\ \times f_{\rm FD}(E_i, r)(1 - f_{\rm FD}(E_i', r)),\end{aligned} \tag{2.39}$$

where we have introduced the helper functions

$$\beta(s) = s - (m_i^2 + m_\chi^2), \tag{2.40}$$

$$\gamma(s) = \sqrt{\beta^2(s) - 4m_i^2 m_\chi^2}. \tag{2.41}$$

We have also introduced the Pauli blocking factor, $1 - f_{\rm FD}(E_i', r)$, to account for the phase space available to the final state target. The energy of this final state particle, E_i', is in general a messy function of E_i, t, s, and r, and can be obtained from the kinematics of the scattering. This result is presented in Appendix **??**.

The integration intervals are

$$t_{\rm min} = -\frac{\gamma(s)}{s}, \tag{2.42}$$

$$t_{\rm max} = 0, \tag{2.43}$$

$$s_{\rm min} = m_i^2 + m_\chi^2 + 2\frac{E_i m_\chi}{\sqrt{B(r)}} - 2m_\chi \sqrt{\frac{1-B(r)}{B(r)}} \sqrt{E_i^2 - m_i^2}, \tag{2.44}$$

$$s_{\rm max} = m_i^2 + m_\chi^2 + 2\frac{E_i m_\chi}{\sqrt{B(r)}} + 2m_\chi \sqrt{\frac{1-B(r)}{B(r)}} \sqrt{E_i^2 - m_i^2}, \tag{2.45}$$

$$E_{i,\rm min} = m_i, \tag{2.46}$$

$$E_{i,\rm max} = \frac{m_i}{\sqrt{B(r)}}. \tag{2.47}$$

As we will be dealing with NSs at low temperatures, we can take the $T_\star \to 0$ limit and replace the FD functions with step functions,

$$f_{\rm FD}(E_i, r) \to \Theta(\varepsilon_{F,i}(r) + m_i - E_i), \tag{2.48}$$
$$1 - f_{\rm FD}(E_i', r) \to \Theta(E_i' - m_i - \varepsilon_{F,i}(r)). \tag{2.49}$$

The first step function can be used to further restrict the E_i integration interval to be $[m_i, m_i + \varepsilon_{F,i}(r)]$. In practice, we work with the kinetic energies of the targets rather than their total energy, as this is the quantity that directly changed in the interactions. Therefore, unless otherwise specified, we will take E_i to mean the target kinetic energy, with the integration range being $0 \leq E_i \leq \varepsilon_{F,i}$.

This expression resembles that of Ref. [108], but uses a relativistic formalism instead. In Appendix A.3, we show that Eq. 2.39 reduces to the classical expression for the interaction rate in the non-relativistic limit.

2.3 The Differential Interaction Rate

In the previous section, we have calculated the interaction rate, $\Omega^-(r)$, assuming the initial DM energy takes its pre-capture value, $E_\chi = m_\chi/B(r)$. However, we are also interested in an expression for the interaction rate valid for arbitrary DM energy. This will be required when we consider capture via multiple scatterings, and it will also be necessary to study the subsequent scattering interactions that follow capture and lead to the DM thermalising within the NS. In principle, it is possible to calculate this rate numerically by binning Ω^-, Eq. 2.39, in the energy loss, i.e. multiplying Ω^- by $\frac{1}{E_i - E_j}\Theta(E_i + E_i - E_i')\Theta(E_i' - E_i - E_j)$ and integrating over the bin $[E_j, E_i]$. However, it is possible to derive analytic expressions for the differential rate, valid in the zero-temperature approximation. To do so, we use the definition of the scattering rate in Ref. [109, 110]

$$\begin{aligned}\Gamma^-(E_\chi) = 2\int \frac{d^3k'}{(2\pi)^3}\int \frac{d^3p}{(2\pi)^3}\int \frac{d^3p'}{(2\pi)^3}&\frac{|\overline{\mathcal{M}}|^2}{(2E_\chi)(2E_\chi')(2E_i)(2E_i')} \\ &\times (2\pi)^4\delta^4\left(k_\mu + p_\mu - k_\mu' - p_\mu'\right) f_{\rm FD}(E_i)(1 - f_{\rm FD}(E_i')),\end{aligned} \tag{2.50}$$

where $|\overline{\mathcal{M}}|^2$ is the squared matrix element, $k^\mu = (E_\chi, \vec{k})$ and $k'^\mu = (E_\chi', \vec{k}')$ are the DM initial and final momenta, and $p^\mu = (E_i, \vec{p})$ and $p'^\mu = (E_i', \vec{p}')$ are the target particle initial and final momenta, respectively. To see that Γ^- is indeed the same as Ω^- in Eq. 2.39, multiply and divide by $v_{rel} = |\vec{w} - \vec{u}_i|$ to reintroduce the quantum field theoretic definition of differential cross-section,

$$d\sigma = \frac{|\overline{\mathcal{M}}|^2}{2E_\chi 2E_i|\vec{w}-\vec{u}_i|} d^2\Pi_{\rm LIPS}, \tag{2.51}$$

$$d^2\Pi_{\rm LIPS} = \frac{1}{2E'_\chi}\frac{d^3k'}{(2\pi)^3}\frac{1}{2E'_i}\frac{d^3p'}{(2\pi)^3}(2\pi)^4\delta^4(k_\mu + p_\mu - k'_\mu - p'_\mu), \tag{2.52}$$

$$\implies \frac{d\sigma}{d\cos\theta_{\rm cm}} = \frac{1}{16\pi}\frac{\beta(s)}{2s\beta(s)-\gamma^2(s)}|\overline{\mathcal{M}}|^2, \tag{2.53}$$

where $d^2\Pi_{\rm LIPS}$ is the 2-body Lorentz invariant phase space.

The advantage of Eq. 2.39 is that it can be used to calculate the capture rate for any interaction given the differential cross-section. The disadvantage is that this computation has to be evaluated numerically, which can be computationally intensive. For this reason, shall now use Eq. 2.50 to derive analytic expressions that will allow us to speed up computations and, in addition, calculate the shape of the interaction rate as a function of the energy loss.

The interaction rate for $d\sigma \propto s^m t^n$ is

$$\Gamma^-(E_\chi)- = \sum_{n,m}\frac{(-1)^n\alpha_{n,m}}{128\pi^3 E_\chi k}\int_0^{E_\chi - m_\chi} dq_0 \int \frac{dt_E t_E^n}{(t_E+q_0^2)^{m+\frac{1}{2}}} \times \sum_{r=0}^{m}\mathcal{V}_{m,r}\sum_{j=0}^{r}\binom{r}{j}\varepsilon_{F,i}^{r-j}\frac{(-1)^j q_0^{j+1}}{j+1}h_j\left(\frac{E_i^{t^-}-\varepsilon_{F,i}}{q_0}\right), \tag{2.54}$$

for elastic scattering with $t_E = -t = q^2 - q_0^2$, where $q_0 = E'_i - E_i$ is the DM energy loss,

$$E_i^{t^-} = -\left(m_n + \frac{q_0}{2}\right) + \sqrt{\left(m_n + \frac{q_0}{2}\right)^2 + \left(\frac{\sqrt{q^2-q_0^2}}{2} - \frac{m_n q_0}{\sqrt{q^2-q_0^2}}\right)^2}, \tag{2.55}$$

is the minimum energy of the neutron before the collision, obtained from kinematics, and $h_j(x)$ is a step function with a smooth transition,

$$h_j(x) = \begin{cases} 0, & x > 0 \\ (-x)^{j+1}, & -1 < x < 0\,. \\ 1, & x < -1 \end{cases} \tag{2.56}$$

The full derivation of this interaction rate can be found in Appendix A. Our result for Γ^- is an extension of that presented in Ref. [110], where the interaction rate was calculated only in the case of low energy and a constant matrix element. It

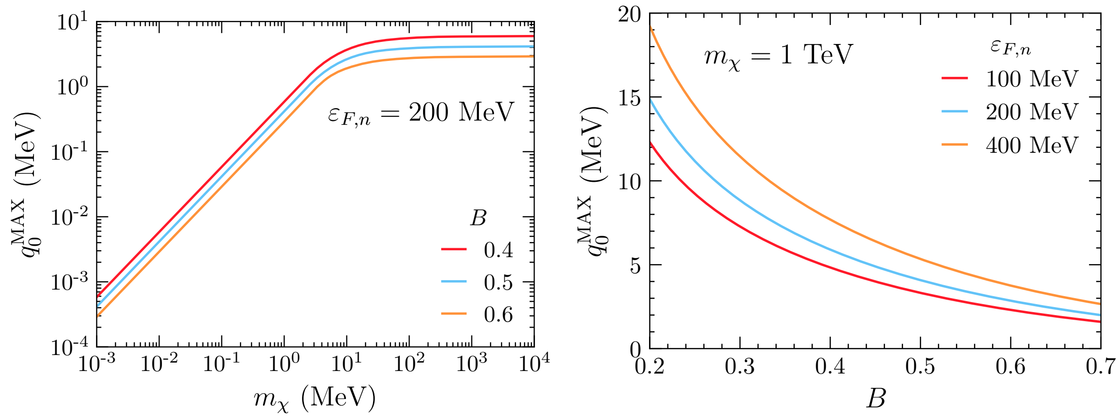

Figure 2.2: Left: $q_0^{\rm MAX}$ vs. m_χ for $\varepsilon_{F,n} = 200\,\text{MeV}$ and different values of B. Right: $q_0^{\rm MAX}$ as a function of B for different values of $\varepsilon_{F,i}$ and $m_\chi = 1\,\text{TeV}$.

is valid at all energy ranges. The differential interaction rate $\frac{d\Gamma}{dq_0}(E_\chi, q_0)$ is then just the integrand of Eq. 2.54. We will use $\frac{d\Gamma}{dq_0}$ to obtain normalised shapes for the differential interaction spectrum, while we will use Ω^- when we need the total interaction rate, such as in the capture rate.

Kinematics, and the phase space allowed by $h_j(x)$ in Eq. 2.54, determine the maximum energy that a DM particle can lose in a single scattering interaction, $q_0^{\rm MAX}$. The details of how to obtain $q_0^{\rm MAX}$ are given in Appendix A.2.1. For DM capture, the value of $q_0^{\rm MAX}$ depends primarily on the DM mass, as is illustrated in the left panel of Fig. 2.2. We can see that for low m_χ, $q_0^{\rm MAX} \propto m_\chi$, while, for $m_\chi \gg m_n$, it plataues to values between $q_0^{\rm MAX} \sim 3 - 6\,\text{GeV}$. Both $q_0^{\rm MAX}$ and $\frac{d\Gamma}{dq_0}$ also depend on $\varepsilon_{F,n}$ and B. Changing $\varepsilon_{F,n}$ has a very mild effect on the value of $q_0^{\rm MAX}$ (see right panel of Fig. 2.2) and on the shape of the normalised spectrum (see Fig. 2.3). On the other hand, increasing B has the main effect of reducing $q_0^{\rm MAX}$ (see right panel of Fig. 2.2), but only a mild effect on the shape of the profile expressed as a function of the normalised energy loss

$$q_0^{\rm norm} = \frac{q_0}{q_0^{\rm MAX}}. \tag{2.57}$$

We apply our results for $\frac{d\Gamma}{dq_0}$ to DM-neutron interactions, and in particular those with differential cross-sections that depend only on the transferred momentum $t = (k^\mu - k'^\mu)^2$ and not on the centre of mass energy $s = (p^\mu + k^\mu)^2$.

In Fig. 2.3 we show the normalised differential rates as a function of $q_0^{\rm norm}$ for the four operators D1-D4. The left-hand panels are in the limit $m_\chi \gg m_n$. We can observe that D1 has a softer spectrum, while the D2 and D4 spectra peak towards higher values of q_0. Varying the chemical potential $\varepsilon_{F,n}$ has a very mild

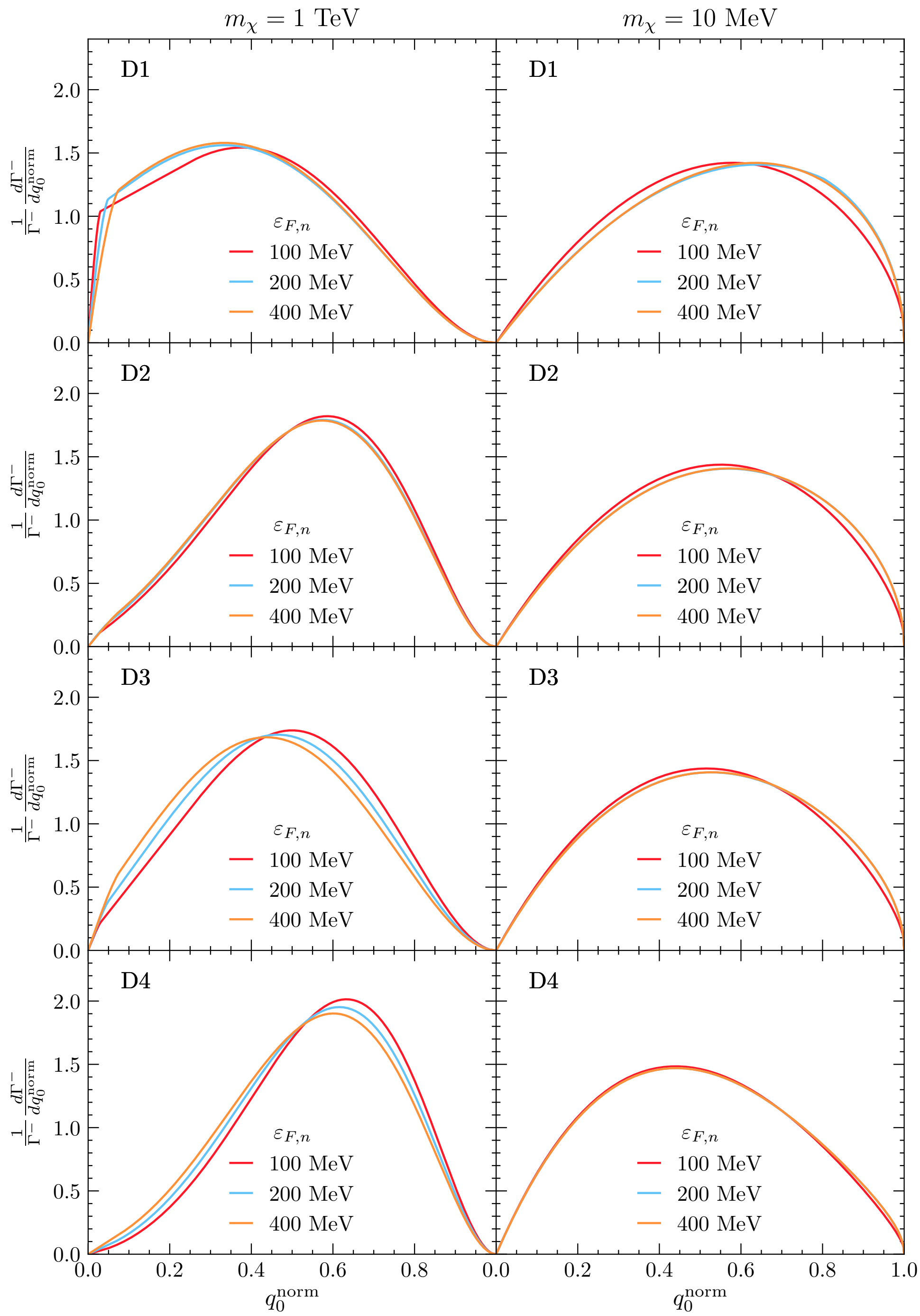

Figure 2.3: Normalised differential interaction rates $\frac{1}{\Gamma}\frac{d\Gamma}{dq_0^{\rm norm}}$ as a function of $q_0^{\rm norm}$ for different values of $\varepsilon_{F,n}$, $m_\chi = 1\,\text{TeV}$ (left) and $m_\chi = 10\,\text{MeV}$ (right), $B = 0.5$ and operators D1 (first row), D2 (second row), D3 (third row) and D4 (fourth row). Profiles do not depend on m_χ in the limits $m_\chi \gg m_n$ (left) and $m_\chi \ll m_n$ (right).

effect, shifting the spectrum to lower values of q_0 with increasing values of $\varepsilon_{F,n}$. Note that at small values of $q_0^{\rm norm}$ there is a sudden change in the slope of the normalised differential rate, which occurs for all operators but is more evident in D1 (top left panel). This is due to the zero temperature approximation, implicit in Eq. 2.54, where Heaviside functions were used to approximate FD distributions (see Appendix A.2.1); using a finite temperature would produce a smoother spectrum at small $q_0^{\rm norm}$.

In the right-hand panels of Fig. 2.3, we explore the low DM mass region $m_\chi \ll m_n$. In this case, all operators give rise to similar profiles, the sole difference being that the peak of the profile is now shifted to lower $q_0^{\rm norm}$ for D4 in contrast to D1, with intermediate values for D2 and D3. This is a consequence of Pauli blocking, with this effect depending on the specific power of t that dominates the spectrum. Profiles with lower n ($d\sigma \propto t^n$) peak at higher $q_0^{\rm norm}$ (see Fig. 2.3, right panels). For D4 we have $|\overline{\mathcal{M}}|^2 \propto t^2$, while the matrix elements of D2 and D3 are linear combinations of t and t^2, and D1 is a combination of all powers of t. Comparing the right panels of Fig. 2.3 with Fig. A.2, we observe that the lowest power of t determines the shape of the final differential interaction rate. Finally, varying $\varepsilon_{F,n}$ has a very mild effect, this time shifting the spectrum mostly to higher values of q_0 for higher $\varepsilon_{F,n}$.

The fact that the lowest power of t dictates the features of the differential interaction rate is true also for the interactions that have a dependence on s. As such, by understanding the properties of the interaction rates with $|\overline{\mathcal{M}}|^2 \propto t^n$, we can understand the rates for all the operators in Table **??**.

2.3.1 Pauli Blocking

The DM interaction rate, Eq. 2.50, will be proportional to the number of target particles available to scatter off. Classically, this is the total number of targets within the star. However, the quantum degeneracy of the species within compact objects, due to the extreme densities, leads to a reduction in the number of available initial state target particles the DM can scatter off. To understand this, consider the $T \to 0$ approximation, in which all initial states with energies $E_i < \varepsilon_{F,i}$ are occupied. These states are known as the “Fermi sea”. In order for the DM to scatter off one of these states, it must impart enough energy to kick the target out of the Fermi sea, such that

$$E_i' = E_i + q_0 > \varepsilon_{F,i}, \tag{2.58}$$

imposing a lower limit on the energy transfer required for an interaction to take place. This effectively reduces the number of available targets to only those with kinetic energies between $\varepsilon_{F,n} - q_0$ and $\varepsilon_{F,i}$. This suppression of the initial state phase space is known as Pauli blocking (PB), and is a completely quantum phenomenon. In this limit, we necessarily have $\Gamma^- \to 0$ for $q_0 \to 0$. It is also worth noting that Pauli blocking only affects the interaction rate when $q_0 \leq \varepsilon_{F,n}$.

To assess the impact of PB on the DM differential interaction rate, in Fig. 2.4 we compare the rate with (blue solid lines) and without (light blue dashed lines) Pauli blocking, for $B = 0.5$ and constant DM-neutron cross-section. When Pauli blocking can be neglected, the interaction rate is obtained straightforwardly from Eq. 2.50 by stripping away the $(1 - f_{\mathrm{FD}}(E_i'))$ factor. The difference between the computations is shaded in light blue. In the top left panel, we see that the rate begins to be suppressed from PB at $q_0 \sim \varepsilon_{F,i} = 100\,\mathrm{MeV}$ for a 1 GeV DM. In the top right plot, we increase the neutron chemical potential from $\varepsilon_{F,n} = 100\,\mathrm{MeV}$ to $\varepsilon_{F,n} = 400\,\mathrm{MeV}$. Given that in this case $q_0^{\mathrm{MAX}} \sim 0.4 m_\chi \sim 400\,\mathrm{MeV}$, almost the whole energy range is affected by PB. The higher $\varepsilon_{F,n}$ changes the spectra (both with and without PB) such that the unsuppressed rate is no longer flat at low q_0. The PB suppressed rate reaches a maximum at values of q_0 slightly below q_0^{MAX}, and then decreases towards 0 at lower q_0. In the middle panels, $m_\chi = 100\,\mathrm{MeV}$, and $q_0^{\mathrm{MAX}} \sim 40\,\mathrm{MeV} \ll \varepsilon_{F,n}$. In this case, it is evident that PB affects the spectrum over the full $q_0 = q_0^{\mathrm{MAX}}$ range. In the bottom row, we set $m_\chi = 10\,\mathrm{MeV}$. As expected, for lighter DM, the effects of PB are even more pronounced.

To understand how the effect of PB varies throughout the star, we can analyse the radial profiles of the capture rates dC/dr. In Fig. 2.5 we plot the differential capture rate as a function of the NS radius, with and without Pauli blocking. We see that Pauli blocking is most significant at low DM mass, below about 1 GeV, and becomes insignificant for higher masses. Pauli blocking has a larger impact on the differential capture rate deeper into the NS interior and has a negligible effect at the surface. This is particularly apparent in the top left panel of Fig. 2.5. This is because the chemical potential is higher in the NS interior than it is near the crust, as seen in the radial $\varepsilon_{F,i}$ profile in the bottom left panel of Fig. 1.4.

2.4 Capture in the Low, Intermediate and High Mass Regimes

Having assembled all the required machinery, we are ready to explore the properties of the capture rate in the three mass regimes outlined in Eq. 2.28. Given the computational load required to evaluate Eq. 2.26 in general, we aim to provide approximations that are numerically more efficient where possible. We also discuss the high DM mass regime where multiple scatterings are required for capture, and how this is affected by Pauli blocking.

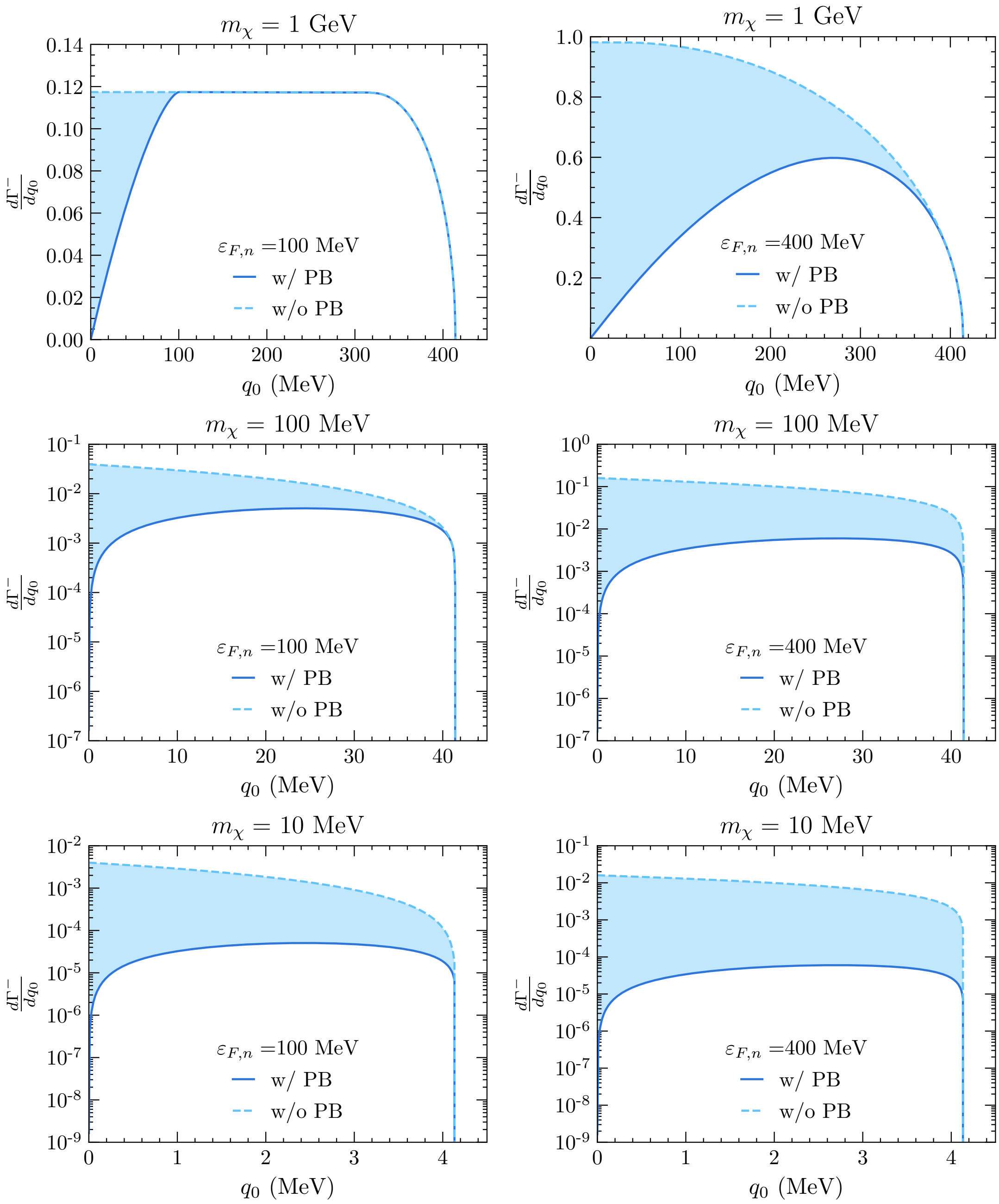

Figure 2.4: Differential interaction rates $\frac{d\Gamma}{dq_0}$ as a function of the energy loss q_0 for different values of m_χ and $\varepsilon_{F,n}$, constant cross-section and $B = 0.5$. Blue lines refer to the result that includes Pauli blocking, while the light blue dashed lines refer to the result without PB. Left column: $\varepsilon_{F,n} = 100\,\text{MeV}$, right column: $\varepsilon_{F,n} = 400\,\text{MeV}$. Top: $m_\chi = 1\,\text{GeV}$, middle: $m_\chi = 100\,\text{MeV}$, bottom: $m_\chi = 10\,\text{MeV}$.

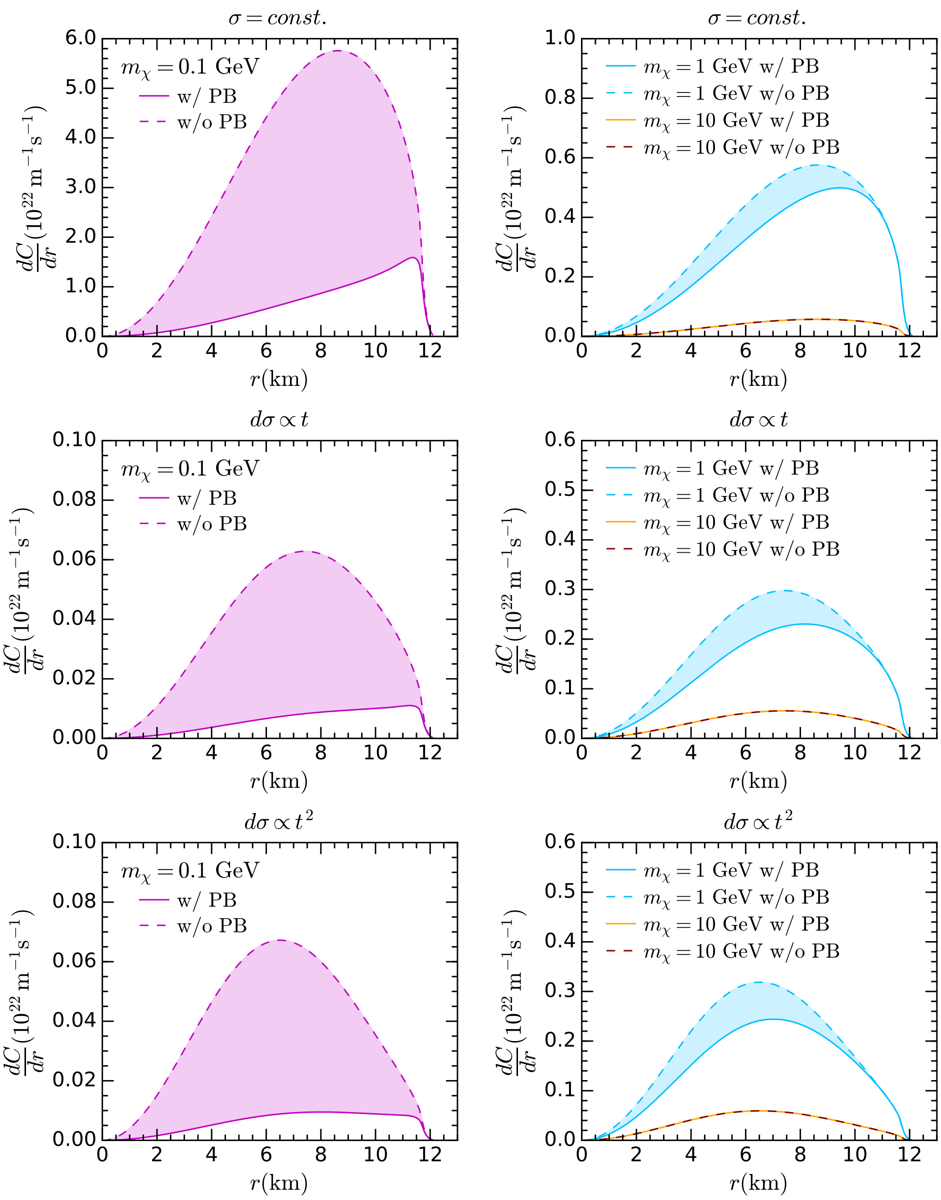

Figure 2.5: Differential capture rate as a function of the NS radius r, with (solid) and without (dashed) Pauli blocking, for the EoS benchmark BSk24-2. Top: constant cross-section, center: $d\sigma \propto t$, bottom: $d\sigma \propto t^2$.

2.4.1 Low and intermediate DM mass range

In sections 2.2 and 2.3, we have derived general expressions to numerically calculate the DM capture and interaction rates, Eqs. 2.26 and 2.39 respectively. Using these expressions, we can write the complete expression for the capture rate as a function of the differential DM-neutron cross-section

$$C = \frac{2\rho_\chi}{\pi v_\star m_\chi^2}\mathrm{Erf}\left(\sqrt{\frac{3}{2}}\frac{v_\star}{v_d}\right)\int_0^{R_\star} dr \frac{r^2\zeta(r)}{\sqrt{B(r)}}\int dt dE_i ds \frac{d\sigma}{d\cos\theta_{\rm cm}}\frac{E_i s}{\beta(s)\gamma(s)} \\ \times f_{\rm FD}(E_i,r)(1-f_{\rm FD}(E_i',r)), \tag{2.59}$$

where the functions β and γ were given in section 2.2.3. Recall that in the limit $T \to 0$, $f_{\rm FD}(E_i, r)$ and $1 - f_{\rm FD}(E_i', r)$ reduce to the step functions, $\Theta(\varepsilon_{F,i}(r) - E_i)$ and $\Theta(E_i' - \varepsilon_{F,i}(r))$, respectively.

Exchanging the differential cross-section for the squared matrix allows for easier examination of the operators in Table **??**, and so we write the capture rate as

$$C = \frac{\rho_\chi}{8\pi^2 v_\star m_\chi^2}\mathrm{Erf}\left(\sqrt{\frac{3}{2}}\frac{v_\star}{v_d}\right)\int_0^{R_\star} dr \frac{r^2\zeta(r)}{\sqrt{B(r)}}\quad\int dt dE_i ds \frac{|\overline{\mathcal{M}}|^2 E_i}{2s\beta(s)-\gamma^2(s)}\frac{s}{\gamma(s)} \\ \times f_{\rm FD}(E_i,r)(1-f_{\rm FD}(E_i',r)). \tag{2.60}$$

This expression can be used to numerically calculate the single scatter capture rate of DM in compact objects, in the optically thin regime. In general, this must be used for low-mass DM where PB is in effect.

As discussed in section 2.3.1, PB eventually becomes negligible for DM with masses $\gtrsim \mu_{F,i}$. Hence, between this mass and the point where multiple scattering becomes important, PB can be neglected and a simplified capture rate be obtained. For nucleon targets, this range is between $1\,\mathrm{GeV} \lesssim m_\chi \lesssim 10^6\,\mathrm{GeV}$, which we call the intermediate mass range.

The resulting simplified capture rate differs slightly depending on whether the matrix element depends only on t, or if it has explicit s dependence. We present the full derivations of these results in Appendix A.4 First, for $|\overline{\mathcal{M}}|^2 = at^n$, the previous expression can be simplified to

$$C \sim C_{\rm approx} = \frac{4\pi}{v_\star}\frac{\rho_\chi}{m_\chi}\mathrm{Erf}\left(\sqrt{\frac{3}{2}}\frac{v_\star}{v_d}\right)\int_0^{R_\star} r^2 dr\, n_i(r)\frac{1-B(r)}{B(r)}\langle\sigma(r)\rangle, \tag{2.61}$$

$$\langle\sigma(r)\rangle = \left\langle\int dt \frac{d\sigma}{dt}\right\rangle_s = \frac{a}{16\pi m_\chi^2}\frac{1}{n+1}\left(\frac{4(1-B(r))m_\chi^2}{B(r)(1+\mu^2)}\right)^n. \tag{2.62}$$

For s-dependent matrix elements the result is very similar, with the only difference being that the cross-section is not averaged over s, and instead s is fixed to a particular value as detailed in Appendix A.4. Writing the matrix element as $|\overline{\mathcal{M}}|^2 \propto \bar{g}(s)t^n$, for with g some function of s, we arrive at the result

$$C \sim C_{\text{approx},s} = \frac{4\pi}{v_\star}\frac{\rho_\chi}{m_\chi}\text{Erf}\left(\sqrt{\frac{3}{2}}\frac{v_\star}{v_d}\right)\int_0^{R_\star} r^2 dr\, n_i(r)\frac{1-B(r)}{B(r)}\sigma(r), \tag{2.63}$$

$$\begin{aligned}\sigma(r) = \int dt \frac{d\sigma}{dt} = &\frac{1}{16\pi\left(m_i^2 m_\chi^2 + 2m_i m_\chi/\sqrt{B(r)}\right)}\frac{\bar{g}(s_0)}{(n+1)} \\ &\times\left[\frac{4(1-B(r))m_\chi^2}{B(r)(1+\mu^2)+2\sqrt{B(r)}\mu}\right]^n,\end{aligned} \tag{2.64}$$

$$s_0 = m_i^2 + m_\chi^2 + 2\frac{E_i m_\chi}{\sqrt{B(r)}}. \tag{2.65}$$

As with the differential interaction rates, it is the t-dependence of the matrix elements that dictate the key features of the capture rate.

In Fig. 2.6, we show the capture rate as a function of the DM mass for matrix elements proportional to t^n, for $n = 0, 1, 2$ and the NS benchmark model BSk24-2. Numerical results obtained using Eq. 2.60 are shown in solid red; results using the same equation but removing the theta function that enforces Pauli blocking are depicted in light blue; and the approximation for intermediate DM masses, Eq. 2.61, in yellow. We show the geometric limit, Eq. 2.27, in blue for comparison. The capture rates were all normalised to the geometric limit at large DM mass where PB is negligible. In the same plots, we also show in brown the result obtained from using a modified version of Eq. 2.61 to include Pauli blocking. This is achieved by including the ratio between the differential the interaction rate, Γ^-, calculated with and without Pauli blocking. This comparison was done in section 2.3.1 for various values of B and $\varepsilon_{F,n}$.

From Fig. 2.6, we can see that Eq. 2.61 is indeed a good approximation to the numerical results obtained without Pauli blocking, and can be safely used for DM masses from a few GeV up to $m_\chi \sim 10^6$ GeV, where multiple scattering becomes relevant. On the other hand, for $m_\chi \lesssim 100$ MeV the brown line is no longer a good approximation to the numerical result with Pauli blocking, as it always overestimates the capture rate by nearly an order of magnitude. Therefore, to accurately account for the effects of PB for low mass DM, the complete expression for the capture rate, Eq. 2.60 must be used and evaluated numerically.

We now compare our full numerical capture rate calculation, Eq. 2.60, with that of Ref. [108], in Fig. 2.7. The capture rates calculated in Ref. [108] correctly include the stellar structure and Pauli blocking, however, they do not account for general relativistic corrections, and the authors only considered the case of a constant cross-section, $\sigma = 10^{-45}$ cm^2. Top make the comparison as fair as possible, we have

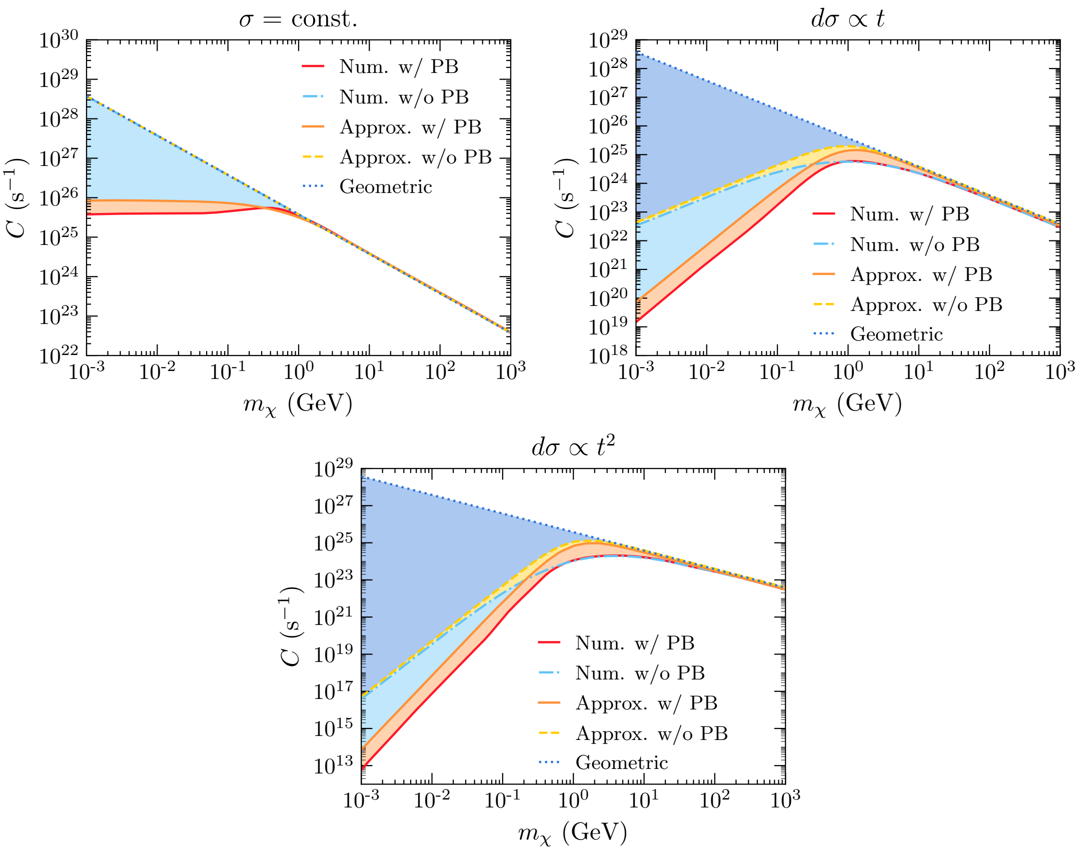

Figure 2.6: Capture rate as a function of the DM mass with cross-sections normalised to $\sigma = \sigma_{\text{ref}} \sim 1.7 \times 10^{-45}\,\text{cm}^2$, for EoS BSk24-2, calculated with and without Pauli blocking. Top left: constant cross-section. Top right: $d\sigma \propto t$, bottom: $d\sigma \propto t^2$, where t is the Mandelstam variable. All rates are normalised to the geometric limit at large DM mass.

selected NS configurations that match those of Figs. 1 and 14 of Ref. [108], namely their Model A (BSk20-1): $M_\star \simeq 1.52 M_\odot$, $R_\star \simeq 11.6\,\mathrm{km}$ and Model D (BSk21-2): $M_\star \simeq 2.11 M_\odot$ and $R_\star \simeq 12.0\,\mathrm{km}$. We denote these new benchmark models as BSk26-1 (left panel of Fig. 2.7) and BSk24-5 (right panel). Note that we were not able to use the BSk20 and BSk21 functionals, since there are no publicly available fits for the chemical potentials and particle abundances for those EoS families. However, as discussed earlier in section 1.3.2, BSk26 (BSk24) yields configurations that are almost indistinguishable from those obtained with BSk20 (BSk21) [85].

We can see in the left panel of Fig. 2.7 that in the non-Pauli suppressed region, $m_\chi \gtrsim 1\,\mathrm{GeV}$, our capture rate calculation in the optical thin limit (solid magenta) exceeds that of Ref. [108] (dot-dashed blue) by a factor of ~ 4. When Pauli blocking is active, our capture rate calculation is about one order of magnitude higher than the classical calculation. Recall that Ref. [108] accounts for neither gravitational focusing nor relativistic kinematics. We also show in dashed light blue the approximation given in Ref. [111], which accounts for Pauli blocking with a suppression factor that depends on the neutron Fermi momentum $\sim m_\chi v_{esc}/p_{F,n}$ for $m_\chi < m_n$. Though this approximation fails to reproduce the capture rate shape due to Pauli blocking in the DM mass range $[0.1\,\mathrm{GeV}, 10\,\mathrm{GeV}]$, it underestimates the capture rate by only a factor of 2 when the DM mass is below 0.1 GeV. Finally, we compare the geometric limit of Eq. 2.27 (solid orange) that incorporates GR effects [106] with the non-relativistic expression in Ref. [108] (dot-dashed brown). We observe that the former is $\sim 67\%$ greater than the latter, mostly due to the $1/B(R_\star)$ GR correction [105, 107]. Similar conclusions are obtained when comparing capture rate calculations for Model D of Ref. [108] (their Fig. 14) with our approach, as illustrated in the right panel of Fig. 2.7.

2.4.2 Large Mass Regime: Multiple Scattering

The capture rate expressions obtained in the previous section assume that the cross-section is small enough that the star is in the “optically thin” regime, and that a single scatter is sufficient to capture the DM. These assumptions break down if the DM-target cross-section is $\gtrsim \mathcal{O}(\sigma_{\rm th})$, or if the DM mass exceeds $m_\chi \sim 10^6\,\mathrm{GeV}$, respectively. In this section, we focus on addressing the latter concern as we work in the optically thin regime for the remainder of this work[4]. To that end, we now explain how to modify our previous capture rate expressions to account for multiple scattering in a degenerate media[5]

In deriving Eq. 2.59 we had assumed that the DM velocity at infinity, u_χ, can

[4]The discussion on the effect of the NS opacity in $\sigma \sim \sigma_{\rm th}$ regime can be found in Ref. [99].

[5]For a recent discussion on multiple scattering within non-relativistic stars, or with ions in WDs, see Ref. [112].

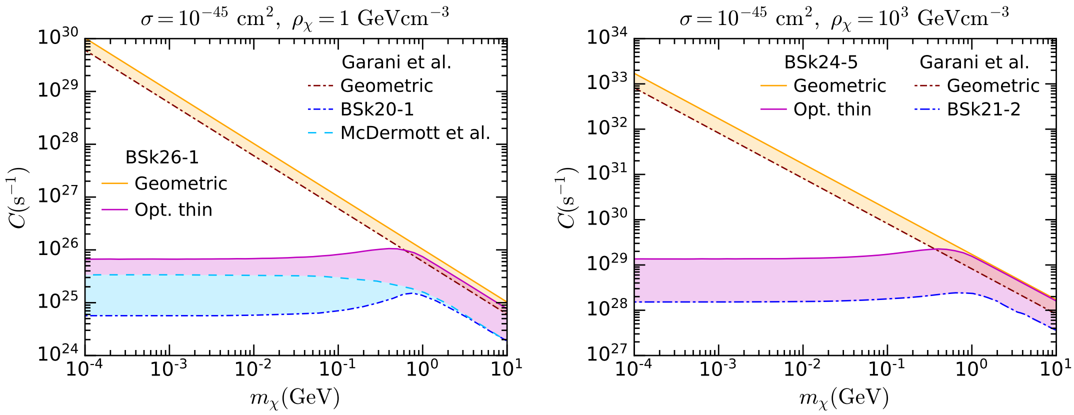

Figure 2.7: Left: Capture rate in the optically thin (magenta) and geometric (orange) limits as a function of the DM mass for constant cross-section $\sigma = 10^{-45}\,\mathrm{cm}^2$, $\rho_\chi = 1\,\mathrm{GeV\,cm}^{-3}$ and BSk26 functional for $M_\star \simeq 1.52 M_\odot$ and $R_\star \simeq 11.6\,\mathrm{km}$ denoted as BSk26-1. Capture rate calculations from Ref. [108] for a NS configuration with EoS BSk20-1 [80] equivalent to BSk26-1, are shown for comparison. Right: Same as left but for $\rho_\chi = 10^3\,\mathrm{GeV\,cm}^{-3}$ and the benchmark model BSk24-5 equivalent to BSk21-2 in Ref. [108]: $M_\star \simeq 2.11 M_\odot$ and $R_\star \simeq 12.0\,\mathrm{km}$.

be neglected, such that any interaction where the DM loses energy resulted in its capture. If we instead keep the leading order u_χ contribution to the total DM energy, the DM energy at infinity is

$$E_\chi^\infty \sim m_\chi \left(1 + \frac{1}{2} u_\chi^2\right), \tag{2.66}$$

and at a distance r from the star, it gets boosted to

$$E_\chi(r) = \frac{m_\chi}{\sqrt{B(r)}} \left(1 + \frac{1}{2} u_\chi^2\right). \tag{2.67}$$

Therefore, the amount of energy that the DM must lose to be captured is

$$E_\chi^C(r) = \frac{1}{2} u_\chi^2 \frac{m_\chi}{\sqrt{B(r)}}. \tag{2.68}$$

$$\sim 0.6\,\mathrm{GeV} \left(\frac{u_\chi}{270\,\mathrm{km\,s}^{-1}}\right)^2 \left(\frac{m_\chi}{10^6\,\mathrm{GeV}}\right) \left(\frac{0.5}{B(r)}\right)^{1/2}. \tag{2.69}$$

Hence, DM with a mass of 10^6 GeV with an initial velocity $u_\chi = 270\,\mathrm{km\,s}^{-1}$, must lose 0.6 GeV of energy for it to be captured. This is of the same order as the maximum amount of energy that can be lost in a single scatter as seen in Fig. 2.2. Given that $q_0^{\rm MAX}$ plates for $m_\chi \gg m_i$, it will be highly improbable that DM heavier than $\sim 10^6\,$GeV loses enough energy in a single scatter to be captured. Single scatter capture is still possible as the DM velocity at infinity is not a fixed value, rather it follows by some distribution function. Therefore, the heavy DM could have a velocity close to zero at infinity, significantly reducing the amount of energy it needs to lose.

To account for this effect, we assume that the DM particles have a speed $u_\chi \ll 1$ at infinity that follows a Maxwell-Boltzmann (MB) distribution, Eq. 2.18. We can then define the probability density function (PDF) of the energy lost by the DM using the differential interaction rate through

$$\xi(q_0, E_\chi, \varepsilon_{F,i}) = \frac{1}{\Gamma^-(E_\chi)}\frac{d\Gamma^-}{dq_0}(q_0, E_\chi, \varepsilon_{F,i}), \tag{2.70}$$

where $\frac{d\Gamma}{dq_0}$ is the DM differential interaction rate, calculated in Appendix 2.3. The function ξ is defined for any $q_0 \geq 0$, however, kinematics dicatates that the function is non-zero only for $q_0 \leq q_0^{\rm MAX}$. Additionally, note that ξ depends on $B(r)$ through the ratio E_χ/m_χ, and for brevity we will simply write $\xi(q_0)$.

We can define the probability of losing at least an amount of energy $q_0 = \delta q_0$ in a single collision as

$$P_1(\delta q_0) = \int_{\delta q_0}^{\infty} dx \xi(x). \tag{2.71}$$

The probability of losing at least the same amount of energy after 2 collisions will then be

$$P_2(\delta q_0) = \int_{\delta q_0}^{\infty} dy \int_0^{\infty} dx\, \xi(x)\xi(y-x) \tag{2.72}$$

$$= P_1(\delta q_0) + \int_{\delta q_0}^{\infty} dy \int_0^{y} dx\, \xi(x)\xi(y-x) \tag{2.73}$$

$$= P_1(\delta q_0) + \int_0^{\delta q_0} dz\, P_1(\delta q_0 - z)\xi(z). \tag{2.74}$$

From this, we obtain the following recursive relation for the probabilities, P_N, of losing at least $q_0 = \delta q_0$ in N scatters,

$$P_{N+1}(\delta q_0) = P_N(\delta q_0) + \int_0^{\delta q_0} dz P_N(\delta q_0 - z)\xi(z). \tag{2.75}$$

In Fig. 2.8 we show how the probability functions $P_1, ..., P_5$ changes based on the t dependence of the differential cross-section. We show results for σ =const. (top

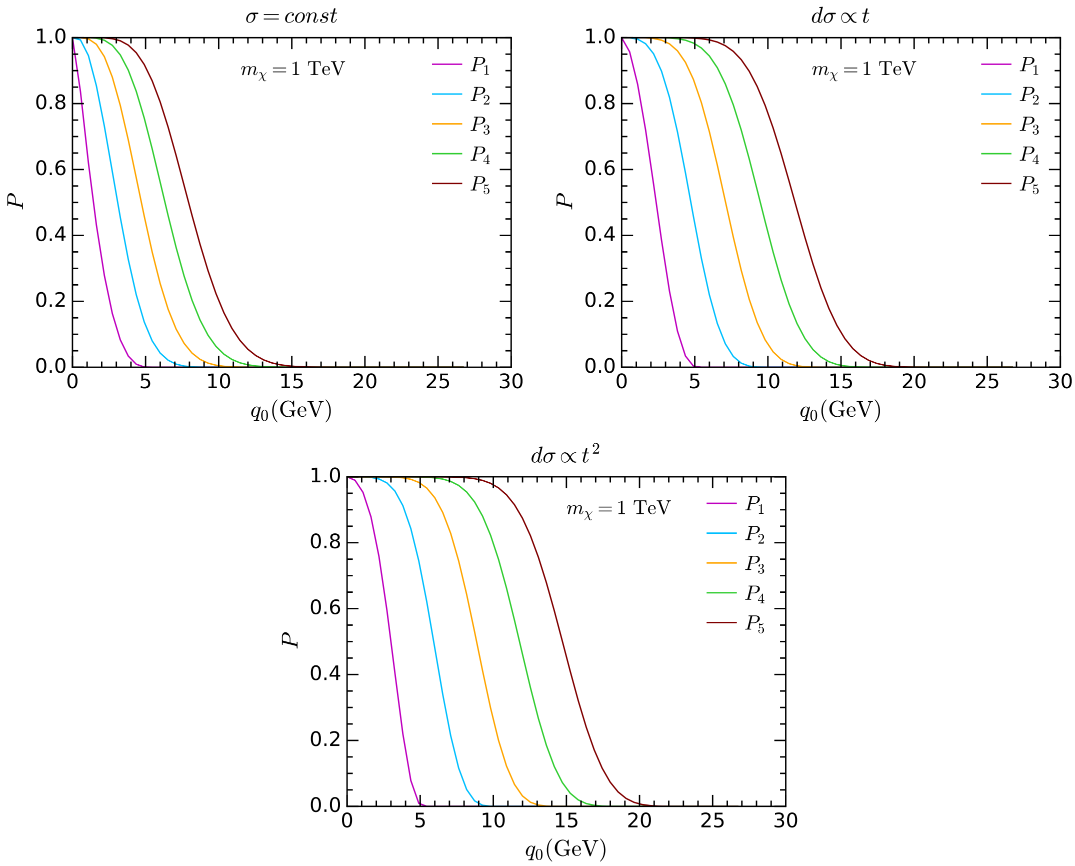

Figure 2.8: Probabilities to lose at least an amount of energy δq_0 after $1, ..., 5$ scatterings, $P_1, ..., P_5$, as a function of the energy loss q_0, assuming $B = 0.5$ and $\varepsilon_{F,n} = 400\,\text{MeV}$. Results are shown for different dependence on the cross-section on the Mandelstam variable t: constant DM-neutron cross-section (top left), $d\sigma \propto t$ (top right) and $d\sigma \propto t^2$ (bottom).

left), $d\sigma \propto t$ (top right) and $d\sigma \propto t^2$ (bottom), for fixed values of $B = 0.5$, $\varepsilon_{F,n} = 400\,\text{MeV}$.

To connect this back to the capture probability, we define the probability for a DM particle to be captured after exactly N interactions, c_N, to be $P_N(E_\chi^C) - P_{N-1}(E_\chi^C)$ averaged over the MB distribution of the initial velocity,

$$c_N(r) = \frac{1}{\int_0^\infty \frac{f_{\rm MB}(u_\chi)}{u_\chi} du_\chi} \int_0^\infty \frac{f_{\rm MB}(u_\chi)}{u_\chi} du_\chi \left[P_N\left(\frac{1}{2}\frac{m_\chi u_\chi^2}{\sqrt{B(r)}}\right) - P_{N-1}\left(\frac{1}{2}\frac{m_\chi u_\chi^2}{\sqrt{B(r)}}\right)\right], \tag{2.76}$$

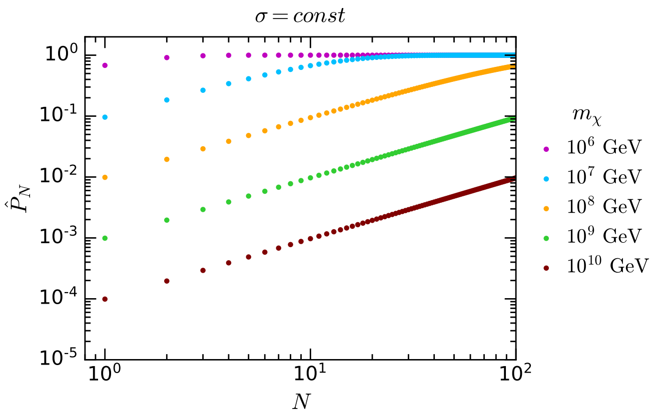

Figure 2.9: Cumulative probability $\hat{P}_N$ for $B = 0.5$, $\varepsilon_{F,n} = 400\,\mathrm{MeV}$ and for $\sigma =$ const. as a function of the number of scatterings N for several DM masses.

where c_N depends on r through the dependence of P_N on $B(r)$ and $\varepsilon_{F,n}(r)$. Note that although our results will assume a Maxwell-Boltzmann velocity distribution, it is straightforward to generalise the results to any other DM velocity distribution. The cumulative probability $\hat{P}_N$ that a DM particle is captured after N interactions with a total energy loss $\delta q_0 = E_\chi^C$ is then

$$\hat{P}_N(r) = \sum_{i=1}^{N} c_i = \frac{1}{\int_0^\infty \frac{f_{\rm MB}(u_\chi)}{u_\chi} du_\chi} \int_0^\infty \frac{f_{\rm MB}(u_\chi)}{u_\chi} du_\chi P_N\left(\frac{1}{2}\frac{m_\chi}{\sqrt{B(r)}}u_\chi^2\right). \tag{2.77}$$

The resulting cumulative probability is shown as a function of the number of scatterings N in Fig. 2.9, for constant cross-section and several DM masses.

The cumulative probability $\hat{P}_N$ for the above values of $B, \varepsilon_{F,n}$ is well approximated by the function[6]

$$\hat{P}_N \sim 1 - e^{-\frac{N m_i^*}{m_\chi}}. \tag{2.78}$$

In particular, the probability that the DM is captured in a single scatter is

$$c_1 = \hat{P}_1 \sim 1 - e^{-\frac{m_i^*}{m_\chi}}. \tag{2.79}$$

From this, we see that c_1 will begin to significantly fall below unity for $m_\chi \gtrsim m_i^*$, and hence multiple scattering will only significantly reduce the capture rate for DM masses above m_i^*.

[6]Further discussion of the multi-scattering regime, and justification of this fitting function, can be found in Appendix C of Ref. [99].

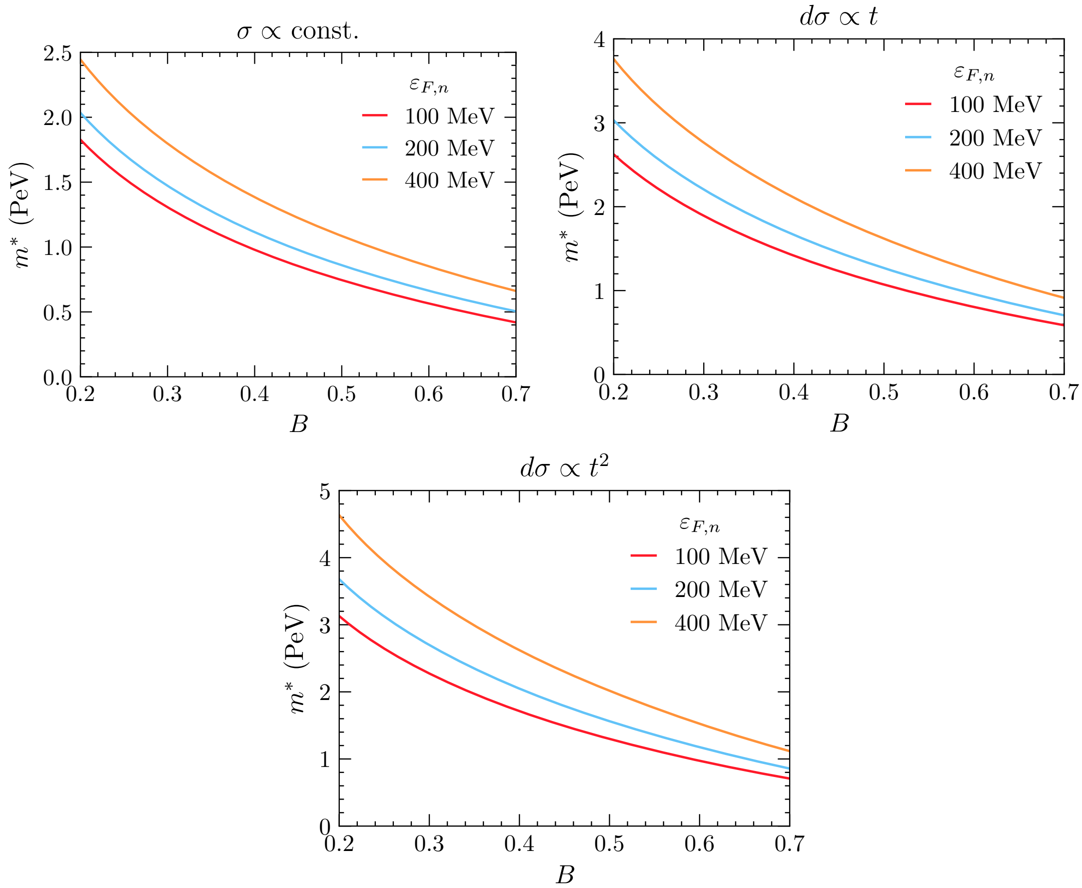

Figure 2.10: Value of m_n^* as a function of B for different values of $\varepsilon_{F,n}$, $\sigma = const.$ (top left), $d\sigma \propto t$ (top right) and $d\sigma \propto t^2$ (bottom).

To give an idea for how large the value of m_i^* will be, for neutron targets and the values $B = 0.5$ and $\varepsilon_{F,n} = 400$ MeV, we find

$$m^* = 1.08 \times 10^6\,\text{GeV}, \quad |\overline{\mathcal{M}}|^2 \propto t^0, \tag{2.80}$$
$$m^* = 1.62 \times 10^6\,\text{GeV}, \quad |\overline{\mathcal{M}}|^2 \propto t^1, \tag{2.81}$$
$$m^* = 2.01 \times 10^6\,\text{GeV}, \quad |\overline{\mathcal{M}}|^2 \propto t^2. \tag{2.82}$$

We illustrate how m_n^* varies with B and $\varepsilon_{F,n}$ in Fig. 2.10.

When the cross-section is small, $\sigma \ll \sigma_{\rm th}$, such that we are in the optically thin regime, if the DM does not get captured in its initial scatter, then it will leave the star without interacting again. To account for this, the factor of c_1 should be included in the capture rate calculation, Eq. 2.26. However, as we have jsut seen, $c_1 \ll 1$ only for $m_\chi \gtrsim m_i^*$, which will always be significantly larger than the target mass and chemical potential. Therefore, multiple scattering is only important in the regime where PB is negligible, and so a suitable approximation for the capture rate in this regime is

$$C^*_{\rm approx} = \frac{4\pi}{v_\star}\frac{\rho_\chi}{m_\chi}{\rm Erf}\left(\sqrt{\frac{3}{2}}\frac{v_\star}{v_d}\right)\int r^2 dr \frac{\sqrt{1-B(r)}}{B(r)}\Omega^-(r)c_1(r), \tag{2.83}$$

with $\Omega^-(r)$ calculated as outlined in sections 2.4.1

2.5 Results

In this section, we present our results for the capture rate of fermionic DM scattering from neutrons within a NS in the zero temperature approximation. We calculate the capture rate only for scalar/pseudoscalar-scalar/pseudoscalar interactions between DM and neutrons, i.e. effective operators D1-D4 in Table **??**, whose differential cross-sections depend only on the Mandelstam variable t and not on s. We use realistic radial profiles for the neutron number density, chemical potential, and relativistic corrections encoded in $B(r)$ as explained in section 1.3.2, obtained from the BSk24 EoS for the configurations in Table 1.2.

To estimate the NS EoS impact on the DM capture rate computation, we numerically calculate C using the exact expression in the optically thin limit, Eq. 2.60, that properly accounts for gravitational focusing and Pauli blocking. In the optically thin regime that we are working in, the capture rate is proportional to the differential DM-neutron cross-section. Fig. 2.11 shows how this rate varies with the NS EoS for operators D1-D4 and the EoS configurations given in Table 1.2, and in turn with the NS mass and radius. The cross-section is normalised such that the capture rate in the intermediate mass range, which is unaffected by PB and multiple scattering, is equal to the geometric limit. It is worth remarking that cross-sections larger than the threshold cross-section should not be used in the optically thin limit, as this would result in capture rates larger than the geometric limit. To account for such large cross-sections, the optical depth of the NS must be accounted for as prescribed in Ref. [99]. Depending on the operator considered, going from the lightest to the heaviest NS can change the capture rate by a minimum of one order of magnitude, such as in the case of operators D1, D2 and D3 (at low DM mass), and up to 2 orders of magnitude, as in the case of operators D2 for large DM mass, and D4 in general.

At large DM mass, all operators show the same scaling with the DM mass. At $m_\chi \lesssim 1\,{\rm GeV}$, a different picture arises as Pauli blocking leads to different suppressions of the capture rate for the different operators. However, we observe that the four operators give very similar results to those of Fig. 2.6, where we analysed the dependence of the capture rate on the momentum transfer t. We note that operator

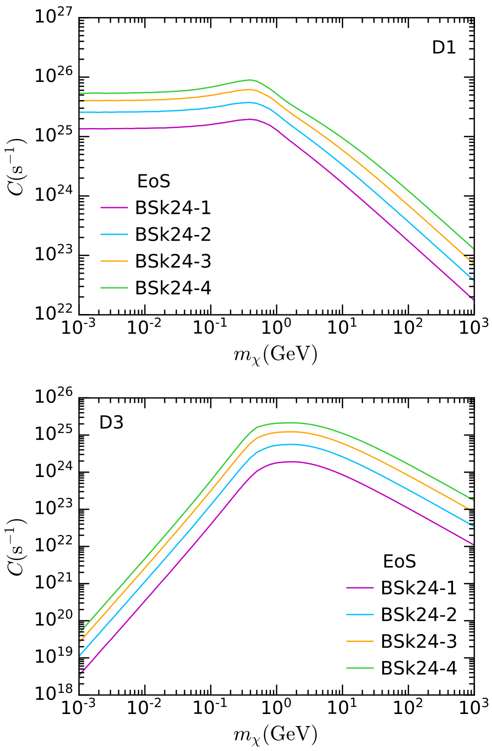

Figure 2.11: Capture rate in the optically thin limit as a function of the DM mass for $\sigma = \sigma_{\mathrm{ref}} \sim 1.7 \times 10^{-45}\,\mathrm{cm}^2$ and the configurations of the EoS BSk24 given in Table 1.2. Rate calculated using the 4-dimensional integral in Eq. 2.60, that includes Pauli blocking but neglects the NS opacity and multiple scattering. Results are shown for the EFT operators D1 (top left), D2 (top right), D3 (bottom left) and D4 (bottom right) in Table **??**.

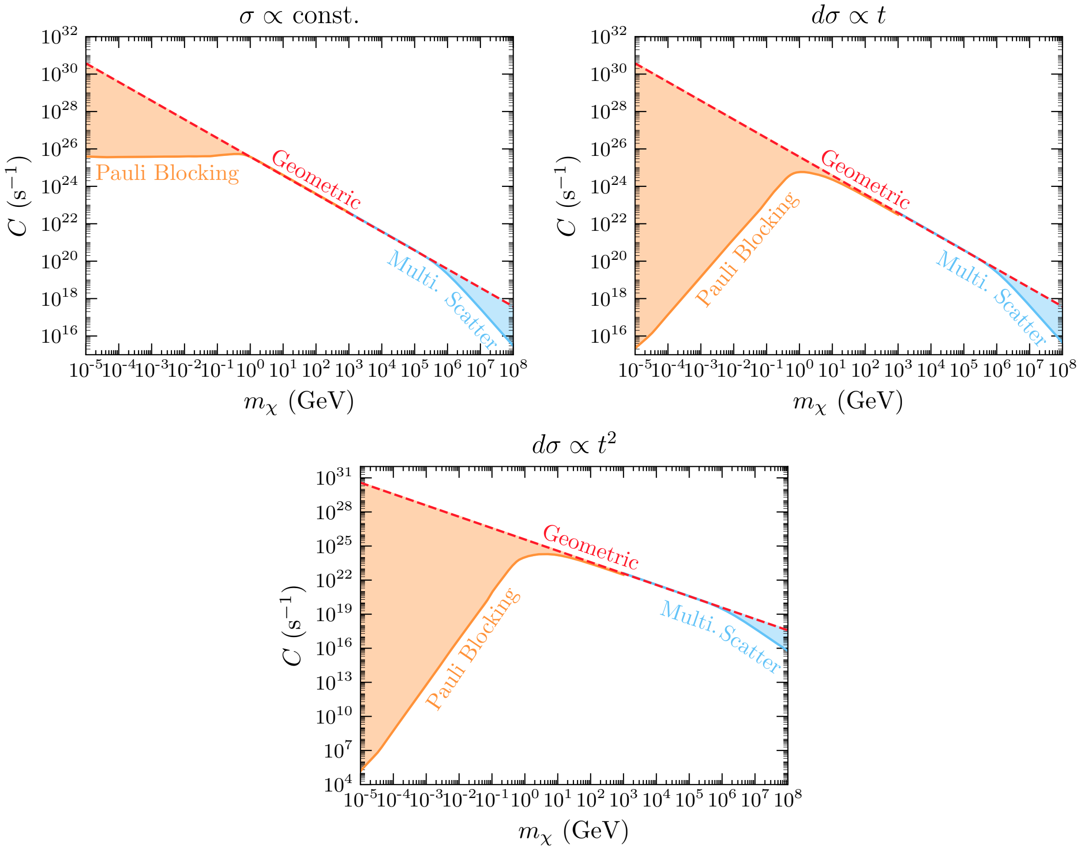

Figure 2.12: Capture rate for constant cross-section (top left), $d\sigma \propto t$ (top right) and $d\sigma \propto t^2$ (bottom), for $\sigma = \sigma_{\rm ref} \sim 1.7 \times 10^{-45}\,\mathrm{cm}^2$ and NS EoS configuration BSk24-2. These plots extent the mass range of those in Fig. 2.6 to large DM masses.

D1, which contains in its squared matrix element a term independent of t, gives a result that is very similar to that of $\sigma = $ const. Operators D2 and D3, for which $|\overline{\mathcal{M}}|^2$ does not include terms independent of t, but rather terms proportional to t and t^2, yield very similar results to that of $d\sigma \propto t$. Overall, we conclude that the lowest power of the transferred momentum determines the mass scaling of the capture rate at low DM mass. This result holds true for matrix elements that depend also on s.

In Fig. 2.12, we show the capture rate for a broad DM mass range, spanning 13 orders of magnitude from $m_\chi = 10\,\mathrm{keV}$ to $m_\chi = 10^8\,\mathrm{GeV}$, including all three of the mass regimes we have discussed in the previous sections, for $d\sigma \propto const.$ (first row), t^1 (second row) and t^2 (third row). The orange line indicates the capture rate calculated in the optically thin limit using the 4-dimensional integration in Eq. 2.59 that accounts for Pauli blocking. At large DM masses, Pauli suppression plays no role and the capture rate approaches the geometric limit (dashed red line). We also show in Fig. 2.12 the effect of the inclusion of multiple scattering in the light blue line, which becomes relevant at $m_\chi \sim 10^6\,\mathrm{GeV}$. At $m_\chi \sim 10^5\,\mathrm{GeV}$ that line matches the geometric limit as expected from the chosen value of the cross-section $\sigma = \sigma_{\rm ref}$. At larger DM masses, $m_\chi \gtrsim 10^6\,\mathrm{GeV}$, multiple scatterings are required for the DM to be captured, hence an additional suppression factor of $1/m_\chi$ arises, as given in Eq. 2.83. Therefore, the capture rate becomes increasingly smaller than C_{geom} (light blue shaded area).

Comparing the plots for different t^n dependence, we can see that increasing the power of n has a small effect on the mass scale where the various suppressions become relevant. For example, comparing the light blue lines between the three figures, we see that the change of slope from the onset of multiple scattering moves slightly further to the right for larger n. This is a consequence of the fact that larger powers of n result in larger energy transfer (see, for example, Fig. A.2), leading to a larger capture probability c_1 and hence a larger m_i^*. However, the qualitative behaviour is the same for all choices of $d\sigma$: the suppression of the capture rate is primarily due to Pauli blocking at low mass and multiple scattering effects (i.e. a low capture probability) at large masses.

2.6 Summary

In this chapter, we have improved and extended the existing framework used to calculate the DM capture rate in the Sun to be compatible with compact objects, relaxing the simplifying assumptions that have previously been made. Specifically, we have derived exact expressions for the capture rate that correctly incorporate relativistic kinematics, gravitational focusing, Pauli blocking, and multiple-scattering effects. We also properly incorporate the internal structure of the star, consistently calculating the radial profiles of the EoS-dependent parameters and the general relativistic corrections, by solving the Tolman-Oppenheimer-Volkoff equations.

This new formalism was applied to neutron stars to highlight the features of the formalism mentioned above. Neutron stars (and compact objects in general) are composed of strongly degenerate matter, resulting in significant Pauli blocking of scattering interactions when the dark matter is light, $m_\chi \lesssim m_i$, suppressing the capture rate by several orders of magnitude. By including the radial dependence of the chemical potential in our calculations, we correctly account for Pauli suppression at any point in the star. However, note that the chemical potential is dependent on the EoS assumption.

For very large DM masses, $m_\chi \gtrsim 10^6\,\mathrm{GeV}$, the energy lost in a single collision will be insufficient for it to be captured. Hence, the DM must scatter multiple times within an orbit to be captured, or else it simply leaves the star. To correctly compute the DM capture probability due to multiple scattering, we have derived, for the first time, an exact equation for the DM interaction rate in degenerate matter, and used that result to compute the differential capture rate as a function of the DM energy loss. This enables us to compute the cumulative probability that a DM particle is captured after multiple interactions, by averaging over the initial DM velocity distribution.

Although we have framed our results in terms of the scattering of DM from neutron targets in neutron star, it is straightforward to obtain the capture rate for DM scattering from any other degenerate species in compact objects. In the next chapter, we apply this formalism to DM scattering off the leptonic compoennts of NSs, as well as the degenerate electrons within WDs.

3

Dark Matter Capture from Leptonic Species in Compact Objects

This chapter is based on the results of Ref. [100] and on the electron capture resluts in Ref. [113]. We apply the formalism for capture in compact objects to leptonic targets in neutron stars and white dwarfs. In NSs, we calculate the projected sensitivities for the threshold DM-electron/muon cross-sections that could be probed in future observations. We then move to capture from the electrons in WDs, where we analyse the existing observations of the WDs in the globular cluster M4. Limits are placed on the DM-electron cross-section by requiring that the DM does not heat up the WDs above their observed temperatures through scattering and annihilation.

3.1 Capture from Leptons in Neutron Stars

Despite NSs being composed primarily of baryons (neutrons and protons in particular), they can still contain a substantial number of leptonic particles, namely electrons and, to a smaller extent, muons. For example, 1.5 $M_\odot$ NS can contain $\sim 5 \times 10^42$ leptons, corresponding to a threshold cross-section $\sigma_{\ell\chi}^{\rm th} \sim 10^{-43}\,{\rm cm}^2$, far below current direct detection bounds. This warrents a detailed study into the DM-lepton parameter space that could be explored with upcoming NSs observations.

To that end, we will consider the BSk24 EoS, with the benchmark configurations listed in Table. 1.2. In Fig. 3.1 we plot the corresponding lepton profiles. As mentioned above, electrons are present in the core and the crust while muons appear at baryon number densities $n_b \simeq 0.12\,{\rm fm}^{-3}$. The kink observed in the electron

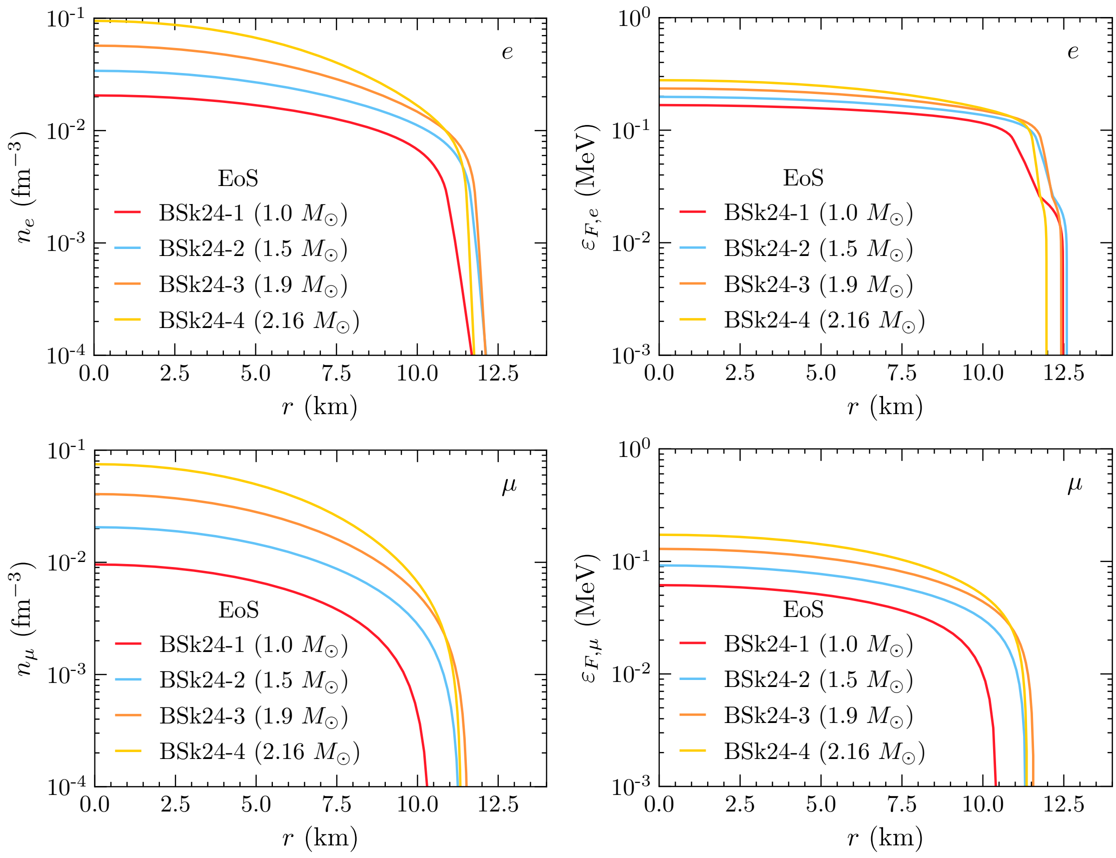

Figure 3.1: Number density profile (left) and chemical potential (right) for electrons (top) and muons (bottom) and NS configurations of the BSk24 functional in Table 1.2.

chemical potential marks out the transition from the core to the inner crust. The aforementioned radial profiles will be used in the following section to calculate the capture rate.

3.1.1 Capture Rate

In this section, we present results for the capture rate $C\Lambda^4$ for each of the EFT operators in Table **??**, calculated in the optically thin limit using Eq. 2.60 for $m_\chi \lesssim m_\ell^*$ and Eq. 2.83 for $m_\chi \gtrsim m_\ell^*$[1]. Typical values of $m_\ell^\star$ and $\sigma_{\ell\chi}^{\rm th}$ are shown in Table. 3.1 for electron and muon targets. Note that in m_ℓ^* will depend on the

[1] To numerically solve these equations we use the `CUBA` libraries [114, 115] linked to `Mathematica` [116].

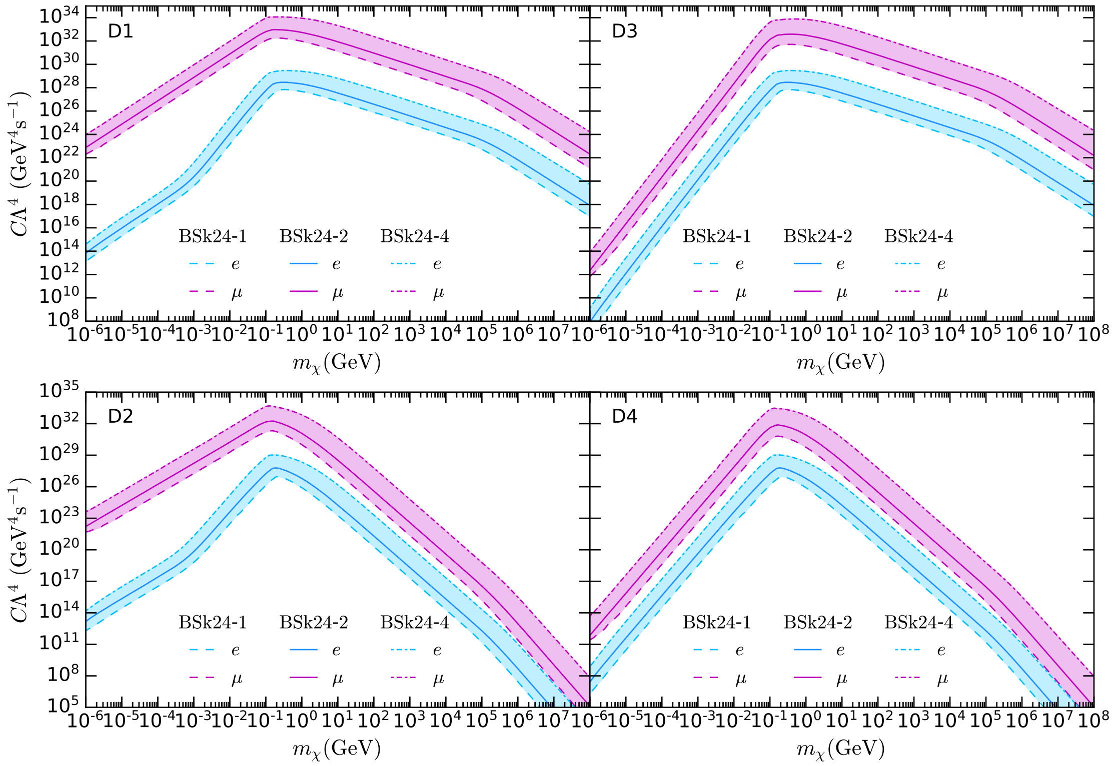

Figure 3.2: Capture rate in the optically thin limit for operators D1-D4 as a function of the DM mass m_χ for electrons (light blue) and muons (magenta) in the NS benchmark models BSk24-1 (dashed), BSk24-2 (solid) and BSk24-4 (dot-dashed). The shaded regions denote the change in the capture rate with the NS configuration for the same EoS family BSk24. All capture rates scale as Λ^{-4}. We require Λ to be sufficiently large that the capture rates are smaller than the geometric limit, $C_{\rm geom}$.

values of $B(r)$ and $\varepsilon_{F,\ell}(r)$, as well as the type of interaction considered.

Figs. 3.2 and 3.3 show the results for electron (light blue) and muon (magenta) targets, considering three NS benchmark models: BSk24-1 (dashed, $1M_\odot$), BSk24-2 (solid, $1.5M_\odot$) and BSk24-4 (dot-dashed, $2.16M_\odot$). In addition, we assume a nearby NS, located in the Solar neighbourhood, and thus take $\rho_\chi = 0.4\,\mathrm{GeV\,cm^{-3}}$, $v_\star = 230\,\mathrm{km\,s^{-1}}$ and $v_d = 270\,\mathrm{km\,s^{-1}}$.

In these figures, we observe that the capture rate is suppressed due to Pauli blocking when $m_\chi \lesssim m_\ell$. The change of slope at $m_\chi \sim m_\ell^* \sim 10^5\,\mathrm{GeV}$, observed for both targets, is due to multiple scattering. For the operators D5-10 (Fig. 3.3), whose matrix elements depend explicitly on s, the slope of the capture rate in the three mass regimes are all very similar to one another, while for D1-D4 (Fig. 3.2), the shape of C is controlled by the power of t that dominates the interaction, which

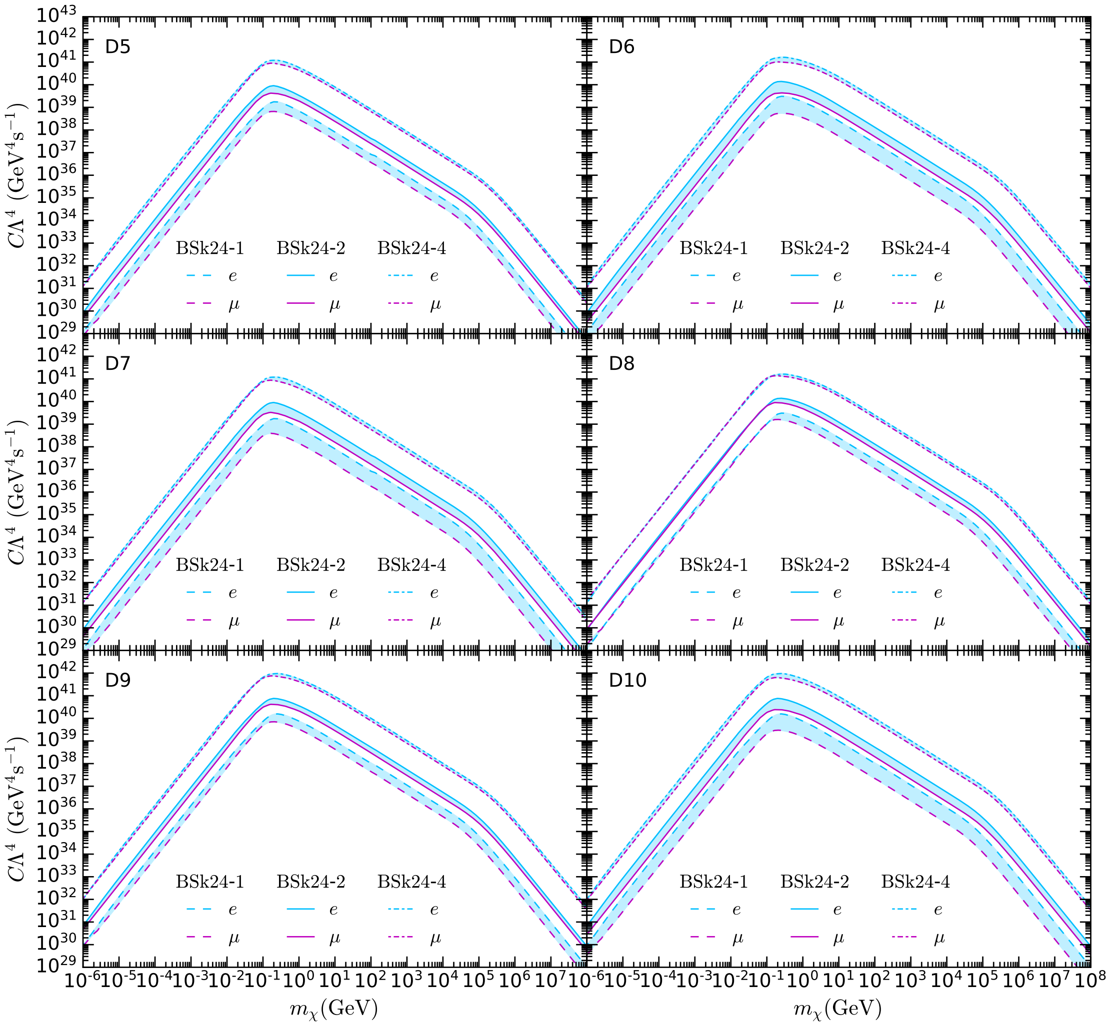

Figure 3.3: Capture rate in the optically thin limit for operators D5-D10 as a function of the DM mass m_χ for electrons (light blue) and muons (magenta) in the NS benchmark models BSk24-1 (dashed), BSk24-2 (solid) and BSk24-4 (dot-dashed). All capture rates scale as Λ^{-4}. The shaded regions depict the difference between capture by electrons and muons for the above mentioned NS models.

Target	μ	e
m_ℓ^* (GeV)	$[0.3, 3] \times 10^5$	$[0.05, 1.7] \times 10^5$
$\sigma_{\ell\chi}^{\rm th}$ (cm^2)	8×10^{-44}	3×10^{-44}

Table 3.1: Typical values of m_ℓ^* and $\sigma_{\ell\chi}^{\rm th}$ for lepton targets. The exact value of $\sigma_{\ell\chi}^{\rm th}$ depends on the DM mass, and the operator. We show here the simplest case of constant matrix element; other operators give similar results. The threshold cross section is approximately constant in the range $1\,\mathrm{GeV} \lesssim m_\chi \lesssim m_\ell^*$, and takes larger values outside that range with a $1/m_\chi$ or m_χ scaling for small and large masses, respectively.

in general is the lowest power [99].

The exceptions to this are the capture rates for operators D1 and D2 with electron targets, which show a distinctive feature in the region $m_e \lesssim m_\chi \lesssim 100\,\mathrm{MeV}$ that does not occur for the other operators. The capture rate for D1 and D2 is more suppressed in that particular region, similarly to D3 and D4, respectively. This is due to the form of the corresponding matrix elements together with the smallness of the electron mass. Namely, D1 and D2 are the only two operators that contain a factor $(t - 4m_\ell^2)$ in their scattering amplitudes, for electrons this means that the lowest power of t in $|\overline{\mathcal{M}}|^2$ is multiplied by m_e^2, i.e. these terms are suppressed in the $m_e \lesssim m_\chi \lesssim 100\,\mathrm{MeV}$ range. Consequently, the capture rate in that DM mass region is dominated by the unsuppressed t-terms in $|\overline{\mathcal{M}}|^2$, these being t for D1 (as for D3) and t^2 for D2 (see Table **??**), while below m_e this additional suppression disappears and the capture rate follows the lowest power of t as was originally expected.

From Fig. 3.2, we note that for the same cutoff scale Λ, the muon contribution to the total capture rate for operators D1-D4 surpasses that of the electron by approximately 4 orders of magnitude for most of the DM mass range, and by about 8 orders of magnitude at very low mass for operators D1-D2. This is due to the large hierarchy between DM couplings to electrons and muons, which is of order $(\frac{m_\mu}{m_e})^2$. For operators D5-D10, electrons and muons will have the same strength couplings to DM (see Table **??**). However, despite similar couplings and a lower abundance, muons are still able to capture DM at a rate comparable to electrons (see light blue regions in Fig. 3.3), thanks to their larger mass and lower chemical potential (see Fig. 3.1, right panels). This means that their interactions with DM are less Pauli suppressed, leading to a larger interaction rate. The small difference between the rates at which electron and muon are able to capture DM particles reduces for heavier NS configurations, e.g. from a factor ~ 5 (BSk24-1) to ~ 1.5 (BSk24-4) for D6 and D10; see the light blue shaded regions in Fig. 3.3. This is due to the muon abundance increasing in heavier NSs.

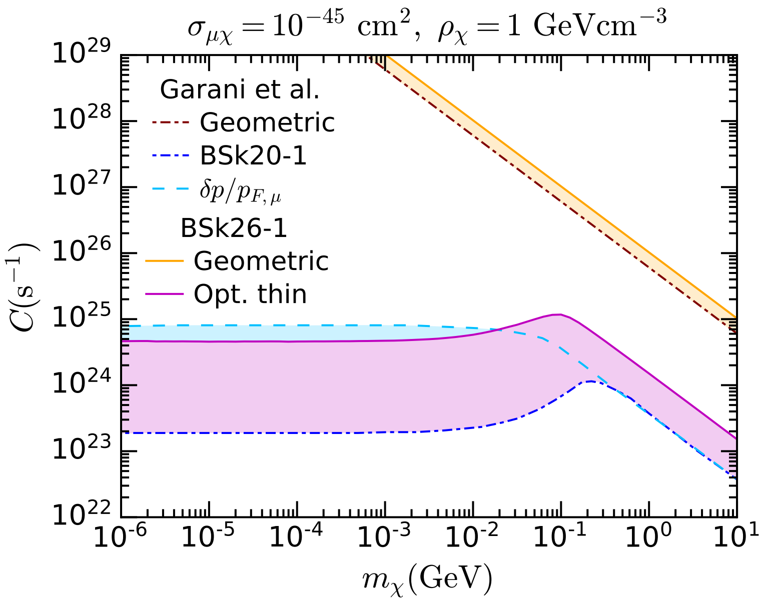

Figure 3.4: Capture rate in the optically thin limit for muon targets (magenta) and geometric (orange) limit as a function of the DM mass for constant cross-section $\sigma_{\mu\chi} = 10^{-45}\,\text{cm}^2$, $\rho_\chi = 1\,\text{GeV}\,\text{cm}^{-3}$ and BSk26 functional for $M_\star \simeq 1.52 M_\odot$ and $R_\star \simeq 11.6\,\text{km}$ denoted as BSk26-1. Capture rate calculations from Ref. [108] for a NS configuration with EoS BSk20-1 [80] equivalent to BSk26-1, are shown for comparison.

It is also worth noting that different EoS assumptions can lead to variations in the capture rate for electron targets of at least two orders of magnitude in the Pauli suppressed region and $\sim$ 2.5 orders of magnitude in the large DM mass regime (compare dashed with dot-dashed light blue lines). For muons, the effect is even larger, with capture rate variations from $\sim \mathcal{O}(5 \times 10^2)$ for low DM mass to $\sim \mathcal{O}(2 \times 10^3)$ for heavy DM, when comparing the lightest and most massive NS configurations of the BSk24 family. For the operators D2 and D4, these variations are even more pronounced for both electrons and muons and can reach $\sim \mathcal{O}(5 \times 10^3)$ and $\sim \mathcal{O}(5 \times 10^4)$, respectively for very large DM masses.

The DM capture rate for muon targets was calculated in Ref. [108], for constant cross-section and light DM, $m_\chi \leq 10\,\text{GeV}$. That calculation accounts for the NS internal structure and Pauli blocking, but neglects general relativity (GR) corrections and assumes that muons are non-relativistic. As outlined in section 2.4.1, to compare our capture rate calculation with that of Ref. [108] we select a NS model that matches that of Fig. 12 of Ref. [108], namely Model A (BSk20-1): $M_\star \simeq 1.52 M_\odot$, $R_\star \simeq 11.6\,\text{km}$. This new benchmark model is denoted as BSk26-1.

In Fig. 3.4, we compare both capture rate calculations for $\sigma_{\mu\chi} = 10^{-45}\,\text{cm}^2$ and the same assumptions about ρ_χ, $v_\star$ and v_d as in Ref. [108]. Comparing the geometric limit, Eq. 2.27 (solid orange), which properly accounts for gravitational focusing in NSs, with the non-relativistic computation in Ref. [108] (dot-dashed brown), we observe a $\sim 67\%$ enhancement, due to the $1/B(R_\star)$ factor that encodes GR corrections [105, 107]. In the region not affected by Pauli blocking, $m_\chi \gtrsim m_\mu$, our calculation in the optical thin limit (solid magenta) exceeds that of Ref. [108] (dot-dashed blue) by a factor of ~ 4, which increases as we move to the Pauli suppressed region where our computation is more than one order of magnitude higher. Unlike Ref. [108], our formalism incorporates GR corrections and made use of relativistic kinematics. We also show in dashed light blue, an estimation of the capture rate using the approximation $\delta p/p_{F,\mu} \sim m_\chi v_{esc}/p_{F,\mu}$ for $m_\chi < m_\mu$ [117], where $p_{F,\mu}$ is the muon Fermi momentum and v_{esc} is the escape velocity. This approximation overestimates the capture rate by a factor of approximately 2 in the Pauli blocked region below 10 MeV and underestimates it in the region of larger DM masses.

3.1.2 Finite Temperature Effects and Evaporation

In section 3.1.1, we have restricted our computation of the capture rates to the DM mass range $m_\chi \in [1\,\text{keV}, 10^8\,\text{GeV}]$. While the upper limit on this mass range is somewhat arbitrary, primarily limited by the increasing numerical tax of calculating Eq. 2.83, the lower bound comes from working in the zero-temperature approximation, $T_\star \to 0$. This approximation is valid for DM masses $m_\chi \gg T_\star$, which for a $10^3\,\text{K}$ star requires $m_\chi \gg 90$ meV.

For DM masses $m_\chi \lesssim \mathcal{O}(10)T_\star$, thermal effects begin to play an important role in the capture rate, significantly boosting the rate in this low mass range [108]. Consequently, the complete Fermi-Dirac distributions should be used in Eqs. 2.50 and 2.39. To illustrate the effect of the NS temperature, we show in Fig. 3.5 the ratio of the capture rate in a NS with $T_\star = 10^5\,\text{K} \simeq 8.6\,\text{eV}$ to the corresponding capture rate in the $T_\star \to 0$ limit, assuming scattering on electrons, the targets for which this effect is most relevant.

From this figure, we immediately notice that the ratio starts to depart from 1 at $m_\chi \sim 100\,\text{eV} \sim 10T_\star$ for all operators. Operators whose matrix element depends on higher powers of the exchanged momentum t feature a larger increment in the capture rate due to finite temperature. In fact, the operator D4 ($|\overline{M}|^2 \propto t^2$) receives the largest correction, followed by D2-D3 (whose $|\overline{M}|^2$ is a linear combination of t^1, t^2), then D1 ($|\overline{M}|^2$ is a linear combination of t^0, t^1, t^2) and finally by D5-D10 (whose $|\overline{M}|^2$ include all powers of the kind $t^n s^m$).

In the very light DM regime, there is another that needs to be accounted for: evaporation. This occurs when the dark matter up-scatters to a state where the final DM kinetic energy is larger than the energy required to escape the star, and hence

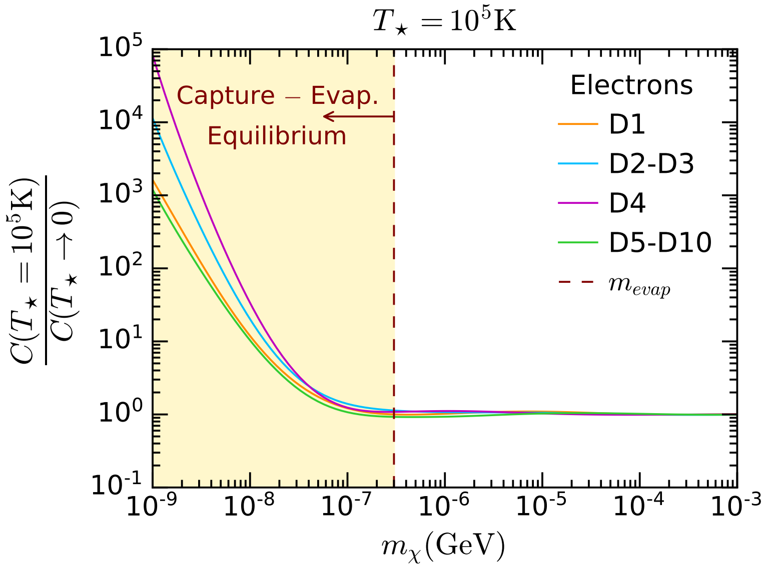

Figure 3.5: Finite temperature effects on the capture rate for electron targets, assuming the NS model BSk24-2. The DM mass range where capture and evaporation are expected to be in equilibrium is shaded in yellow. The dashed brown line corresponds to the evaporation mass.

DM particles are expelled. Thus, as opposed to capture, evaporation drains energy from the star. To estimate the evaporation rate, we convolve the DM distribution within the star, with the interaction rate for up-scattering, $\Gamma^-_{\rm up}(E_\chi, T_\star)$, retaining the temperature dependence.

Assuming the DM distribution to be isothermal with temperature $T_\chi = T_\star$, we have

$$n_\chi^{\rm iso}(r, E_\chi) = \frac{n_c}{1 + e^{\frac{E_\chi - m_\chi\left(\frac{1}{\sqrt{B(r)}}-1\right)}{T_\star}}} \tag{3.1}$$

$$\simeq \frac{\exp\left[-\frac{E_\chi - m_\chi\left(\frac{1}{\sqrt{B(r)}}-1\right)}{T_\star}\right]}{4\pi\int_0^{R_\star} dr r^2 \int_0^{m_\chi\left(\frac{1}{\sqrt{B(r)}}-1\right)} dE_\chi \exp\left[-\frac{E_\chi - m_\chi\left(\frac{1}{\sqrt{B(r)}}-1\right)}{T_\star}\right]}, \tag{3.2}$$

where n_c is a normalisation constant such that the total number of DM particles is $N_\chi = \int d^3r \int dE_\chi\, n_\chi^{\rm iso}(E_\chi, r)$. The interaction rate for up-scattering, $\Gamma^-_{\rm up}(E_\chi, T_\star)$

can be related to the down-scattering rate through

$$\frac{d\Gamma^-_{\rm up}}{dq_0}\left(E_\chi, q_0, T_\star\right) = -\frac{e^{q_0/T_\star}}{1-e^{q_0/T_\star}}\frac{d\Gamma^-}{dq_0}\left(E_\chi, q_0\right), \quad q_0 < 0, \tag{3.3}$$

where $\frac{d\Gamma^-}{dq_0}$ is the differential interaction rate in the $T_\star \to 0$ approximation derived in Appendix A.2.1, with the full derivation of Eq. 3.3 in Appendix A.2.2.

The evaporation rate then reads

$$E \simeq 4\pi \int_0^{R_\star} dr r^2 \int_0^{m_\chi\left(\frac{1}{\sqrt{B(r)}}-1\right)} dE_\chi n_\chi^{\rm iso}(r, E_\chi) \int_{-\infty}^{-q_0^{\rm min}} dq_0 \frac{d\Gamma^-_{\rm up}}{dq_0}\left(q_0, T_\star\right), \tag{3.4}$$

$$q_0^{\rm min} = m_\chi\left(\frac{1}{\sqrt{B(r)}}-1\right) - E_\chi, \tag{3.5}$$

where $q_0^{\rm min}$ is the minimum energy the DM needs to gain to be ejected from the star. When the DM distribution is concentrated very close to the centre of the star, this expression can be approximated by

$$E \sim \frac{m_\chi m_\ell^2 \sigma_{\ell\chi}}{4\pi^2}\left(\frac{1}{\sqrt{B(0)}}-1\right)^2 \exp\left[-\frac{m_\chi}{T_\star}\left(\frac{1}{\sqrt{B(0)}}-1\right)\right]. \tag{3.6}$$

The rate at which DM particles accumulate in NSs is then given by

$$\frac{dN_\chi}{dt} = C - EN_\chi, \tag{3.7}$$

assuming that DM annihilation is negligible. The solution of this equation is

$$N_\chi(t_\star) = C\, t_\star \left(\frac{1-e^{-E\, t_\star}}{E\, t_\star}\right), \tag{3.8}$$

where $t_\star$ is the age of the NS. The term in brackets quantifies the depletion of the number of capture DM particles due to the evaporation process. This factor will be of order 1 unless $E(m_\chi)\, t_\star \gtrsim \mathcal{O}(1)$. Therefore, we will define the evaporation mass as the DM mass for which the previous relation holds, i.e. $E(m_{\rm evap})t_\star \sim 1$. For DM masses below this threshold, $m_\chi \lesssim m_{\rm evap}$, the capture and evaporation processes are in equilibrium with each other. In that limit, the net energy exchange in the star due to the combined effects of DM capture and evaporation would be negligible, and hence we would be unable to constrain DM interactions using the NS temperature as a probe.

Using Eq. 3.5, we find the evaporation mass to be of order $m_{\rm evap} \sim \mathcal{O}(100 T_\star)$ for all scattering targets in old NSs with $t_\star \sim \mathcal{O}(10\,{\rm Gyr})$. For instance, for $T_\star = 10^5\,$K and electron targets, we obtain $m^e_{\rm evap} \simeq 300\,$eV. The region in Fig. 3.5 for which capture and evaporation are in equilibrium is shaded in yellow, with the evaporation mass indicated by the dashed brown line. From this, we can see that the finite temperature effects on the capture rate come become importatnt for masses below the evaporation mass, for all operators we consider. Hence, when calculating the capture rate while aiming to constrain DM interactions, finite temperature effects can be safely neglected.

3.1.3 Results

Threshold Cross-Sections

In section 2.2.2, we defined the threshold cross-section, $\sigma_{\ell\chi}^{\rm th}$, as the cross-section for which the capture rate, $C(\sigma(\Lambda), m_\chi)$, calculated in the optically thin regime becomes equal to the geometric limit, $C_{\rm geom}$. The threshold cross-section restricts the NS sensitivity to DM-target interactions since for $\sigma \geq \sigma_{\ell\chi}^{\rm th}$ the capture rate saturates to the geometric limit $C_{\rm geom}$.

In Fig. 3.6, we show the threshold cross-sections for lepton targets, electrons and muons, and compare them with existing direct detection limits and expected sensitivities of future experiments. The neutrino floor for electron recoil experiments for silicon targets [118] is shown as a shaded yellow region. The solid light blue and magenta lines correspond to the value of σ_{th} for electrons and muons respectively, calculated using the NS model BSk24-2 ($1.5M_\odot$), while the shaded bands in light blue and magenta denote the expected range for σ_{th} for the two different targets, obtained by varying the NS configuration along the BSk24 family. BSk24-1 ($1M_\odot$) gives the upper bound on $\sigma_{\rm th}$ and BSk24-4 ($2.16M_\odot$) the lower bound. Note that the variation in $\sigma_{\rm th}$ due to the NS EoS increases with the DM mass and for muons goes from about one order of magnitude in the low mass range, to two orders of magnitude in the multiple scattering region. For electrons, this effect is slightly less pronounced.

All the limits for existing experiments are orders of magnitude weaker than the expected NS reach, with only the future DAMIC-M [119] (dashed brown line) expected to overcome NS electron scattering sensitivity and approach that of muons, in the DM mass range $3\,\text{MeV} \lesssim m_\chi \lesssim 30\,\text{MeV}$. Moreover, NS sensitivity to DM interactions with lepton targets is expected to be well below the neutrino floor for $m_\chi \gtrsim 100\,\text{MeV}$ and, in the case of muons, even for $m_\chi \lesssim 1\,\text{MeV}$.

Note that NSs have a better sensitivity to vector-vector interactions (operator D5, see right panel) than scalar-scalar interactions (operator D1, see left panel) in the low DM regime for both leptonic targets, and especially for electrons. As discussed in section 3.1.1, there is an additional suppression in the capture rate of

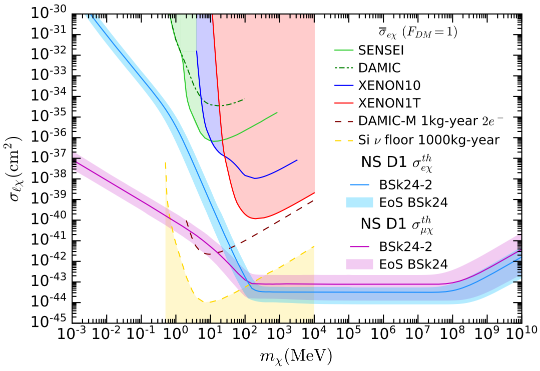

Figure 3.6: DM-lepton threshold cross-section for operators D1 (left) and D5 (right) for the EoS BSk24. The solid blue (electron) and magenta (muon) lines represent $\sigma_{\rm th}$, are computed assuming the NS model BSk24-2, while the shaded bands represent the expected range due to variation of the EoS. For comparison, we show leading electron recoil bounds for heavy mediators from SENSEI [120], DAMIC [121], Xenon10 [122], Xenon1T [123], projected sensitivities from DAMIC-M [119] as well as the neutrino floor for silicon detectors [118].

scalar operators that stems from an $m_e^2 t$ term in their scattering amplitudes.

Similar threshold cross-sections can be estimated for the remaining operators. Operators with s-dependent matrix elements (D6-D10) have $\sigma_{\rm th}$ that behave like that of D5 for both electrons and muons. D2 presents the same features as D1 in the sub-GeV regime for electrons, due to the similar shape of their capture rates (see Fig. 3.2) and D3-D4 show a steeper slope in the $m_\chi \lesssim m_e$ region with respect to D1-D2, due to the capture rate dependence on higher powers of t.

Comparison with Literature

We now compare our calculations for the capture rates and resulting reach in the EFT cutoff Λ for operators D1 and D5 to those presented in Refs. [124, 125][2]. The formalism in Refs. [124, 125] is valid for relativistic and non-relativistic targets in a broad mass range, however, several simplifying assumptions were made that are accounted for in our results. Namely, they do not account for the DM velocity distribution far from the star, nor do they incorporate the internal structure of the NS. Instead, constant chemical potentials and particle abundances that have been averaged over the core volume are used. These quantities correspond to the NS

[2]Note that the Yukawa couplings for scalar and pseudoscalar operators in Refs. [124, 125] are embedded into the cutoff scale Λ.

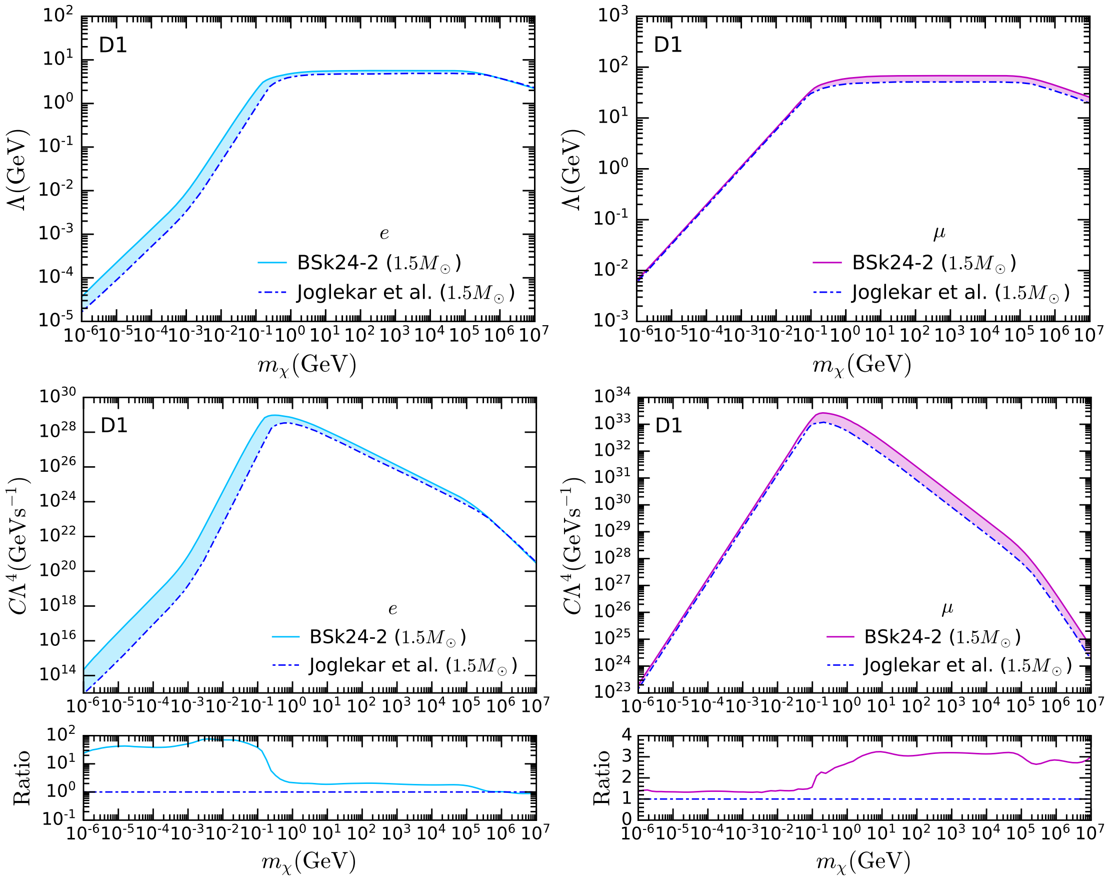

Figure 3.7: Comparison of the reach in Λ for D1 with the approach of Ref. [125]. The shaded regions denote the difference in Λ (top) and $C\Lambda^4$ (middle) between the two approaches and their ratio is shown in the bottom panels.

model BSk24-2 and were calculated in Ref. [126].

In the top panels of Figs. 3.7 and 3.8, we compare the reach in Λ for DM-lepton scattering cross-sections in Refs. [124, 125] with the cutoff scale we obtain for the maximum capture rate, $C(\Lambda, m_\chi) = C_{\rm geom}$. Our results differ the most for electron targets in the Pauli suppressed region by a factor of $\sim$ 2.5, and we find Pauli blocking is active at a slightly lighter DM mass. This arises from our use of the full radial profiles for the NS input parameters, and that light DM particles whose interactions are subject to Pauli blocking are captured closer to the surface [99]. The discrepancy is reduced to a factor of $\sim$ 1.25 in the intermediate mass region and there is almost no difference in the large mass regime. For muons, we find a Λ that is, on average, a factor $\sim$ 1.33 greater than that of Refs. [124, 125] along the whole DM mass range for D5, and is in almost perfect agreement in the $m_\chi \lesssim m_\mu$

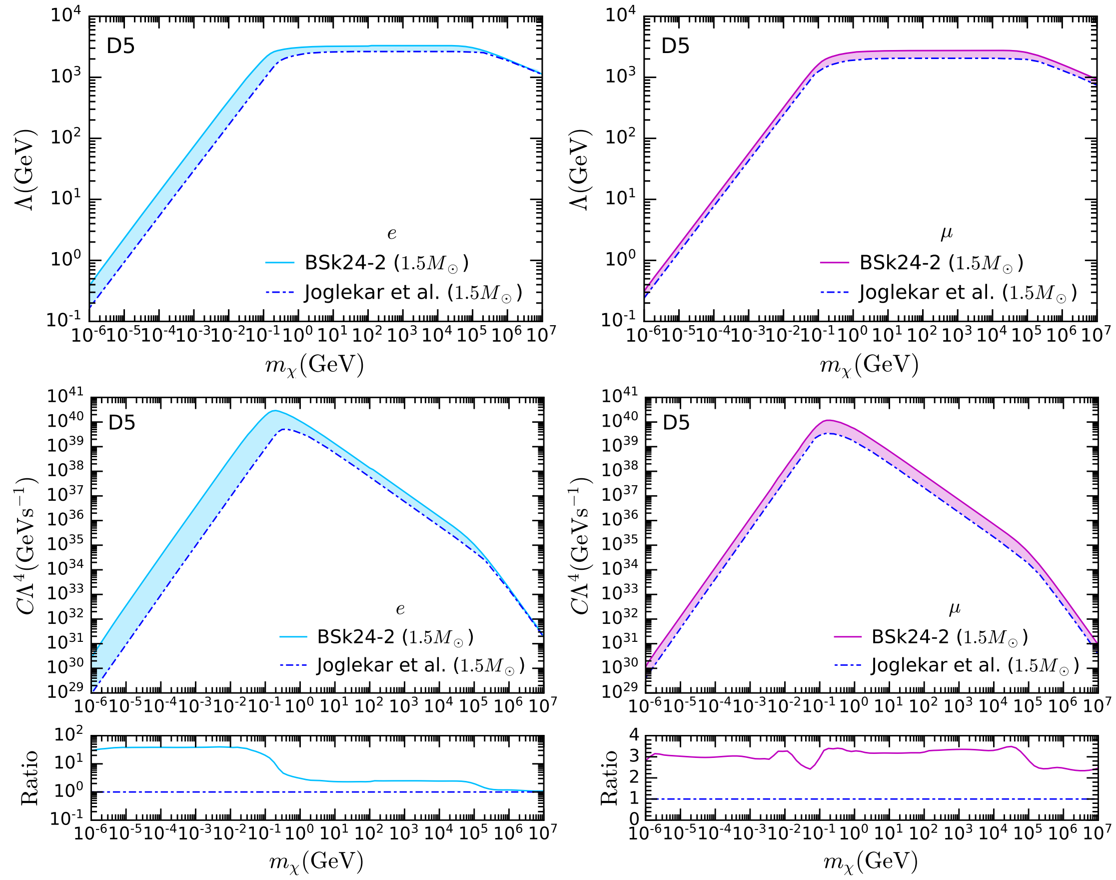

Figure 3.8: Same as Fig. 3.7 but for the vector operator D5.

region for D1.

In the middle panels of Figs. 3.7 and 3.8 we show how these small differences in the two approaches translate to differences in the capture rate, comparing $C\Lambda^4 = \Lambda^4 C_{\rm geom}$ obtained with the two formalisms. Since the geometric limit of the capture rate is not defined in Refs. [124, 125], we use a definition similar to Eq. 2.27 that is compliant with the assumptions made by these authors. For electron scattering, we see that the formalism that does not account for the NS internal structure underestimates the capture rate in the region affected by Pauli blocking by a factor ~ 40 (bottom LH panels of Figs. 3.7 and 3.8). This difference is slightly larger in the region where the Pauli suppression is stronger, becoming almost a factor of ~ 100 for D1 in the range $m_e \lesssim m_\chi \lesssim 100\,\mathrm{MeV}$. For muons, the difference between the two approaches is less pronounced, with a maximum ratio of ~ 3.5 for both operators.

3.2 Capture from Electrons in White Dwarfs

We now turn our attention to DM capture in white dwarfs, where the degenerate electrons preventing these stars from gravitational collapse are a perfect candidate for the capture formalism we have constructed. Not only are the electrons extremely degenerate, with chemical potentials $\varepsilon_{F,e} \gg m_e$ in some stars, but they can also be ultra-relativistic. As the gravitational fields of WDs are significantly weaker than those of NSs, the incoming DM does not get boosted to relativistic velocities in this case. This leads to the scattering interactions taking place in an interesting kinematic regime, as we are dealing with non-relativistic DM scattering off ultra-relativistic electrons.

3.2.1 Capture Rates

Single scattering

The kinematics involved in treating the scattering of non-relativistic DM off ultra-relativistic electrons requires a few modifications to the interaction rate derived in section 2.2.3, Eq. 2.39. We also reintroduce the dependence of the capture rate on the DM-target relative velocity distribution, $f_{\rm MB}(u_\chi)$, one might be interested in departures from the standard MB speed distribution. The generalised expression for the capture rate without integrating over the DM velocity u_χ is

$$C = 4\pi \frac{\rho_\chi}{m_\chi} \int_0^\infty \frac{f_{\rm MB}(u_\chi) du_\chi}{u_\chi} \int_0^{R_\star} \eta(r) r^2 \frac{\sqrt{1-B(r)}}{B(r)} \Omega^-(r)\, dr, \tag{3.9}$$

where interaction rate between DM and the electron targets is given by [99, 100]

$$\begin{aligned}\Omega^-(r) = \frac{\zeta(r)}{32\pi^3} \int dt dE_e ds \frac{|\overline{M}_{e\chi}|^2}{2s\beta(s)-\gamma^2(s)} \frac{E_e}{m_\chi} \sqrt{\frac{B(r)}{1-B(r)}} \frac{s}{\gamma(s)} \Theta\left(E_e' - E_e\right) \\ \times f_{\rm FD}(E_e, r)(1-f_{\rm FD}(E_e', r)) \Theta\left(E_e \sqrt{\frac{1-B(r)}{E_e^2 - m_e^2}} - \frac{s_{\max} + s_{\min} - 2s}{s_{\max} - s_{\min}}\right),\end{aligned} \tag{3.10}$$

$$\beta(s) = s - \left(m_e^2 + m_\chi^2\right), \tag{3.11}$$

$$\gamma(s) = \sqrt{\beta^2(s) - 4m_e^2 m_\chi^2}, \tag{3.12}$$

where E_e and E_e' are the target electron initial and final energies, respectively. The correction factor $\zeta(r) = \frac{n_e(r)}{n_{\rm free}(r)}$ accounts for the fact we are using realistic profiles for the electron number density $n_e(r)$ and the chemical potential $\varepsilon_{F,e}(r)$, while the interaction rate is defined in the free Fermi gas approximation [99, 108, 127]. The definition of $n_{\rm free}(r)$ can be found in Ref. [99]. The integration intervals in Eq. 3.10 are

$$t_{\rm max} = 0, \tag{3.13}$$
$$t_{\rm min} = -\frac{\gamma^2(s)}{s}, \tag{3.14}$$
$$s_{\rm min} = m_e^2 + m_\chi^2 + 2\frac{E_e m_\chi}{\sqrt{B(r)}} - 2\sqrt{\frac{1-B(r)}{B(r)}} m_\chi \sqrt{E_e^2 - m_e^2}, \tag{3.15}$$
$$s_{\rm max} = m_e^2 + m_\chi^2 + 2\frac{E_e m_\chi}{\sqrt{B(r)}} + 2\sqrt{\frac{1-B(r)}{B(r)}} m_\chi \sqrt{E_e^2 - m_e^2}, \tag{3.16}$$
$$E_{e,\rm min} = m_e, \tag{3.17}$$

while $E_{e,\rm max}$ should be set to $E_{e,\rm max} = m_e + \varepsilon_{F,e}$ in the $T_\star \to 0$ limit, or left free otherwise.

We have introduced two additional Θ functions in Eq. 3.10 when compared to Refs. [99, 100]. The first Θ function ensures that we count only scatterings that are kinematically allowed, in this case requiring that the collision is head-on. We explain the details of the derivation of this phase space constraint in Appendix A.5. The second Heaviside function enforces that the DM loses energy, which is required for finite temperature calculations. In the zero temperature limit, on the other hand, the FD distributions can themselves be approximated by Θ functions. Therefore, the initial states occupy all the lower energy levels, and scattering can proceed only if the target acquires enough energy to be ejected from the Fermi Sea. Specifically, the inequalities enforced are

$$E_e \leq m_e + \varepsilon_{F,e}, \tag{3.18}$$
$$E_e' > m_e + \varepsilon_{F,e}. \tag{3.19}$$

It is also worth noting that when computing the capture rate while keeping the leading order terms in the inital DM energy, i.e. setting $E_\chi = m_\chi(1/\sqrt{B(r)} + u_\chi^2/2)$ in the interaction rate, we find that there is no significant effect compared to setting $u_\chi \to 0$ and using Eq. 2.26 instead. This can be understood by noting that the halo velocities are of order $u_\chi^2 \sim 10^{-6}$, while the escape velocity is $v_{esc}^2 = 1 - B(r) \sim 10^{-3}$, and so the corrections are expected to be only of order $u_\chi^2/v_e^2 \sim 10^{-3}$. It is worth noting that in the case of scatting of the ions in WDs the $u_\chi \to 0$ approximation is less justifiable, discussed in Ref. [113].

Multiple Scattering

In the optically thin limit, and for DM masses larger than a certain threshold denoted m_e^*, the single scatter capture probability is no longer ~ 1. In this regime, multiple collisions are required for the DM particles to lose sufficient energy to be captured. In the $T_\star \to 0$ limit, one can use the multiple scattering approach outlined in section 2.4.2, which involves inserting the capture probability $c_1(r)$ in Eq. 3.10 instead of the $\Theta\left(E_e' - E_e\right)$ term, with

$$c_1(r) = 1 - e^{-\frac{m_e^*(r)}{m_\chi}} \sim \frac{m_e^*(r)}{m_\chi}. \tag{3.20}$$

Since the DM energy loss for scattering on electrons is much larger than the WD core temperature, as is the case for DM scattering in neutron stars, we can calculate m_e^* using the same method as for NS in the previous chapter. We assume a MB velocity distribution for the DM velocities in M4, with $v_\star = 20\,\mathrm{km\,s^{-1}}$, $v_d = 8\,\mathrm{km\,s^{-1}}$. Taking a WD of mass $M_\star = 1.38 M_\odot$, a constant matrix element, $B = 0.995$ and $\varepsilon_{F,e} = 8\,\mathrm{MeV}$, we find a typical value of

$$m_e^* \simeq 10^5\,\mathrm{GeV}. \tag{3.21}$$

Capture Rates for Electron Scattering

We are now ready to calculate the capture rate for the operators in Table **??**, for DM-electron interactions with $\Lambda_f = \Lambda_e$, $\mu = m_\chi/m_e$ and the coefficients c_N^I, $I = S, P, V, A, T$ set to 1. In Fig. 3.9, we present our results for $C\Lambda_e^4$ in the zero temperature and optically thin limits for carbon WDs with $M_\star = 0.49 M_\odot$ (top panels) and $M_\star = 1.38 M_\odot$ (bottom panels). In both WDs, Pauli blocking strongly suppresses the capture rate in the light mass regime, $m_\chi \lesssim 100\,\mathrm{MeV}$. Above this mass range, Pauli suppression persists but remains minimal.

The change of slope in the Pauli suppressed region for operators D1 and D2 is due to their matrix elements containing a factor $(t - 4m_e^2)$, which introduces an additional suppression due to the smallness of the electron mass in the $m_e \lesssim m_\chi \lesssim 100\,\mathrm{MeV}$ interval [100]. This was also present in the NS case discussed in the previous section. Then, a transition between the Pauli blocked and the unsuppressed capture rate is observed for all the operators, which is immediately noticeable in the case of the light WD, where we observe a valley in the $100\,\mathrm{MeV} \lesssim m_\chi \lesssim 1\,\mathrm{GeV}$ mass range. In the heavy WD, this transition region extends up to $\sim 10\,\mathrm{GeV}$ and is more evident for operators D5-D10. The region at which multiple scattering becomes relevant also depends on the star configuration. It occurs at $m_\chi \gtrsim 1\,\mathrm{TeV}$ for the light WD, and at around $m_\chi \gtrsim 10^5\,\mathrm{GeV}$ for the heavy WD, observed as a change of slope in the capture rate at around those masses.

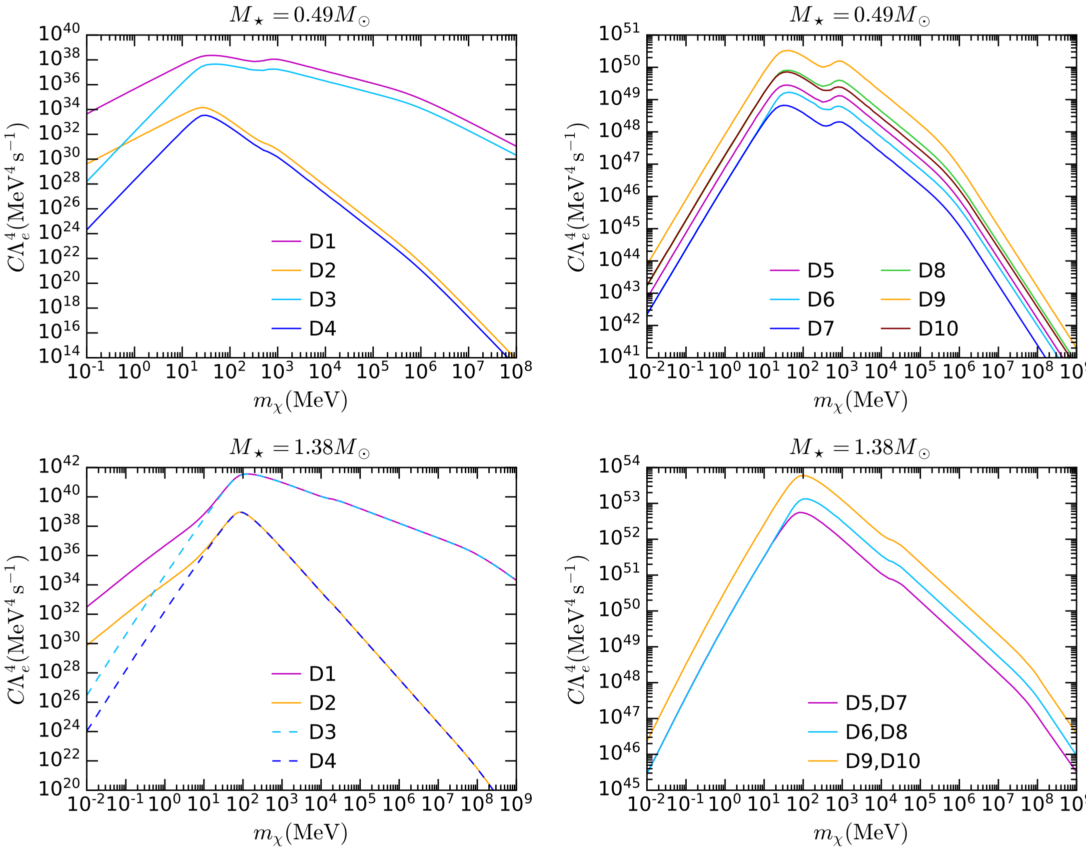

Figure 3.9: Capture rate for scattering on electrons, in the optically thin limit, as a function of the DM mass for the lightest (WD_1, top panels) and heaviest (WD_4, bottom panels) carbon WDs in Table **??**.

It is worth remarking that, in contrast to the light WD, the heavy WD features an electron chemical potential more than one order magnitude higher, and that the electrons here are ultra-relativistic. As a result, the capture rate curves for WD_4 exhibit similar features to those observed in neutron stars where electrons are degenerate and ultra-relativistic [100]. In addition, since the electrons in the heavy WD are relativistic, the scattering amplitudes are dominated by terms of the form $t^n s^m$ in the large DM mass regime, while terms proportional to m_e^2 are suppressed (see Table **??**). This results in very similar capture rates for operators D1 and D3, D2 and D4, D5 and D7, D6 and D8, D9 and D10.

Finally, we note that the capture rate due to scattering on electrons would scarcely be affected by a different chemical composition, such as He or O.

3.2.2 Finite Temperature Effects and Evaporation

As was observed in the case of DM scattering off electrons in NSs, accounting for the finite temperature of the star can have a large impact when the dark matter mass is low. There are two main effects to consider. First, there is a boost in the capture and interaction rates as there is a greater volume of phase space for the interactions to take place in. This is due to the DM energy loss, q_0, being bounded from above such that $q_0^{\mathrm{MAX}} \lesssim 3\,\mathrm{MeV}$ at zero temperature, and so only the outer shell of the Fermi sphere contributes to the capture rate. In comparison, non-zero $T_\star$ allows deeper shells of the Fermi sphere to contribute, substantially iincreasing the capture rate. Calculating the capture rate for finite $T_\star$ is achieved by using the full form of the Fermi-Dirac distributions in Eq. 3.10, instead of approximating them with Θ-functions, and removing the upper limit on the E_e integration interval.

Second, evaporation of the captured DM becomes possible due to scattering off the thermal electrons. Again, this is relevant for low-mass DM. For these finite temperature effects to be relevant in DM capture, they need to come into effect at DM masses above the evaporation mass of the WD [100, 108]. To estimate the evaporation rate, we use the full expression obtained in section 3.1.2 for neutron stars, reiterated here for electrons in WDs

$$E \sim \frac{m_\chi m_e^2 \sigma_{e\chi}}{4\pi^2} \left(\frac{1}{\sqrt{B(0)}} - 1 \right)^2 \exp \left[-\frac{m_\chi}{T_\star} \left(\frac{1}{\sqrt{B(0)}} - 1 \right) \right], \tag{3.22}$$

when the accreted DM is confined close to the centre of the star. Note that the evaporation rate is driven by the ratio $m_\chi/T_\star$, and as such is enhanced for light DM.

In Fig. 3.10, we plot the ratio of the capture rate for $T_\star = 10^5\,\mathrm{K}$ to the zero temperature approximation for the same WDs as in Fig. 3.9. Operators that depend

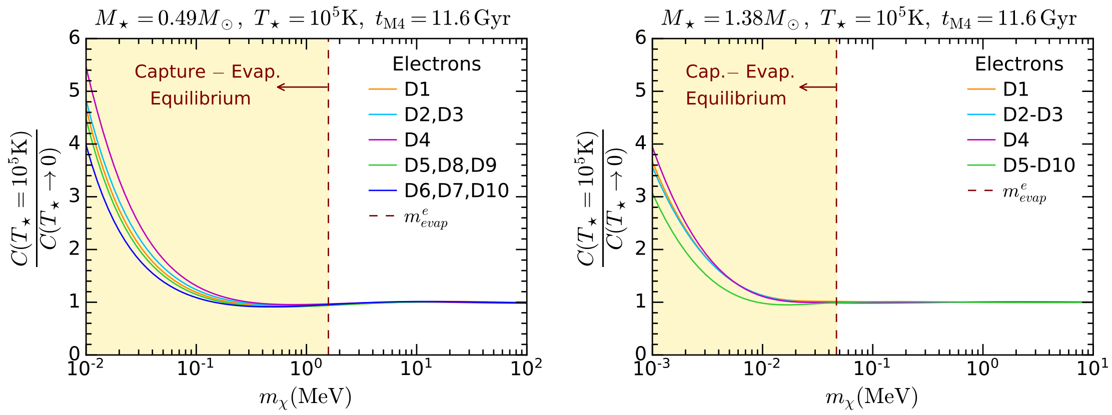

Figure 3.10: Finite temperature effects on the capture rate in the case of scattering on electron targets, for two WDs in the globular cluster M4, namely WD_1 (left) and WD_4 (right) in Table 1.1. The DM mass range where capture and evaporation are expected to be in equilibrium is shaded in yellow. The dashed brown line corresponds to the evaporation mass.

only on powers of the exchanged momentum t, namely D1-D4, are the most affected by finite temperature corrections, followed by operators that contain in their matrix elements linear terms of the form $t^n s^m$, i.e., D5-D10. As can be noticed, the DM mass range at which these effects become relevant depends on the specific WD configuration and similar to the NS case is always below the evaporation mass for electron scattering $m^e_{\rm evap}$ (dashed brown lines). We find that the evaporation mass for carbon WDs with $T_\star = 10^5$ K ranges from $m^e_{\rm evap} \sim 50$ keV ($M_\star = 1.38 M_\odot$, right panel) to $m^e_{\rm evap} \sim 1.5$ MeV ($M_\star = 0.49 M_\odot$, left panel). The evaporation mass is larger in warmer WDs, e.g. $T_\star = 10^6$ K, with an increase of one order of magnitude in $T_\star$ resulting in a similar rise in $m^e_{\rm evap}$.

3.2.3 DM Induced Heating of WDs in GC M4

In this section, we calculate bounds on the cutoff scale of the dimension 6 EFT operators that describe DM interactions with electrons in WDs. To that end, we use the observed luminosity of the faintest WDs in the globular cluster M4 [20, 36], together with the estimations for ρ_χ, $v_\star$ and v_d derived in Ref. [36]. We compute the capture rate in the optically thin limit, assuming that the WDs are made of ^{12}C. Even though colder WDs have been recently observed by the Gaia mission [17], no significant bounds can be derived from this data due to the low DM density in the solar neighbourhood.

Once captured, the gravitationally bound DM will continue to scatter with the WD constituents until they reach thermal equilibrium. We have checked the thermalisation timescales for scattering on electrons, using the method described in Ref. [110]. We find that the longest time requiredfor the DM to thermalize is $\sim 10^5$ yrs for any of the operators of interest.

Following thermalisation, the DM can self-annihilate in the WD interior. The number of DM particles present in the WD core therefore evolves as

$$\frac{dN_\chi}{dt} = C - AN_\chi^2, \tag{3.23}$$

where the coefficient A is related to the annihilation rate through

$$\Gamma_{\rm ann} = \frac{1}{2} AN_\chi^2, \tag{3.24}$$

and we have assumed that evaporation is negligible, i.e., $m_\chi \geq m_{evap}$. The annihilation coefficients can be calculated from the thermally averaged annihilation cross-sections for each operator that can be found in Ref. [128]. To calculate these cross-sections, we only consider DM annihilating to SM leptons at tree level, as there is no a priori reason to expect similar scale DM couplings to quarks, nor for them to be related in any specific way. In principle one would have two cutoff scales for DM coupling to the quark and lepton sectors respectively, with the details depending on the UV phyiscs. This means that when computing bounds on Λ_e for interactions with electrons, no assumptions were made regarding the strength of DM-quark interactions. Instead, loop-induced effective couplings to quarks were calculated similarly to Refs. [126, 129]. Importantly, note that below the electron mass annihilation to neutrinos, or loop-induced annihilation to photons (non-zero only for some operators) are the only allowed annihilation channels.

If the capture and annihilation processes are in equilibrium, then $\Gamma_{ann} = C/2$ and the DM contribution to the star luminosity is $L_\chi = m_\chi C(m_\chi, \Lambda_f)$. The time in which this equilibrium is reached is determined by the steady state solution of Eq. 3.23, and is given by

$$\tau_{\rm eq} = \frac{1}{\sqrt{CA}}. \tag{3.25}$$

We can then set the EFT cutoff Λ_f to the values obtained from the WD luminosity (see paragraph below) to calculate the corresponding equilibrium times, and hence verify that capture-annihilation equilibrium is met. For electrons, the resulting times are significantly less than the age of the WDs. For ions, timescales longer than 1 Myr are required to reach equilibrium in the case of operator D1 with DM mass $\lesssim 1\,\mathrm{GeV}$, while D2 can take as long as 10^4 yrs in the mass range of interest. The remaining operators all rapidly reach equilibrium. Given we are interested in

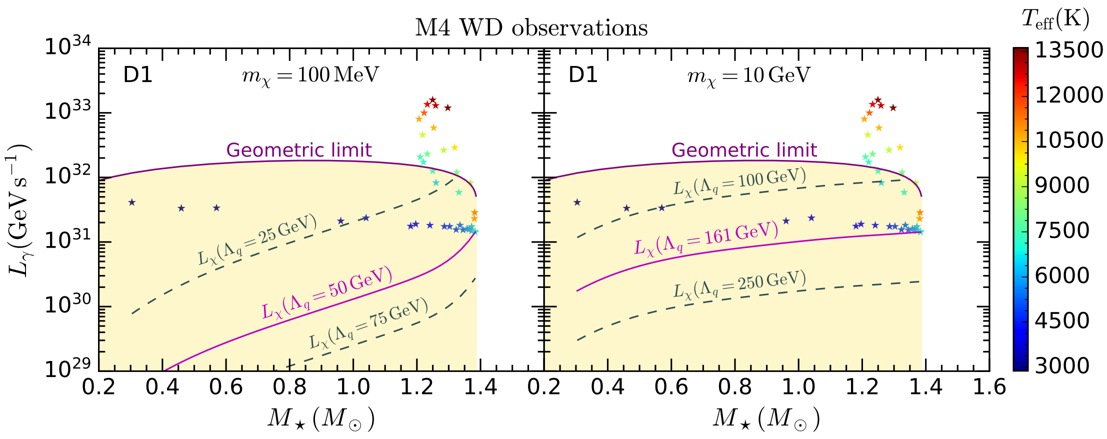

Figure 3.11: WDs observed in the globular cluster M4 and DM contribution to the star luminosity L_χ for different values of the cutoff scale Λ_q and m_χ for D1. The dark violet lines correspond to the maximum achievable L_χ for nucleon targets, obtained in the geometric limit. The magenta lines represents the minimum value of Λ_q that is consistent with the WD observations.

old WDs, with ages of order $\sim$ Gyrs, we conclude that capture-annihilation is safely met for all cases of interest.

To estimate the limits on the cutoff scale Λ_f for DM interactions with SM fermions, we compare the luminosity due to DM with the WD observed luminosities L_γ. In Fig. 3.11, we illustrate how we have performed this calculation for DM scattering with nuclei, i.e., to determine Λ_q. The observed luminosity of the WDs in M4 is shown in the $L_\gamma - M_\star$ plane[3], where we have used the effective temperature to infer the radius of every star. Since, there are no independent measures of the mass of the WDs in M4 and we require radial profiles of the target number density, electron Fermi energy and escape velocity to compute capture and evaporation rates, we have solved the TOV equations coupled with the FMT EoS for carbon WDs to calculate $M_\star$.[4] We also show the DM luminosity for different values of Λ_q for $m_\chi = 100\,\mathrm{MeV}$ (left) and $m_\chi = 10\,\mathrm{GeV}$ (right), calculated using different WD configurations. As can be seen, the WD with $M_\star \simeq 1.38 M_\odot$ is the star that imposes a lower bound on Λ_q (solid magenta line), since L_γ should be at least equal to the expected contribution from DM for all the observed WDs. In other words, if the

[3]Actually, more WDs were observed in the globular cluster M4 than those shown in Fig. 3.11. We have given preference to the faintest WDs.

[4]The mass and radius obtained using this method are in good agreement with recent observations within 2 kpc retrieved from the Montreal White Dwarf Database [130], which contains more than 32000 WDs identified by Gaia DR2 [131] and EDR3 [30], and spectroscopy measurements from surveys including SDSS DR12 and 2MASS.

luminosity due to DM capture and annihilation is at most equal to the observed luminosity of the faintest and heaviest WD in M4 ($M_\star \simeq 1.38 M_\odot$), there will be no tension between these observations and DM induced heating of WDs. While the results in Fig. **??** assume WDs of a pure carbon composition, we have checked that a pure He composition for stars of $M_\star \lesssim 0.5 M_\odot$ does not alter the bounds on Λ_q. Note that the lower bounds are always well below the DM luminosity for maximal capture probability (geometric limit, see purple lines). Lower values of Λ_q (dashed grey lines) would be in tension with the lowest luminosity WDs.

In Fig. 3.12, we show the limits on the cutoff scale Λ_e, in the case where DM is captured solely by collisions with the degenerate electrons. The shaded blue regions are the excluded parameters. For operators D1-D4, for which the squared matrix elements depend exclusively on the transferred momentum t, the DM-electron couplings is proportional to the tiny electron Yukawa coupling. This reduces the capture rate in such a way that for operator D4, the bounds on Λ_e lie entirely in the $\Lambda_e \lesssim m_\chi$ region and for D2 only a small corner of the allowed parameter space surpasses this threshold. Given these low limits on the EFT cutoff scale Λ_e, such that an EFT description would not be valid, we do not plot results for D4 or D2. For the remaining operators, especially D5-D10, there is a much larger region of parameter space where the limits on Λ_e are such that an EFT description would be valid. In all cases, the lower limits on Λ_e, obtained using the WD with $M_\star = 1.38 M_\odot$ in M4, outperform the leading bounds from electron recoil experiments by at least $\sim$ an order of magnitude. In most cases, they even outshine the projected sensitivity for the future experiment DAMIC-M (with the exceptions being D1, D5, D8 and D9 in the region below $m_\chi \lesssim 10\,\text{MeV}$ – see dot-dashed green lines). DM scattering on electrons is heavily hampered by Pauli blocking for $m_\chi \lesssim 100\,\text{MeV}$. The reach in the light DM mass regime is restricted by the evaporation mass for operators D1, D7 and D8 (see yellow region) and the electron mass for D3, D5, D6, D9 and D10 (see region shaded in grey) where DM annihilation to neutrinos is either the only final state allowed or the dominant channel. Despite those limitations, we conclude that constraints from the observed luminosity of cold faint WDs in old globular clusters that have been able to retain their initial DM content in the innermost region of the cluster, can potentially exclude larger regions of the parameter space than direct detection, particularly in the sub-GeV region. This is especially relevant for leptophilic DM models.

Finally, in Fig. 3.13, we conservatively compare the bound on the scattering cross-section of the vector-vector operator obtained from WDs in M4, with the limits from electron recoil experiments. Even though the WD constraint is not able to probe the region where neutrino coherent scattering is expected to hamper the sensitivity of silicon detectors, or extend down below the electron mass, it would certainly surpass current DD bounds by orders of magnitude in $\sigma_{e\chi}$. It would even surpass the projected sensitivity for DAMIC-M, especially in the sub-MeV regime where no projections have been made[5], despite the reduced WD sensitivity in this region due to Pauli blocking.

[5]In the sub-MeV DM mass regime, modest limits on the DM-electron scattering cross-section can be obtained by considering DM upscattered by cosmic rays. See, e.g. Refs. [132–134].

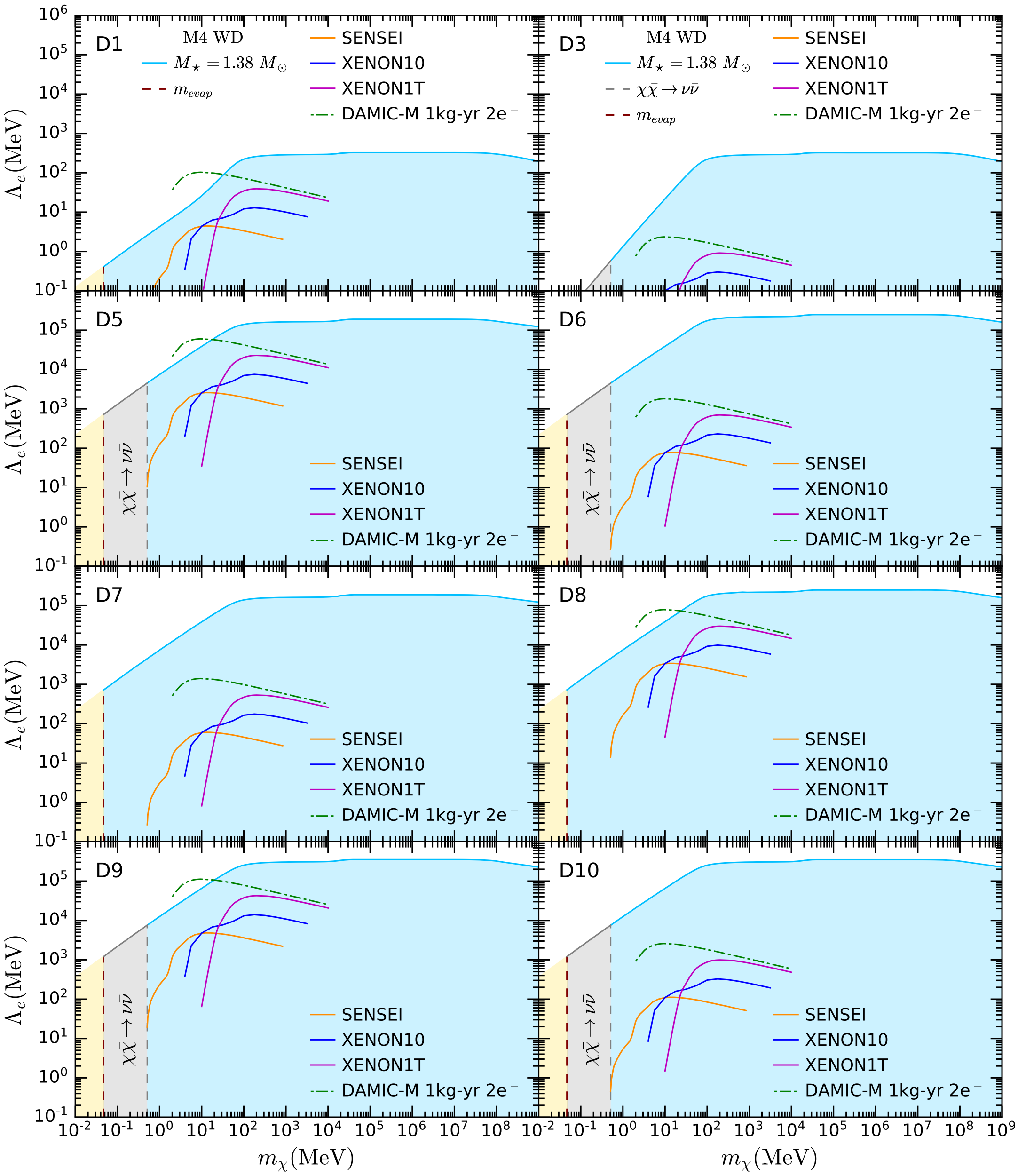

Figure 3.12: Limits on Λ_e for DM interactions with electrons for the same WD obtained with the lowest luminosity and heaviest WD in the globular cluster M4, assuming $\rho_\chi = 798\,\mathrm{GeV\,cm^{-3}}$ (contracted halo) [36] and $T_\star = 10^5$ K.. The region where capture and evaporation (for $T_\star = 10^5$ K) are expected to be in equilibrium is shaded in yellow, and the region where DM annihilates to neutrinos that escape the WD is shaded in grey. For comparison, we show upper bounds from the leading electron recoil experiments for heavy mediators from SENSEI [120]/DAMIC [121], Xenon10 [122], Xenon1T [123] and the projected sensitivity for DAMIC-M [119].

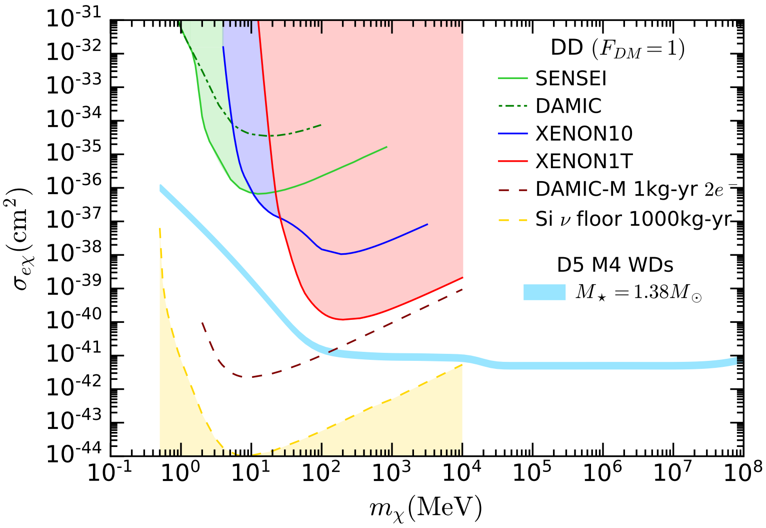

Figure 3.13: Upper bounds on the DM-electron scattering cross-section for D5. The light blue band represents the limit from the WD observations in M4. The band width denotes the uncertainty in the DM density in M4 [36]. For comparison we show leading electron recoil bounds for heavy mediators from SENSEI [120], DAMIC [121], Xenon10 [122], Xenon1T [123], the projected sensitivity for DAMIC-M [119], and the neutrino floor for silicon detectors [118].

A

Dark Matter Interaction Rates

A.1 General Interaction Rates for Scattering within a Degenerate Media

The most general form of the interaction rate, following Ref. [110], can be written in terms of the spin-averaged squared matrix element, $|\overline{\mathcal{M}}|^2$, as

$$\Gamma = \int \frac{d^3k'}{(2\pi)^3} \frac{1}{(2E_\chi)(2E'_\chi)(2m_i)(2m_i)} \Theta(E'_\chi - m_\chi)\Theta(\pm q_0) S(q_0, q), \quad (A.1)$$

$$\begin{aligned} S(q_0, q) = 2 \int \frac{d^3p}{(2\pi)^3} \int \frac{d^3p'}{(2\pi)^3} \frac{m_i^2}{E_i E'_i} |\overline{\mathcal{M}}|^2 (2\pi)^4 \delta^4 \left(k_\mu + p_\mu - k'_\mu - p'_\mu\right) \\ \times f_{\rm FD}(E_i)(1 - f_{\rm FD}(E'_i))\Theta(E_i - m_i)\Theta(E'_i - m_i), \end{aligned} \quad (A.2)$$

where $S(q_0, q)$ is the target response function that depends on the energy and momentum transfers, q_0 and q respectively. E_χ and E_i are the DM and target initial energies, with k and p their respective momenta. Primed variables represent final state quantities.

The δ-function can be used to perform the d^3p' integrations, leaving

$$\begin{aligned} S(q_0, q) = \frac{1}{2\pi^2} \int d^3p \, \frac{m_i^2}{E_i E'_i} |\overline{\mathcal{M}}|^2 \delta\left(q_0 + E_i - E'_i\right) f_{\rm FD}(E_i)(1 - f_{\rm FD}(E'_i)) \\ \times \Theta(E_i - m_i)\Theta(E'_i - m_i). \end{aligned} \quad (A.3)$$

After this, the final state target energy is fixed to

$$E'_i(E_i, q, \theta) = \sqrt{m_i^2 + (\vec{p} + \vec{q})^2} \quad (A.4)$$

$$= \sqrt{E_i^2 + q^2 + 2qp\cos\theta} > m_i, \quad \forall p, q, \theta, |\cos\theta| < 1, \quad (A.5)$$

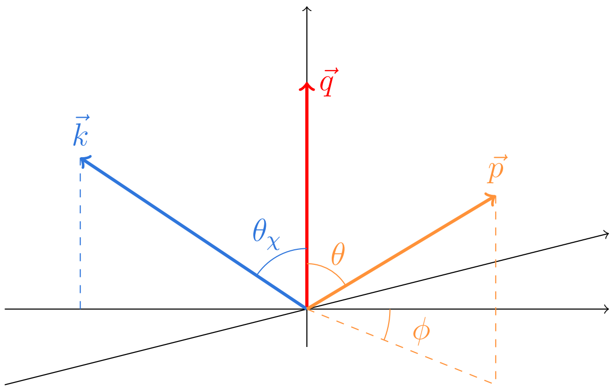

Figure A.1: Schematic of kinematics for dark matter interacting with a target in the frame of the star. We set the momentum transfer to lie along the z-axis with the initial momenta defined relative to it.

where θ is the angle between the target initial momentum and the transferred momentum, $\vec{q}$, that is defined below. To perform the remaining integrals, we write $d^3p = pE_i dE_i \, d\cos\theta \, d\phi$. The kinematics of this interaction are depicted in Fig. A.1, where the incoming momenta are defined relative to the momentum transfer that is set to lie along the z-axis. In doing so, we must account for the fact that in this frame we cannot assume all three of the vectors are coplanar, and assign the additional azimuthal angle ϕ to the target momentum.

In general, the squared matrix elements we are interested in can be expressed as polynomials in the Mandalstam variables s and t, such that

$$|\overline{\mathcal{M}}|^2 = \sum_{n,m} \alpha_{n,m} t^n s^m. \tag{A.6}$$

Writing $s = m_\chi^2 + m_i^2 + 2E_\chi E_i - 2\vec{p} \cdot \vec{k}$, the quantity $\vec{k} \cdot \vec{p}$ is obtained by analysing the kinematics of the interaction. From the diagram in Fig. A.1, we can write the inital momenta as

$$\vec{k} = (k \sin\theta_\chi, 0, k\cos\theta_\chi), \tag{A.7}$$
$$\vec{p} = (p\sin\theta\cos\phi, p\sin\theta\sin\phi, p\cos\theta). \tag{A.8}$$

The angles can then be expressed in terms of the other kinematic quantities by noting that

$$E'_\chi = \sqrt{m_\chi^2 + (\vec{k} - \vec{q})}, \tag{A.9}$$

$$\implies (E_\chi - q_0)^2 = m_\chi^2 + (k^2 + q^2 - 2kq\cos\theta_\chi) \tag{A.10}$$

$$\implies \cos\theta_\chi = \frac{q^2 - q_0^2 + 2E_\chi q_0}{2q\sqrt{E_\chi^2 - m_\chi^2}}, \tag{A.11}$$

$$E'_i = \sqrt{m_i^2 + (\vec{p} + \vec{q})}, \tag{A.12}$$

$$\tag{A.13}$$

for the dark matter angle, and

$$\implies (E_i + q_0)^2 = m_i^2 + (p^2 + q^2 + 2pq\cos\theta) \tag{A.14}$$

$$\implies \cos\theta = \frac{q_0^2 - q^2 + 2E_i q_0}{2q\sqrt{E_i^2 - m_i^2}} \tag{A.15}$$

for the target angle. These result in

$$\vec{k}\cdot\vec{p} = kp\sin\theta_\chi\sin\theta\cos\phi + kp\cos\theta_\chi\cos\theta \tag{A.16}$$

$$= kp\left[\sqrt{1 - \frac{(q^2 - q_0^2 + 2E_\chi q_0)^2}{4q^2(E_\chi^2 - m_\chi^2)}}\sqrt{1 - \frac{(q_0^2 - q^2 + 2E_i q_0)^2}{4q^2(E_i^2 - m_i^2)}}\cos\phi + \frac{(q^2 - q_0^2 + 2E_\chi q_0)(q_0^2 - q^2 + 2E_i q_0)}{4q^2\sqrt{E_\chi^2 - m_\chi^2}\sqrt{E_i^2 - m_i^2}}\right] \tag{A.17}$$

$$= \frac{(q^2 - q_0^2 + 2E_\chi q_0)(q_0^2 - q^2 + 2E_i q_0)}{4q^2} + \sqrt{E_\chi^2 - m_\chi^2 - \frac{(q^2 - q_0^2 + 2E_\chi q_0)^2}{4q^2}}\sqrt{E_i^2 - m_i^2 - \frac{(q_0^2 - q^2 + 2E_i q_0)^2}{4q^2}}\cos\phi. \tag{A.18}$$

This makes explicit that s is now a function of the azimuthal angle ϕ.

We then use the remaining delta function to integrate over θ, giving rise to a step function $\Theta(1 - \cos^2\theta(q, q_0, E_i))$, leaving the

$$S(q_0, q) = \alpha t^n \frac{m_i^2}{2\pi^2 q}\int dE_i d\phi s^m f_{\rm FD}(E_i)(1 - f_{\rm FD}(E_i + q_0))\Theta(E_i)\Theta(1 - \cos^2\theta). \tag{A.19}$$

It will be more convenient to work with the kinetic energies of the targets rather than their total energies, as we are only interested in elastic scattering. From here on out, E_i will refer to the kinetic energy of the target, i.e. $E_i \to E_i + m_i$.

This is compensated by using the Fermi kinetic energy in the FD distributions, $\varepsilon_{F,i} = \mu_{F,i} - m_i$.

The ϕ integrals can be easily computed for a given power of s, in general resulting in a messy function of the kinematic variables. However, we know that they will always be a polynomial of degree m, and so to make this explicit while keeping things as tidy as possible, we define the polynomials $\mathcal{U}_m(q^2, q_0, E_\chi, E_i)$ as

$$\mathcal{U}_m = \frac{q^{2m}}{2\pi}\int_0^{2\pi} d\phi \; s^m = \sum_r \mathcal{V}_{m,r} E_i^r \tag{A.20}$$

where the coefficients of the polynomial, $\mathcal{V}_{m,r}$, are functions of q^2, q_0, and E_χ. The response function is then

$$S(q_0, q) = \alpha t^n \frac{m_i^2}{\pi q}\int dE_i \; f_{\mathrm{FD}}(E_i)(1-f_{\mathrm{FD}}(E_i+q_0))\frac{\mathcal{U}_m}{q^{2m}}\Theta(E_i)\Theta(1-\cos^2\theta). \tag{A.21}$$

Therefore, the integrals we are interested in computing are over the FD distributions, which we call

$$\mathcal{F}_r(E_i, q_0) = \int dE_i E_i^r f_{\mathrm{FD}}(E_i)(1 - f_{\mathrm{FD}}(E_i + q_0)). \tag{A.22}$$

To proceed, make the change to the dimensionless variables

$$x = \frac{E_i - \varepsilon_{F,i}}{T_\star}, \; z = \frac{q_0}{T_\star}, \tag{A.23}$$

which we can use to write

$$\begin{aligned}
\mathcal{F}_r(E_i, q_0) &= T_\star \int dx \, (\varepsilon_{F,i} + T_\star x)^r \, f_{\mathrm{FD}}(x) f_{\mathrm{FD}}(-x - z) && \text{(A.24)}\\
&= T_\star \int dx \sum_{j=0}^{r} \binom{r}{j} T_\star^j x^j \varepsilon_{F,i}^{r-j} f_{\mathrm{FD}}(x) f_{\mathrm{FD}}(-x - z) && \text{(A.25)}\\
&= \sum_{j=0}^{r} T_\star^{j+1} \binom{r}{j} \varepsilon_{F,i}^{r-j} \int dx x^j f_{\mathrm{FD}}(x) f_{\mathrm{FD}}(-x - z) && \text{(A.26)}\\
&= \sum_{j=0}^{r} \binom{r}{j} \varepsilon_{F,i}^{r-j} \int dE_i (E_i - \varepsilon_{F,i})^j f_{\mathrm{FD}}(E_i) f_{\mathrm{FD}}(-E_i - q_0) && \text{(A.27)}\\
&= \sum_{j=0}^{r} \binom{r}{j} \varepsilon_{F,i}^{r-j} (-1)^j \frac{q_0^{j+1}}{j+1} g_j \left(\frac{E_i - \varepsilon_{F,i}}{q_0}\right), \quad \text{for } T_\star \to 0, && \text{(A.28)}
\end{aligned}$$

where the final line holds in the zero-temperature approximation in which the FD distributions become Θ-functions, allowing the integrals to be expressed in terms of the function

$$g_j(x) = \begin{cases} 1, & x > 0 \\ 1-(-x)^{j+1}, & -1 < x < 0\,. \\ 0, & x < -1 \end{cases} \tag{A.29}$$

The integration range for E_i is obtained from the two Θ-functions. There are two cases to be considered, $t < 0$ and $t > 0$. In the former case, the range become $E_i^{t^-} < E_i < \infty$ and for the latter $0 < E_i < E_i^{t^+}$. These integration bounds are obtained from Eq. A.15, by settting $\cos\theta = 1$, and are given by

$$E_i^{t^-} = -\left(m_i + \frac{q_0}{2}\right) + \sqrt{\left(m_i + \frac{q_0}{2}\right)^2 + \left(\frac{\sqrt{q^2-q_0^2}}{2} - \frac{m_i q_0}{\sqrt{q^2-q_0^2}}\right)^2} \tag{A.30}$$

$$E_i^{t^+} = -\left(m_i + \frac{q_0}{2}\right) + \sqrt{\left(m_i + \frac{q_0}{2}\right)^2 - \left(\frac{\sqrt{q_0^2-q^2}}{2} + \frac{m_i q_0}{\sqrt{q_0^2-q^2}}\right)^2}\,. \tag{A.31}$$

These are both the same root of Eq. A.15, but with an interchange of $t \leftrightarrow -t$. We denote the response function for $t < 0$ as S^- and for $t > 0$ as S^+. For S^- we have

$$S_m^- = \alpha t^n \frac{m_i^2}{\pi q^{2m+1}} \sum_{r=0}^{m} \mathcal{V}_{m,r} \int_{E_i^{t^-}}^{\infty} dE_i E_i^r f_{\rm FD}(E_i)(1 - f_{\rm FD}(E_i + q_0)) \tag{A.32}$$

$$= \alpha t^n \frac{m_i^2}{\pi q^{2m+1}} \sum_{r=0}^{m} \mathcal{V}_{m,r} \sum_{j=0}^{r} \binom{r}{j} \varepsilon_{F,i}^{r-j} \int_{E_i^{t^-}}^{\infty} dE_i (E_i - \varepsilon_{F,i})^j f_{\rm FD}(E_i) f_{\rm FD}(-E_i - q_0) \tag{A.33}$$

$$= \alpha t^n \frac{m_i^2}{\pi q^{2m+1}} \sum_{r=0}^{m} \mathcal{V}_{m,r} \sum_{j=0}^{r} \binom{r}{j} \varepsilon_{F,i}^{r-j} \frac{(-1)^j q_0^{j+1}}{j+1} \left[1 - g_j\left(\frac{E_i^{t^-} - \varepsilon_{F,i}}{q_0}\right)\right] \tag{A.34}$$

$$= \alpha t^n \frac{m_i^2}{\pi q^{2m+1}} \sum_{r=0}^{m} \mathcal{V}_{m,r} \sum_{j=0}^{r} \binom{r}{j} \varepsilon_{F,i}^{r-j} \frac{(-1)^j q_0^{j+1}}{j+1} h_j\left(\frac{E_i^{t^-} - \varepsilon_{F,i}}{q_0}\right), \tag{A.35}$$

while for S^+ the logic is

$$S^+_m = \alpha t^n \frac{m_i^2}{\pi q^{2m+1}} \sum_{r=0}^{m} \mathcal{V}_{m,r} \int_0^{E_i^{t^+}} dE_i E_i^r f_{\rm FD}(E_i)(1 - f_{\rm FD}(E_i + q_0)) \tag{A.36}$$

$$= \alpha t^n \frac{m_i^2}{\pi q^{2m+1}} \sum_{r=0}^{m} \mathcal{V}_{m,r} \sum_{j=0}^{r} \binom{r}{j} \varepsilon_{F,i}^{r-j} \int_0^{E_i^{t^+}} dE_i (E_i - \varepsilon_{F,i})^j f_{\rm FD}(E_i) f_{\rm FD}(-E_i - q_0) \tag{A.37}$$

$$= \alpha t^n \frac{m_i^2}{\pi q^{2m+1}} \sum_{r=0}^{m} \mathcal{V}_{m,r} \sum_{j=0}^{r} \binom{r}{j} \varepsilon_{F,i}^{r-j} \frac{(-1)^j q_0^{j+1}}{j+1} \left[g_j \left(\frac{E_i^{t^+} - \varepsilon_{F,i}}{q_0} \right) - g_j \left(\frac{-\varepsilon_{F,i}}{q_0} \right) \right] \tag{A.38}$$

$$= -\alpha t^n \frac{m_i^2}{\pi q^{2m+1}} \sum_{r=0}^{m} \mathcal{V}_{m,r} \sum_{j=0}^{r} \binom{r}{j} \varepsilon_{F,i}^{r-j} \frac{(-1)^j q_0^{j+1}}{j+1} h_j \left(\frac{E_i^{t^+} - \varepsilon_{F,i}}{q_0} \right) \quad \text{for } q_0 < 0, \tag{A.39}$$

with

$$h_j(x) = \begin{cases} 0, \quad x > 0 \\ (-x)^{j+1}, \quad -1 < x < 0 \, . \\ 1, \quad x < -1 \end{cases} \tag{A.40}$$

The final step of the S^+ calculation holds only for up-scattering of the DM, i.e. $q_0 < 0$.

For matrix elements that are polynomials in s and t, the full response function is simply the sum of the n and m, giving

$$S^- = \sum_{n,m} \alpha_{n,m} t^n \frac{m_i^2}{\pi q^{2m+1}} \sum_{r=0}^{m} \mathcal{V}_{m,r} \sum_{j=0}^{r} \binom{r}{j} \varepsilon_{F,i}^{r-j} \frac{(-1)^j q_0^{j+1}}{j+1} h_j \left(\frac{E_i^{t^-} - \varepsilon_{F,i}}{q_0} \right) \tag{A.41}$$

$$S^+ = -\sum_{n,m} \alpha_{n,m} t^n \frac{m_i^2}{\pi q^{2m+1}} \sum_{r=0}^{m} \mathcal{V}_{m,r} \sum_{j=0}^{r} \binom{r}{j} \varepsilon_{F,i}^{r-j} \frac{(-1)^j q_0^{j+1}}{j+1} h_j \left(\frac{E_i^{t^+} - \varepsilon_{F,i}}{q_0} \right) \tag{A.42}$$

A.2 Elsatic Scattering

A.2.1 Down-scattering Rate

Returning to the scattering rate, we first look at the case of down-scattering, where the DM loses energy, $q_0 > 0$. In this case, the interaction rate is given by

$$\Gamma^-(E_\chi) = \int \frac{d\cos\theta_\chi k'^2 dk'}{64\pi^3 E_\chi E'_\chi} \Theta(E_\chi - q_0 - m_\chi)\Theta(q_0) \sum_{n,m} \frac{\alpha_{n,m} t^n}{q^{2m+1}} \times \sum_{r=0}^{m} \mathcal{V}_{m,r} \sum_{j=0}^{r} \binom{r}{j} \varepsilon_{F,i}^{r-j} \frac{(-1)^j q_0^{j+1}}{j+1} h_j \left(\frac{E_i^{t^-} - \varepsilon_{F,i}}{q_0} \right) \tag{A.43}$$

Change variables to q_0 and q through

$$q_0 = E_\chi - \sqrt{k'^2 + m_\chi^2}, \tag{A.44}$$

$$q^2 = k^2 + k'^2 - 2kk' \cos\theta_\chi, \tag{A.45}$$

$$\implies dk' d\cos\theta_\chi = \frac{E'_\chi q}{kk'^2} dq_0 dq \tag{A.46}$$

To further simplify the notation we introduce $t_E = -t = q^2 - q_0^2$, $dq = dt_E/(2q)$, and exchange the q-integral for

$$\implies dk' d\cos\theta_\chi = \frac{E'_\chi}{2kk'^2} dq_0 dt_E, \tag{A.47}$$

giving the interaction rate as

$$\Gamma^-(E_\chi)- = \frac{1}{128\pi^3 E_\chi k} \int_0^{E_\chi - m_\chi} dq_0 \int dt_E \sum_{n,m} \frac{\alpha_{n,m}(-1)^n t_E^n}{(t_E + q_0^2)^{m+\frac{1}{2}}} \times \sum_{r=0}^{m} \mathcal{V}_{m,r} \sum_{j=0}^{r} \binom{r}{j} \varepsilon_{F,i}^{r-j} \frac{(-1)^j q_0^{j+1}}{j+1} h_j \left(\frac{E_i^{t^-} - \varepsilon_{F,i}}{q_0} \right) \tag{A.48}$$

$$= \sum_{n,m} \frac{(-1)^n \alpha_{n,m}}{128\pi^3 E_\chi k} \int_0^{E_\chi - m_\chi} dq_0 \int \frac{dt_E t_E^n}{(t_E + q_0^2)^{m+\frac{1}{2}}} \times \sum_{r=0}^{m} \mathcal{V}_{m,r} \sum_{j=0}^{r} \binom{r}{j} \varepsilon_{F,i}^{r-j} \frac{(-1)^j q_0^{j+1}}{j+1} h_j \left(\frac{E_i^{t^-} - \varepsilon_{F,i}}{q_0} \right). \tag{A.49}$$

There are then two main cases to consider; when $h_j(x)$ is unity or when it is not. We denote the t_E integrand in the former case as f_1 and f_2 for the latter, given explicitly as

$$f_1^{(m,n)}(t_E) = \frac{t_E^n}{(t_E+q_0^2)^{m+\frac{1}{2}}} \sum_{r=0}^{m} \mathcal{V}_{m,r} \sum_{j=0}^{r} \binom{r}{j} \varepsilon_{F,i}^{r-j} \frac{(-1)^j q_0^{j+1}}{j+1}, \tag{A.50}$$

$$f_2^{(m,n)}(t_E) = \frac{-t_E^n}{(t_E+q_0^2)^{m+\frac{1}{2}}} \sum_{r=0}^{m} \mathcal{V}_{m,r} \sum_{j=0}^{r} \binom{r}{j} \varepsilon_{F,i}^{r-j} \frac{1}{j+1} \left(E_i^{t^-} - \varepsilon_{F,i}\right)^{j+1}, \tag{A.51}$$

where we suppress the explicit dependence on the other variables for brevity. We encode the integrals over t_E within an operator

$$\begin{aligned}\mathcal{I}_{n,m}(f^{(m,n)}(t), t_1^+, t_2^+, t_1^-, t_2^-) = &\sum_{i=1,2}\sum_{j=1,2} \left(F^{(m,n)}(t_i^+) - F^{(m,n)}(t_j^-)\right) \\ &\times \Theta\left(t_{3-i}^+ - t_i^+\right)\Theta\left(t_i^+ - t_j^-\right)\Theta\left(t_j^- - t_{3-j}^-\right),\end{aligned} \tag{A.52}$$

$$F^{(m,n)}(t) = \int dt\, f^{(m,n)}(t). \tag{A.53}$$

The full interaction rate is then written as

$$\begin{aligned}\Gamma^-(E_\chi) = &\sum_{n,m} \frac{(-1)^n \alpha_{n,m}}{128\pi^3 E_\chi k} \int_0^{E_\chi - m_\chi} dq_0 \\ &\times \Big[\mathcal{I}_{n,m}\left(f_1^{(m,n)}(t), t_E^+, t_{\mu^-}^+, t_E^-, t_{\mu^-}^-\right)\Theta(\varepsilon_{F,i} - q_0) \\ &+ \mathcal{I}_{n,m}\left(f_2^{(m,n)}(t), t_E^+, t_{\mu^+}^+, t_E^-, t_{\mu^-}^+\right)\Theta(\varepsilon_{F,i} - q_0) \\ &+ \mathcal{I}_{n,m}\left(f_2^{(m,n)}(t), t_E^+, t_{\mu^-}^-, t_E^-, t_{\mu^+}^-\right)\Theta(\varepsilon_{F,i} - q_0) \\ &+ \mathcal{I}_{n,m}\left(f_2^{(m,n)}(t), t_E^+, t_{\mu^+}^+, t_E^-, t_{\mu^+}^-\right)\Theta(q_0 - \varepsilon_{F,i})\Big],\end{aligned} \tag{A.54}$$

where the t_E integration limits are

$$t_E^\pm = 2\left[E_\chi(E_\chi - q_0) - m_\chi^2 \pm k\sqrt{(E_\chi - q_0)^2 - m_\chi^2}\right], \tag{A.55}$$

$$\begin{aligned}t_{\mu^+}^\pm = 2\Big[&\varepsilon_{F,i}(\varepsilon_{F,i} + q_0) + m_i(2\varepsilon_{F,i} + q_0) \\ &\pm\sqrt{\left(\varepsilon_{F,i}(\varepsilon_{F,i} + q_0) + m_i(2\varepsilon_{F,i} + q_0)\right)^2 - m_i^2 q_0^2}\Big],\end{aligned} \tag{A.56}$$

$$\begin{aligned}t_{\mu^-}^\pm = 2\Big[&\varepsilon_{F,i}(\varepsilon_{F,i} - q_0) + m_i(2\varepsilon_{F,i} - q_0) \\ &\pm\sqrt{\left(\varepsilon_{F,i}(\varepsilon_{F,i} - q_0) + m_i(2\varepsilon_{F,i} - q_0)\right)^2 - m_i^2 q_0^2}\Big],\end{aligned} \tag{A.57}$$

All interaction rate spectra will have an endpoint at $q_0 = q_0^{\rm MAX}$, the maximum amount of energy that can be lost in a single interaction. The value of $q_0^{\rm MAX}$ is shown in the left panel of Fig. 2.2 as a function of B in the case of large DM mass ($m_\chi = 1\,\mathrm{TeV}$), for several values of $\varepsilon_{F,n}$. The endpoint can be found as the minimum between the DM kinetic energy and the root of one of the following two equations

$$t_E^- = t_{\mu^+}^+, \tag{A.58}$$
$$t_E^+ = t_{\mu^+}^-. \tag{A.59}$$

Only one of these equations will have a positive root for a given choice of m_χ, $\varepsilon_{F,n}$ and E_χ. For $m_\chi \gg m_i$, the second equation never has a solution, and the solution of the first equation is always much lower than the kinetic energy. This results in the value of $q_0^{\rm MAX}$ becoming independent of m_χ in this mass range.

The shape of the differential interaction rate depends very weakly on m_χ and B for $m_\chi \gg m_i$ and $m_\chi \ll m_i$, as seen by plotting it as a function of $q_0^{\rm norm} = q_0/q_0^{\rm MAX}$. Therefore, we use as a reference $m_\chi = 1\,\mathrm{TeV}$ (left) and $m_\chi = 10\,\mathrm{MeV}$ (right), $B = 0.5$, and show the normalised differential interaction rates in Fig. A.2 for $n = 0, 1, 2$, and neutron targets. We observe in the left panels that for $n = 0$ interaction rates are flat (or peaked, depending on $\varepsilon_{F,n}$) at low energy and suppressed at high energies, while for $n = 1, 2$ the profiles become peaked at higher and higher energies. Conversely, for $m_\chi = 10\,\mathrm{MeV}$ the peak of the spectrum is shifted to lower energies with increasing power of t ($d\sigma \propto t^n$).

A.2.2 Up-scattering Rate

We now treat the case of $q_0 < 0$, applicable to up scattering and evaporation. Focusing on s-independent matrix elements for the moment, the response function is

$$S_{\rm up}^-(q_0, q) = \frac{m_i^2}{\pi q} \int_{E_i^{t-}}^{\infty} f_{\rm FD}(E_i)(1 - f_{\rm FD}(E_i - |q_0|)) \tag{A.60}$$

and evaluate the integral, now with $q_0 < 0$. If we attempt to take the $T_\star \to 0$ limit as before, we find that there is no overlap of the FD distributions and the result vanishes. Instead, we keep the leading order thermal corrections, i.e. terms of order $e^{-|q_0|/T_\star}$. The result is

$$\mathcal{F}_0(E_i, -|q_0|) = \frac{T_\star e^{-|q_0|/T_\star}}{1 - e^{-|q_0|/T_\star}} \left[\log\left(1 + e^{(E_i - \varepsilon_{F,i})/T_\star}\right) - \log\left(1 + e^{(E_i - |q_0| - \varepsilon_{F,i})/T_\star}\right)\right], \tag{A.61}$$

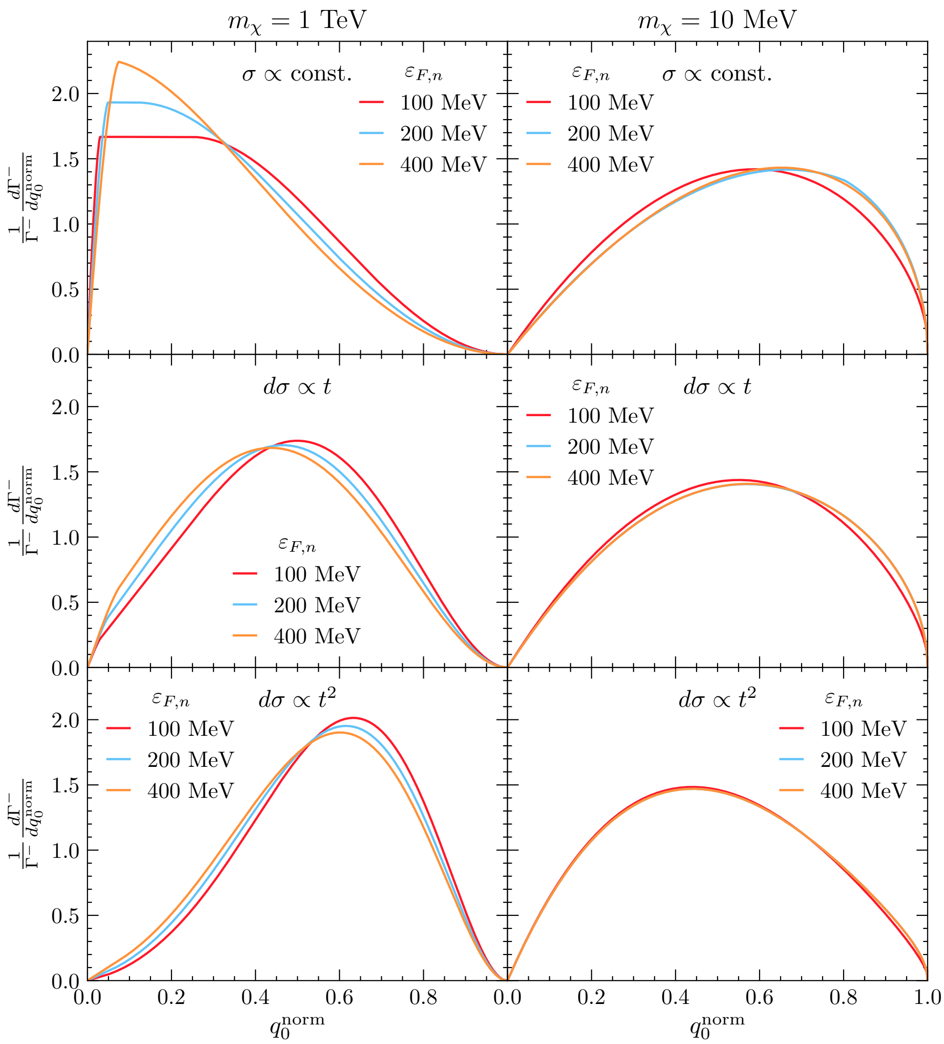

Figure A.2: Normalised differential interaction rates, $\frac{1}{\Gamma}\frac{d\Gamma^-}{dq_0^{\rm norm}}$, as a function of $q_0^{\rm norm}$ for different values of $\varepsilon_{F,n}$, with $m_\chi = 1\,\text{TeV}$ (left panels) $m_\chi = 10\,\text{MeV}$ (right panels) and $B = 0.5$. Top row: $n = 0$, middle row: $n = 1$, bottom row: $n = 2$.

where after taking $T_\star \to 0$ we recognise three regions of interest

$$\lim_{T_\star \to 0} T_\star \mathcal{F}_0(E_i, -|q_0|) = \begin{cases} \dfrac{|q_0| e^{-|q_0|/T_\star}}{1 - e^{-|q_0|/T_\star}}, & E_i > \varepsilon_{F,i} + |q_0| \\ \dfrac{(E_i - \varepsilon_{F,i}) e^{-|q_0|/T_\star}}{1 - e^{-|q_0|/T_\star}}, & \varepsilon_{F,i} + |q_0| > E_i > \varepsilon_{F,i} \\ 0, & \varepsilon_{F,i} > E_i \end{cases}, \tag{A.62}$$

and we can write this as

$$\lim_{T_\star \to 0} T_\star \mathcal{F}_0(E_i, -|q_0|) = \frac{|q_0| e^{-|q_0|/T_\star}}{1 - e^{-|q_0|/T_\star}} h_0 \left(\frac{\varepsilon_{F,i} - E_i}{q_0} \right). \tag{A.63}$$

The response function for upscattering is then

$$S^-_{\rm up}(q_0, q) = \frac{m_i^2 q_0}{\pi q} \frac{e^{-|q_0|/T_\star}}{e^{-|q_0|/T_\star} - 1} \left[1 - h_0 \left(\frac{E_i^{t-} - \varepsilon_{F,i}}{q_0} \right) \right] \tag{A.64}$$

$$= \frac{m_i^2 q_0}{\pi q} \frac{e^{-|q_0|/T_\star}}{e^{-|q_0|/T_\star} - 1} g_0 \left(\frac{\varepsilon_{F,i} - E_i^{t-}}{q_0} \right), \tag{A.65}$$

leading to the corresponding up-scattering rate being

$$\Gamma^-_{\rm up}(E_\chi) = \int \frac{k'^2 d\cos\theta dk'}{64\pi^2 m_i^2 E_\chi E'_\chi} |\overline{\mathcal{M}}|^2 \Theta(E_\chi + |q_0| - m_\chi) \Theta(q_0) S^-_{\rm up}(q_0, q) \tag{A.66}$$

$$= \frac{(-1)^n \alpha}{128\pi^3 E_\chi k} \int_{-\infty}^0 dq_0 \, \frac{q_0 e^{q_0/T_\star}}{e^{q_0/T_\star} - 1} \int dt_E \, \frac{t_E^n}{\sqrt{t_E - |q_0|^2}} g_0 \left(\frac{\varepsilon_{F,i} - E_i^{t-}}{q_0} \right) \tag{A.67}$$

where we have substituted $|\overline{\mathcal{M}}|^2 = \alpha t^n$ as the matrix element. Typically, we expect to be in the regime where $g_0 = 1$, and so the differential up-scattering rate is related result for down-scattering through

$$\frac{d\Gamma^-_{\rm up}}{dq_0} = \frac{e^{-|q_0|/T_\star}}{e^{-|q_0|/T_\star} - 1} \frac{d\Gamma^-_{\rm down}}{dq_0} \tag{A.68}$$

This result applies generally to all matrix elements, not just the ones $\propto t^n$. The result can be derived from the principle of detailed balance, and hence is true for all interactions we consider. To calculate the total interaction rate, the t_E integrations can be performed in the same manner as in the previous section, with the q_0 integration bounds being $(-\infty, 0)$.

A.3 Non-degenerate weak field limit

When setting up the centre of mass energy interval in section 2.3, we have set the DM energy to 0 at infinity. This means that when taking the classical non-relativistic limit, the interaction rate would approach

$$\Omega^-(r) \to n_i(r) v_{\rm esc}(r)\sigma, \tag{A.69}$$

in the simple case of a constant cross-section. Taking Eq. 2.39, one can first strip out the Pauli blocking term $(1 - f_{\rm FD})$, and then the integration in t and s can be performed analytically. Taking the limit $u_i \to 0$, $E_i = m_i/\sqrt{1-u_i^2}$, and then the weak field approximation $B(r) \to 1 - v_{\rm esc}^2(r)$, for a constant cross-section $\frac{d\sigma}{d\cos\theta_{\rm cm}} = \frac{\sigma}{2}$, we find

$$\begin{aligned}
\Omega^-(r) &\to m_i^2 \frac{\sigma}{2} \frac{2u_i v_{\rm esc}(r) f_{\rm FD}(E_i, r)}{\pi^2} dE_i & \text{(A.70)}\\
&= m_i^3 \frac{\sigma}{2} \frac{2u_i v_{\rm esc}(r) f_{\rm FD}(E_i, r)}{\pi^2} u_i du_i & \text{(A.71)}\\
&= m_i^3 \frac{\sigma}{2} \frac{v_{\rm esc}(r) f_{\rm FD}(E_i, r)}{2\pi^3} d^3u_i & \text{(A.72)}\\
&= \frac{\sigma}{2} \frac{v_{\rm esc}(r) f_{\rm FD}(E_i, r)}{2\pi^3} d^3p. & \text{(A.73)}
\end{aligned}$$

Cases with $\sigma \propto t^n$ give similar results. Recall that

$$\frac{2 f_{\rm FD}(E_i)}{(2\pi)^3} d^3p, \tag{A.74}$$

is the number density of neutron states. Then, following expression in 2.31 we substitute it with the classical number density $n_i(r)$, to obtain the expected classical limit given by Eq. A.69.

A.4 Intermediate DM mass range

The interaction rate in Eq. 2.39 can be rewritten in terms of the DM momentum p_χ, such that

$$\begin{aligned}
\Omega^-(r) = \frac{\zeta(r)}{32\pi^3} \int dt dE_i ds |\overline{M}|^2 \frac{E_i}{2s\beta(s) - \gamma^2(s)} \frac{1}{p_\chi} \frac{s}{\gamma(s)} \\
\times f_{\rm FD}(E_i, r)(1 - f_{\rm FD}(E_i^{'}, r)),
\end{aligned} \tag{A.75}$$

where we have also used Eq. 2.51. We first consider the case where the squared matrix element depends only on t, i.e. $|\overline{M}|^2 \propto t^n$, we can straightforwardly perform the integral over t,

$$\Omega^-(r) = \frac{\zeta(r)}{32\pi^3}\int dE_i ds \bar{g}(s) \frac{E_i\gamma(s)}{2s\beta(s)-\gamma^2(s)} \frac{1}{n+1}\frac{1}{p_\chi}\left(\frac{\gamma^2(s)}{s}\right)^n \times f_{\rm FD}(E_i,r)(1-f_{\rm FD}(E_i^{'},r)). \tag{A.76}$$

We now assume that either $\mu \gg 1$ or $\mu \ll 1$. In both cases, the integration range for s shrinks to $[s_0-\delta s, s_0+\delta s]$, with $\delta s \ll s_0$, and the following simplifications can be made;

$$s_0 = m_i^2 + m_\chi^2 + 2\frac{E_i m_\chi}{\sqrt{B(r)}} = m_i^2+m_\chi^2+2E_iE_\chi, \tag{A.77}$$

$$\delta s = 2\sqrt{\frac{1-B(r)}{B(r)}} m_\chi \sqrt{E_i^2-m_i^2} = 2p_\chi\sqrt{E_i^2-m_i^2}, \tag{A.78}$$

$$\frac{\gamma(s)}{2s\beta(s)-\gamma^2(s)} \to \frac{\sqrt{1-B(r)}}{2\left(m_i^2+m_\chi^2\right)} = \frac{p_\chi}{2E_\chi\left(m_i^2+m_\chi^2\right)}, \tag{A.79}$$

$$\frac{\gamma^2(s)}{s} \to \frac{4(1-B(r))m_\chi^2}{B(r)\left(1+\mu^2\right)} = \frac{4p_\chi^2}{1+\mu^2}. \tag{A.80}$$

If $g(s)$ is regular in s_0, we can estimate the integral in s to be $2\delta s$, approximating the integrand as being constant in that range, which gives

$$\Omega^-(r) \sim \zeta(r)\frac{1}{16\pi^3}\frac{\sqrt{E_\chi^2-m_\chi^2}}{E_\chi\left(m_i^2+m_\chi^2\right)}\frac{\left[\frac{4\left(E_\chi^2-m_\chi^2\right)}{1+\mu^2}\right]^n}{n+1}\int dE_iE_i\sqrt{E_i^2-m_i^2} \times f_{\rm FD}(E_i,r)(1-f_{\rm FD}(E_i^{'},r)). \tag{A.81}$$

To perform the integral in E_i, we have to potentially deal with Pauli blocking. However, for $\mu \gg 1$, Pauli blocking is not effective and we can drop the $1-f_{\rm FD}$ term to obtain

$$\int_{m_i}^{m_i+\varepsilon_{F,i}(r)} dE_iE_i\sqrt{E_i^2-m_i^2} f_{\rm FD}(E_i,r) = \frac{\left[\varepsilon_{F,i}(r)(2m_i+\varepsilon_{F,i}(r))\right]^{3/2}}{3} \tag{A.82}$$

$$= \pi^2 n_{\rm free}(r). \tag{A.83}$$

This, together with $\zeta(r)$, result in an overall factor of $\pi^2 n_i(r)$, leaving

$$\Omega^-(r) \sim \frac{n_i(r)}{16\pi}\frac{\sqrt{E_\chi^2-m_\chi^2}}{m_\chi^2E_\chi}\frac{1}{n+1}\left[\frac{4(1-B(r))m_\chi^2}{B(r)(1+\mu^2)}\right]^n, \tag{A.84}$$

and the capture rate reads,

$$C \sim \frac{1}{4v_\star}\frac{\rho_\chi}{m_\chi^3}\mathrm{Erf}\left(\sqrt{\frac{3}{2}}\frac{v_\star}{v_d}\right)\int_0^{R_\star} r^2 dr\, n_i(r)\frac{1-B(r)}{B(r)}\frac{1}{n+1} \times\left[\frac{4(1-B(r))m_\chi^2}{B(r)(1+\mu^2)}\right]^n . \tag{A.85}$$

We can now rewrite these expressions in terms of the cross-section which has been averaged over s,

$$\begin{aligned}
\langle\sigma(r)\rangle &= \left\langle \int dt \frac{d\sigma}{dt}\right\rangle_s && \text{(A.86)}\\
&= \frac{1}{2\delta s}\int_{s_0-\delta s}^{s_0+\delta s} ds\int dt\frac{d\sigma}{dt} && \text{(A.87)}\\
&= \frac{1}{64\pi m_\chi^2 m_i^2}\frac{B(r)}{(1-B(r))}\int dt\, t^n && \text{(A.88)}\\
&= \frac{1}{64\pi m_\chi^2 m_i^2}\frac{B(r)}{(1-B(r))}\frac{1}{(n+1)}\left[\frac{4(1-B(r))m_\chi^2}{B(r)(1+\mu^2)}\right]^{n+1} && \text{(A.89)}\\
&= \frac{1}{16\pi\left(m_i^2+m_\chi^2\right)}\frac{1}{(n+1)}\left[\frac{4(1-B(r))m_\chi^2}{B(r)(1+\mu^2)}\right]^{n}, && \text{(A.90)}
\end{aligned}$$

which leads to,

$$\Omega^-(r) \sim n_i(r)\langle\sigma(r)\rangle\frac{\sqrt{E_\chi^2-m_\chi^2}}{E_\chi}, \tag{A.91}$$

$$C \sim \frac{4\pi}{v_\star}\frac{\rho_\chi}{m_\chi}\mathrm{Erf}\left(\sqrt{\frac{3}{2}}\frac{v_\star}{v_d}\right)\int_0^{R_\star} r^2 dr\, n_i(r)\frac{1-B(r)}{B(r)}\langle\sigma(r)\rangle. \tag{A.92}$$

From Eq. A.92, we can identify the typical $1/m_\chi$ scaling of the capture rate. This equation also looks very similar to the non-relativistic case, with $1-B(r)$ playing the role of the escape velocity, $v_{\rm esc}^2(r)$, and $1/B(r)$ being a relativistic correction.

Turning to the case of s-dependent matrix elements, $|\overline{\mathcal{M}}|^2 = g(\bar{s})t^n$ for $\bar{g}$ some function of s, the result is fairly similar. The main difference is that we must keep all terms in m_i and m_χ, leading to the new substitutions

$$\frac{\gamma(s)}{s^2-[m_i^2-m_\chi^2]^2} \sim \frac{\sqrt{1-B(r)}}{2\left(m_i^2+m_\chi^2+2m_i m_\chi/\sqrt{B(r)}\right)}, \tag{A.93}$$

$$\frac{\gamma^2(s)}{s} \to \frac{4(1-B(r))m_\chi^2}{B(r)\left(1+\mu^2\right)+2\sqrt{B(r)}\mu}. \tag{A.94}$$

Now when we take the limit as $\varepsilon_{F,n} \to 0$, the integrand over s can be approximated as a δ-function, resulting in s being fixed to the value of s_0. As such, we no longer need to average the cross-section over s. The results are

$$\begin{aligned}\Omega^-(r) \sim \frac{n_i(r)}{16\pi} &\frac{\sqrt{E_\chi^2 - m_\chi^2}}{E_\chi\left(m_i^2 + m_\chi^2 + 2m_i E_\chi\right)} \frac{\bar{g}(s_0)}{n+1} \\ &\left[\frac{4(1-B(r))m_\chi^2}{B(r)\left(1+\mu^2\right) + 2\sqrt{B(r)}\mu}\right]^n .\end{aligned} \tag{A.95}$$

$$C \sim C_{\text{approx},s} = \frac{4\pi}{v_\star}\frac{\rho_\chi}{m_\chi}\text{Erf}\left(\sqrt{\frac{3}{2}}\frac{v_\star}{v_d}\right)\int_0^{R_\star} r^2 dr\, n_i(r)\frac{1-B(r)}{B(r)}\sigma(r), \tag{A.96}$$

$$\begin{aligned}\sigma(r) = \int dt \frac{d\sigma}{dt} = &\frac{1}{16\pi\left(m_i^2 m_\chi^2 + 2m_i m_\chi/\sqrt{B(r)}\right)}\frac{\bar{g}(s_0)}{(n+1)} \\ &\times\left[\frac{4(1-B(r))m_\chi^2}{B(r)(1+\mu^2) + 2\sqrt{B(r)}\mu}\right]^n .\end{aligned} \tag{A.97}$$

A.5 Kinematic phase space for DM-electron scattering

When deriving the interaction rate in the context of DM capture in NSs, we assumed that all the target phase space was available to scatter with DM. This is not necessarily true if the target is highly degenerate or if gravity is not particularly strong, like in NSs. In fact, for the scattering to occur, both the DM and target momenta should be in the inbound direction in the centre of mass frame. This is true in the whole phase space only when the following condition is satisfied

$$\frac{1}{\sqrt{B(r)}} > \frac{\varepsilon_{F,e}}{m_e}. \tag{A.98}$$

To clarify this point, we first derive this constraint using non-relativistic kinematics. The DM particle of mass m_χ has an initial speed

$$v_{\text{esc}} = \sqrt{1-B}, \tag{A.99}$$

while the target has a mass m_e and an energy

$$E_e = m_e + b\varepsilon_{F,e} = m_e\left(1 + b\frac{\varepsilon_{F,e}}{m_e}\right), \quad b \in [0,1]. \tag{A.100}$$

Using non-relativistic kinematics, the speed of the target is

$$v_e = \sqrt{2b\frac{\varepsilon_{F,e}}{m_e}}. \tag{A.101}$$

The centre of mass velocity is defined as

$$\vec{v}_{com} = \frac{1}{m_\chi + m_e}(m_\chi \vec{v}_{esc} + m_e \vec{v}_e), \tag{A.102}$$

so the DM speed in the CoM frame is $\vec{v}'_\chi = \vec{v}_{\rm esc} - \vec{v}_{\rm com}$. To ensure that the DM and the target are not moving away from each other, the following condition should hold, $\vec{v}'_\chi \cdot \vec{v}_{\rm esc} > 0$, i.e., the component of the DM velocity in the CoM frame is always parallel to the initial speed in the star frame. This condition leads to

$$\cos\theta < \sqrt{\frac{1-B}{2b(\varepsilon_{F,e}/m_e)}}, \tag{A.103}$$

where θ is the angle between the DM and the target speed in the star frame. If $\varepsilon_{F,e}/m_e \gg 1-B$, the condition reduces to

$$\cos\theta < 0, \tag{A.104}$$

meaning that the collision is head-on only.

Repeating the same exercise with relativistic kinematics, the variable whose parameter space is modified by the above mentioned condition is the centre of mass energy s,

$$s = m_\chi^2 + m_e^2 + \frac{2m_e m_\chi}{\sqrt{B}}\left(1 + b\frac{\varepsilon_{F,e}}{m_e} - a\sqrt{1-B}\sqrt{2b\frac{\varepsilon_{F,e}}{m_e} + b^2\frac{\varepsilon_{F,e}^2}{m_e^2}}\right),\ a \in [-1,1], \tag{A.105}$$

and the new condition becomes

$$a = \frac{s_{\rm max} + s_{\rm min} - 2s}{s_{\rm max} - s_{\rm min}} < \left(1 + b\frac{\varepsilon_{F,e}}{m_e}\right)\sqrt{\frac{1-B}{2b\frac{\varepsilon_{F,e}}{m_e} + b^2\frac{\varepsilon_{F,e}^2}{m_e^2}}} = E_e\sqrt{\frac{1-B}{E_e^2 - m_e^2}}. \tag{A.106}$$

With the exception of the heaviest WDs, we have $\varepsilon_{F,e}/m_e \lesssim 1$. Then, with $1-B \sim 10^{-3}$, we can check that expanding Eq. A.106 leads to Eq. A.103 and that $a \lesssim 0$. This implies that approximately half of the phase space is not available for scattering. (For electrons in NSs we instead have $\varepsilon_{F,e}/m_e \gg 1$, and hence this does not occur.)

Taking the ultra-relativistic limit for electrons, Eq. A.106 reduces to

$$a < \sqrt{1-B}. \tag{A.107}$$

This restriction of the available phase space results in variations of the order of $\mathcal{O}(10\%)$ for both the interaction and capture rates.

A.6 Interaction Rate for Low Energies

Need to consider the case where $T_\chi = E_\chi - m_\chi < \mu_F$, with $0 < q_0 < T_\chi < \varepsilon_{F,i}$. Then the t_E integration limits follow the hierarchy; $t^+_{\mu^+} \sim t^+_{\mu^-} \geq t^-_{\mu^-} \sim t^-_{\mu^+} \gtrsim 0$, and $t^+_{\mu^-} \gg t^+_E \geq t^-_E \gg t^-_{\mu^-}$. Then the only term in A.54 that remains is the first term, and only the $i = j = 1$ term contributes, leaving

$$\Gamma^-(E_\chi) = \sum_{n,m} \frac{(-1)^n \alpha_{n,m}}{128\pi^3 E_\chi k} \int_0^{E_\chi - m_\chi} dq_0 \int_{t_E^-}^{t_E^+} dt_E \, f_1^{(m,n)}(t_E) \tag{A.108}$$

At first order in q_0 and K_χ, we have the following approximations

$$E_\chi \approx m_\chi \tag{A.109}$$

$$k \approx \sqrt{2 m_\chi T_\chi} \tag{A.110}$$

$$t_E^\pm \approx 4 m_\chi T_\chi \left[1 - \frac{q_0}{2K_\chi} \pm \sqrt{1 - \frac{q_0}{K_\chi}}\right] \tag{A.111}$$

$$\Gamma^- \approx \sum_{n,m} \frac{(-1)^n \alpha_{n,m}}{128\sqrt{2}\pi^3 m_\chi^{3/2} K_\chi^{1/2}} \int_0^{K_\chi} dq_0 \int_{t_E^-}^{t_E^+} dt_E \, f_1^{(m,n)}(t_E) \tag{A.112}$$

For single term matrix elements such that $|\overline{\mathcal{M}}|^2 = \alpha_{n,m}(-t)^n s^m$, the corresponding $\Gamma^-_{n,m}$ are

$$\Gamma^-_{0,0} = \frac{\alpha_{0,0}}{120\pi^3 m_\chi} K_\chi^2 \tag{A.113}$$

$$\Gamma^-_{1,0} = \frac{2\alpha_{1,0}}{105\pi^3} K_\chi^3 \tag{A.114}$$

$$\Gamma^-_{2,0} = \frac{4\alpha_{2,0} m_\chi}{63\pi^3} K_\chi^4 \tag{A.115}$$

$$\Gamma^-_{0,1} = \frac{\alpha_{0,1}((m_i + m_\chi)^2 + 2m_\chi \varepsilon_{F,i})}{120\pi^3} K_\chi^2 \tag{A.116}$$

$$\Gamma^-_{1,1} = \frac{2\alpha_{1,1}((m_i + m_\chi)^2 + 2m_\chi \varepsilon_{F,i})}{105\pi^3} K_\chi^3 \tag{A.117}$$

$$\Gamma^-_{0,2} = \frac{\alpha_{0,2}((m_i + m_\chi)^2 + 2m_\chi \varepsilon_{F,i})^2}{120\pi^3} K_\chi^2 \tag{A.118}$$

The $\alpha_{n,m}$ can be obtained at some reference point, taken to be the surface of the NS, from the differential cross-section,

$$\frac{d\sigma}{d\cos\theta_{\rm cm}} = \frac{\alpha_{n,m}(-t)^n s^m}{32\pi(m_i + m_\chi)^2} \tag{A.119}$$

which gives

$$\sigma_{0,0} = \frac{\alpha_{0,0}}{16\pi(m_i + m_\chi)^2} \tag{A.120}$$

$$\sigma_{1,0} = \frac{\alpha_{1,0}}{32\pi(m_i + m_\chi)^2} t_{\max} \tag{A.121}$$

$$\sigma_{2,0} = \frac{1}{3}\frac{\alpha_{2,0}}{16\pi(m_i + m_\chi)^2} t_{\max}^2 \tag{A.122}$$

$$\sigma_{0,1} = \frac{\alpha_{0,1}}{16\pi(m_i + m_\chi)^2} s \tag{A.123}$$

$$\sigma_{1,1} = \frac{\alpha_{1,1}}{32\pi(m_i + m_\chi)^2} t_{\max} s \tag{A.124}$$

$$\sigma_{0,2} = \frac{\alpha_{0,2}}{16\pi(m_i + m_\chi)^2} s^2 \tag{A.125}$$

where I have used

$$t = -\frac{t_{\max}}{2}(1 - \cos\theta_{\mathrm{cm}}) \tag{A.126}$$

$$t_{\max} \sim \frac{4m_i^2 m_\chi^2}{(m_i^2 + m_\chi^2)} \frac{1 - B(R_\star)}{B(R_\star)} \tag{A.127}$$

$$s \sim m_i^2 + m_\chi^2 + \frac{2m_\chi(m_i + \varepsilon_{F,i})}{\sqrt{B(R_\star)}} \tag{A.128}$$

$$\sim (m_i + m_\chi)^2 \tag{A.129}$$

Again introducing the correction

$$\zeta = \frac{n_i}{n_{free}} \sim \frac{3\pi^2}{(2m_i\varepsilon_{F,i})^{3/2}} n_i \tag{A.130}$$

Then the interaction rates can be expressed with respect to the surface of the star as

$$\Gamma^-_{0,0}(K_\chi) = \frac{\sqrt{2}}{10}\frac{(1+\mu)^2}{\mu}\frac{m_i}{(m_i\varepsilon_{F,i})^{3/2}}\sigma_{surf}n_iK_\chi^2 \tag{A.131}$$

$$\Gamma^-_{1,0}(K_\chi) = \frac{4\sqrt{2}}{35}\frac{(1+\mu)^2(1+\mu^2)}{\mu^2}\frac{1}{(m_i\varepsilon_{F,i})^{3/2}}\frac{B(R_\star)}{(1-B(R_\star))}\sigma_{surf}n_iK_\chi^3 \tag{A.132}$$

$$\Gamma^-_{2,0}(K_\chi) = \frac{\sqrt{2}}{7}\frac{(1+\mu)^2(1+\mu^2)^2}{\mu^3}\frac{1}{m_i(m_i\varepsilon_{F,i})^{3/2}}\left(\frac{B(R_\star)}{(1-B(R_\star))}\right)^2\sigma_{surf}n_iK_\chi^4 \tag{A.133}$$

$$\Gamma^-_{0,1}(K_\chi) = \frac{\sqrt{2}}{10}\frac{(m_i(1+\mu)^2+2\mu\varepsilon_{F,i})}{\mu(m_i\varepsilon_{F,i})^{3/2}}\sigma_{surf}n_iK_\chi^2 \tag{A.134}$$

$$\Gamma^-_{1,1}(K_\chi) = \frac{4\sqrt{2}}{35}\frac{(m_i(1+\mu)^2+2\mu\varepsilon_{F,i})(1+\mu^2)}{\mu^2 m_i(m_i\varepsilon_{F,i})^{3/2}}\frac{B(R_\star)}{(1-B(R_\star))}\sigma_{surf}n_iK_\chi^3 \tag{A.135}$$

$$\Gamma^-_{0,2}(K_\chi) = \frac{\sqrt{2}}{10}\frac{(m_i(\mu+1)^2+2\mu\varepsilon_{F,i})^2}{\mu(\mu+1)^2m_i(\varepsilon_{F,i}m_i)^{3/2}}\sigma_{surf}n_iK_\chi^2 \tag{A.136}$$

The average energy loss per collision is given by

$$\langle\Delta T\rangle = \frac{1}{\Gamma^-}\int_0^{K_\chi} dq_0\, q_0\frac{d\Gamma^-}{dq_0} \tag{A.137}$$

which gives the results

$$\langle\Delta T^{0,0}\rangle = \frac{4}{7}K_\chi \sim \langle\Delta T^{0,1}\rangle \sim \langle\Delta T^{0,2}\rangle \tag{A.138}$$

$$\langle\Delta T^{1,0}\rangle = \frac{5}{9}K_\chi \sim \langle\Delta T^{1,1}\rangle \tag{A.139}$$

$$\langle\Delta T^{2,0}\rangle = \frac{28}{55}K_\chi \tag{A.140}$$

The DM will reach thermal equilibrium with the targets when $K_\chi = T_\star$. There are two stages to this process; one where the interactions are not affected by Pauli blocking which takes N_1 collisions, and the next N_2 collisions where Pauli blocking is in effect. The time it takes for thermalisation to occur is given by the sum of the average times between collisions

$$t_{\text{therm}} = \sum_{n=0}^{N_2}\frac{1}{\Gamma^-(T_n)} \sim \sum_{n=N_1}^{N_2}\frac{1}{\Gamma^-(T_n)} \tag{A.141}$$

where T_n is the DM kinetic energy after n collisions. If Pauli blocking is in effect for the entire process, then T_n is related to the initial kinetic energy, T_0 through

$$T_n = T_0\left(1-\frac{\Delta T}{T}\right)^n. \tag{A.142}$$

This result implies the following relation;

$$\frac{T_N}{T_0} = \frac{T_{eq}}{T_0} = \left(1 - \frac{\Delta T}{T}\right)^N \tag{A.143}$$

Then for interaction rates which follow $\Gamma^- \propto (K_\chi)^p$, we have that

$$\begin{aligned}
t_{\text{therm}} &\propto \sum_{n=N_1}^{N_2} (T_n)^{-p} && \text{(A.144)}\\
&= \frac{1}{T_{N_1}^p} \sum_{n=N_1}^{N_2} \left(\left(1 - \frac{\Delta T}{T}\right)^{-p}\right)^n && \text{(A.145)}\\
&= \frac{1}{T_{N_1}^p} \frac{(1-\Delta T/T)^{p(1-N_1)} - (1-\Delta T/T)^{-pN_2}}{-1 + (1-\Delta T/T)^p} && \text{(A.146)}\\
&\sim \frac{1}{T_{N_1}^p} \frac{(1-\Delta T/T)^{-pN_2}}{1-(1-\Delta T/T)^p} \quad \text{for} \quad N_2 > N_1 && \text{(A.147)}\\
&= \frac{1}{T_{N_1}^p} \left(\frac{T_{eq}}{T_{N_1}}\right)^{-p} \frac{1}{1-(1-\Delta T/T)^p} && \text{(A.148)}\\
&= \frac{1}{T_{\text{eq}}^p} \frac{1}{1-(1-\Delta T/T)^p} && \text{(A.149)}
\end{aligned}$$